Rafael Alves
Figueiredo Ribeiro

# Grafeno em fibra ótica para deteção eletroquímica de nitritos – rumo à monitorização Lab-on-Fiber em aquacultura

# Graphene on fiber optics for electrochemical detection of nitrites – towards Lab-on-Fiber monitoring in aquaculture

Rafael Alves
Figueiredo Ribeiro

# Grafeno em fibra ótica para deteção eletroquímica de nitritos – rumo à monitorização Lab-on-Fiber em aquacultura

# Graphene on fiber optics for electrochemical detection of nitrites – towards Lab-on-Fiber monitoring in aquaculture

Dissertação apresentada à Universidade de Aveiro para cumprimento dos requisitos necessários à obtenção do grau de Mestre em Engenharia Física, realizada sob a orientação científica do Doutor Nuno Miguel Franco dos Santos, Investigador Pós-Doutoramento do Departamento de Física da Universidade de Aveiro e do Doutor Carlos Alberto Ferreira Marques, Investigador Principal do Departamento de Física da Universidade de Aveiro.

Este trabalho foi desenvolvido no âmbito do projeto i3N, UIDB/50025/2020 & UIDP/50025/2020 & LA/P/0037/2020, e do projeto DigiAqua PTDC/EEI-EEE/0415/2021 financiados por fundos do FEDER através do programa COMPETE 2020 e da FCT - Fundação portuguesa para a Ciência e Tecnologia.

FCT Fundação para a Ciência e a Tecnologia
MINISTÉRIO DA CIÊNCIA, TECNOLOGIA E ENSINO SUPERIOR

i3N INSTITUTE FOR NANOSTRUCTURES, NANOMODELLING AND NANOFABRICATION
RESEARCH, INNOVATION AND ENGINEERING APPLICATIONS

DIGIAQUA
DIGITIZING AQUACULTURE

**o júri / the jury**

presidente / president

**Professora Doutora Maria Rute de Amorim e Sá Ferreira André**
Professora Associada com Agregação da Universidade de Aveiro

vogais / examiners committee

**Doutor Luís Carlos Costa Coelho**
Investigador Pós-Doutoramento do Inesc Tec - Instituto de Engenharia de Sistemas e Computadores, Tecnologia e Ciência

**Doutor Nuno Miguel Franco dos Santos**
Investigador Pós-Doutoramento da Universidade de Aveiro (orientador)

**Agradecimentos / Acknowledgements**

Em primeiro lugar, gostaria de agradecer ao meu orientador, o Doutor Nuno Santos, pela constante disponibilidade, dedicação e por todo o conhecimento transmitido ao longo deste percurso, sem o qual não seria possível a realização e a compreensão deste trabalho.

Quero também agradecer ao meu coorientador, o Doutor Carlos Marques, por todo o apoio e estar sempre disponível para ajudar, seja no trabalho ou simplesmente falar e prestar motivação quando esta parecia estar a desvanecer-se.

Agradeço à Laura, que me acompanhou, por todo o apoio, simpatia e companhia, que foi tão bem-vinda nos longos dias passados no laboratório. Um agradecimento também ao Guilherme pela ajuda em explicar o funcionamento do seu sensor e pelas discussões que tivemos sobre como implementar ambos os sensores fabricados na plataforma híbrida, e que enriqueceram este trabalho.

Aos meus amigos, o meu sincero obrigado a cada um de vós por se importarem comigo e por todo o companheirismo e momentos de descontração proporcionados que tornaram mais fácil esta caminhada.

Por fim, agradecer à minha família, o meu irmão e sua namorada, e os meus pais, pelo apoio incondicional que me dão todos os dias, e por nunca deixarem de acreditar em mim e quererem sempre a minha felicidade, estou para sempre grato.

**Palavras-chave**

Aquacultura, Nitritos, Sensor Eletroquímico, Grafeno Induzido por Laser, Fibra Ótica, *Lab-on-Fiber*, Transdução Híbrida

**Resumo**

A monitorização de múltiplos parâmetros de qualidade da água, tais como a concentração de nitritos ($NO_2^-$), é fundamental para proporcionar bem-estar e crescimento dos peixes. As fibras óticas mostram grande potencial em aquacultura, devido à possibilidade de multiplexação de sensores ao longo da fibra, permitindo medições multiparamétricas in-situ. Por outro lado, sensores eletroquímicos são igualmente interessantes neste contexto devido ao seu baixo custo e elevada sensibilidade para deteção de diversos parâmetros bioquímicos, tais como contaminantes orgânicos, inorgânicos e até agentes patogénicos. A combinação de deteção ótica e eletroquímica pode ser muito útil com vista ao desenvolvimento de conceitos de laboratórios em fibra (*lab-on-fiber*) miniaturizados para uma ampla monitorização da qualidade da água. Desta forma, o objectivo do presente trabalho consistiu em desenvolver e testar sensores eletroquímicos à base de elétrodos de grafeno induzido por laser (LIG) diretamente inscritos em fibras óticas. Os sensores foram aplicados na deteção de nitritos em concentrações relevantes para a aquacultura.
Primeiramente, a produção de LIG foi estudada através da conversão fototérmica da poliimida com potências de laser de 2.5 W e 4 W. Além disso, foram testados dois tipos de geometrias, um onde LIG foi produzido em todos os 360° da fibra, e outro onde LIG foi produzido com apenas uma passagem do laser. Os sensores foram revestidos com nanopartículas de ouro (AuNPs), pela técnica de *dropcasting*, a fim de aumentar a sensibilidade aos nitritos.
Através da análise SEM e Raman, LIG produzido a 2.5 W parece ser próximo do limiar de formação de LIG, apresentando uma morfologia heterogénea. Em contraste, 4 W LIG apresenta uma morfologia homogénea e porosa, cuja influência na sua resposta electroquímica foi evidente nas caracterizações de voltametria cíclica (CV) e espectroscopia de impedância eletroquímica (EIS).
Em particular, estudos de EIS demonstraram claramente o impacto da porosidade do LIG na sua resposta eletroquímica, sendo necessário o uso de modelos equivalentes de linha de transmissão, que consideram efeitos de porosidade, para modelar corretamente a resposta impedimétrica do LIG produzido a 4 W. A estrutura 3D porosa do LIG produzido a 4 W aumenta significativamente a área efetiva de biodeteção, resultando num desempenho superior na deteção de nitritos comparado com o LIG produzido a 2.5 W.
Foram realizados testes de deteção em PBS para diferentes concentrações de $NO_2^-$ com técnica de voltametria de pulso diferencial (DPV), e verificou-se que 4 W LIGs de uma passagem com AuNPs apresentam um LOD medido de 20 $\mu$M, um intervalo linear de 20-200 $\mu$M e uma sensibilidade de (1.93 $\pm$ 0.13) nA/$\mu$M. O sensor foi calibrado de 6.6-8 pH e a resposta de corrente elétrica permanece semelhante, com sensibilidades entre 1.88 nA/$\mu$M e 1.77 nA/$\mu$M, diminuindo ligeiramente com o pH. Os sensores LIG foram testados em amostras reais de água de aquacultura, antes e depois de entrar no RAS (pH = 7.6 e 7.0) e mostraram respostas semelhantes às obtidas em PBS, reportando sensibilidades de (1.86 $\pm$ 0.09) nA/$\mu$M e (1.71 $\pm$ 0.07) nA/$\mu$M, respetivamente, um intervalo linear de 20-200 $\mu$M, que inclui as concentrações relevantes em aquacultura, e um LOD medido de 20 $\mu$M que é inferior à concentração limite considerada tóxica para os peixes (43 $\mu$M).
O sensor produzido foi testado em conjunto com um sensor ótico de pH em fibra ótica, como prova de conceito de uma plataforma híbrida.

**Keywords** Aquaculture, Nitrites, Electrochemical Sensor, Laser-Induced Graphene, Optical Fiber, Lab-on-Fiber, Hybrid Transduction

**Abstract**

Monitoring multiple water quality parameters, such as nitrites ($NO_2^-$) concentration, is vital to provide well-being and growth in fish. Optical fibers show great potential in aquaculture, due to the possibility of multiplexing sensor elements along the fiber, enabling multi-parametric in-situ measurements. On the other hand, electrochemical sensors are equally interesting in this context due to their low-cost and high sensitivity in the detection of various biochemical parameters, such as organic or inorganic contaminants, and even pathogens. The combination of electrochemical with optical detection can be extremely useful towards the development of lab-on-fiber concepts miniaturized for a wide monitoring of the water quality. This way, the goal of the present work consisted in developing and testing electrochemical sensors, based on laser-induced graphene (LIG) electrodes directly scribed on optical fibers. The sensors were applied for the detection of nitrites in concentrations relevant to aquaculture.

First, the production of LIG was studied by photothermally converting polyimide with laser irradiating powers of 2.5 W and 4 W. In addition, two types of geometries were tried, one where LIG was produced in all the 360° of the fiber, and other where LIG was produced with only one laser passage. The sensors were coated with gold nanoparticles (AuNPs), by dropcasting technique, in order to enhance the sensitivity to nitrites.

Through SEM and Raman analysis, 2.5 W produced LIG appears to be near the LIG formation threshold, presenting a heterogeneous morphology. In contrast, 4 W LIG presents a homogeneous and porous morphology, whose influence on its electrochemical response was evident in cyclic voltammetry (CV) and electrochemical impedance spectroscopy (EIS) characterizations.

Specifically, EIS studies clearly demonstrated the impact of LIG's porosity in its electrochemical response, making it necessary to use equivalent transmission line models, which consider porosity effects, in order to correctly model the impedimetric response of LIG produced at 4 W. The 3D porous structure of LIG produced at 4 W increases significantly the effective biodetection area, resulting in superior performance when detecting nitrites, compared to LIG produced at 2.5 W.

Detection tests were performed in PBS for different concentrations of $NO_2^-$ with differential pulse voltammetry (DPV) technique, and it was found that 4 W LIGs of one passage with AuNPs present a measured LOD, of 20 $\mu$M, a linear range of 20-200 $\mu$M and sensitivity of (1.93 $\pm$ 0.13) nA/$\mu$M. The sensor was calibrated from 6.6-8 pH and the current response remains similar, with sensitivities between 1.88 nA/$\mu$M and 1.77 nA/$\mu$M, slightly decreasing with pH. The LIG sensors were tested in real aquaculture water samples, before and after entering RAS (pH 7.6 and 7.0), and showed similar responses to those of PBS, with sensitivities of (1.86 $\pm$ 0.09) nA/$\mu$M and (1.71 $\pm$ 0.07) nA/$\mu$M, respectively, also reporting a linear range of 20-200 $\mu$M, which covers the relevant concentrations in aquaculture, and a measured LOD of 20 $\mu$M which is lower than the threshold concentration considered toxic for fish (43 $\mu$M).

The produced LIG sensor was tested together with an optical pH sensor in optical fiber, as proof-of-concept of a hybrid platform.

# Contents

**List of Figures** i

**List of Tables** iv

**List of Acronyms** v

**1 Introduction** 1
1.1 Motivation and Objectives . . . 1

**2 Theoretical Principles and State of the Art** 3
2.1 Nitrite detection . . . 3
2.1.1 Nitrites in aquaculture ecossystems . . . 3
2.1.2 Nitrite current detection methods . . . 4
2.2 Optical fibers . . . 7
2.2.1 Coatings . . . 8
2.3 Graphene . . . 9
2.3.1 Laser-induced graphene (LIG) . . . 11
2.4 Electrochemical sensors . . . 14
2.4.1 LIG and electrochemistry . . . 16
2.5 Hybrid Sensors . . . 17

**3 Experimental Implementation and Characterization** 19
3.1 LIG production on PI-coated Optical Fiber . . . 19
3.2 SEM and Raman Characterization . . . 20
3.3 Electrical contacts . . . 20
3.4 Electrochemical Characterization . . . 21
3.4.1 Ciclic Voltammetry . . . 22
3.4.2 Electrochemical Impedance Spetroscopy . . . 23
3.5 Nitrite Detection . . . 24
3.6 Hybrid Platform . . . 26

**4 Results and Discussion** 28
4.1 Morphologic Characterization . . . 28
4.1.1 SEM . . . 28
4.1.2 Raman . . . 31
4.2 Electrochemical Characterization . . . 32
4.2.1 CV . . . 32
4.2.2 EIS . . . 34
4.3 Nitrite Detection . . . 36
4.4 Hybrid Sensor . . . 40

**5 Conclusions and Future Work** 42

**Bibliography** 43

# List of Figures


1.1 Recirculating aquaculture system, with sensor elements (red circles) on a single optical fiber placed on the tanks, for multi-parametric monitoring. . . . . 2

2.1 Nitrogen cycle, where the nitrification process of ammonia to nitrite and then nitrate is shown. Retrieved from [17]. . . . . 4
2.2 Optical fiber structure, in a perspective view, and Representation of transmission of light in optical fibers, due to total internal reflection. . . . . 7
2.3 Schematic illustration of the Polyimide (PI)-coated Fiber Bragg Grating (FBG) humidity sensing mechanism, where $\Lambda$ is the FBG period and $\lambda_B$ is the Bragg wavelength. . . . . 9
2.4 Graphite structure, with multiple stacked graphene layers. Graphene is a planar layer of carbon atoms bonded in a hexagonal lattice. Oxygen-containing functional groups appear due to oxidation and strong acids, forming graphene oxide. . . . . 10
2.5 Schematic illustration of LIG production, with photothermal reaction taking place on PI film, disrupting several bonds and leaving behing carbon rings, forming graphene. Typical chemical structure of PI retrieved from [66]. . . . . 11
2.6 (**a**) TEM image taken at the edge of a Laser-Induced Graphene (LIG) flake, with scale bar of 2 nm, displaying polycrystalline structure with many grain boundaries; (**b**) TEM image of the area indicated by the red square, showing a hexagon and pentagon-heptagon hybrid lattice, with scale bar of 0.5 Å. Image retrieved from [64]. . . . . 12
2.7 Schematic diagram of main sensing principles and applications of LIG. . . . . 13
2.8 (**a**) Schematic diagram of pyrolytic graphite showing atomically ordered hexagonal planes, "basal planes", and edge plane like-sites/defects; (**b**) Typical Scanning Electron Microscopy (SEM) image of LIG, with the yellow rectangle representing a zoomed porous structure, where electrolyte can penetrate and promote HET, and Nanoparticles (NPs) can be deposited. Original SEM images retrieved from [100]. . . . . 17
2.9 Hybrid sensor diagram retrieved from [105]. . . . . 18

3.1 Scheme of LIG-on-fiber samples production. . . . . 19
3.2 Scheme of production of the electrical contacts of the working electrode (LIG). . . . . 21
3.3 Schematic diagram of the experimental setup used for both electrochemical characterization of LIG electrodes and nitrite detection. . . . . 21
3.4 Typical voltammogram of reversible reduction of 1mM $Fc^+$ solution to Fc, with various points from A-G represented (left), and applied potential as a function of time, with initial (A), switching (D) and end (G) potentials represented (right). Retrieved from [96]. 22
3.5 **a)** Negatively charged electrode, where countercations are aligned along its surface. The electrochemical processes here are modeled by the Randles equivalent circuit, at bottom left. **b)** Typical Nyquist plot a planar electrode. Abbreviations: $C_d$, double-layer capacitor; ; IHP, inner Helmholtz plane; OHP, outer Helmholtz plane; $R_p/R_{ct}$, polarization (charge-transfer) resistance; $R_s/R_\Omega$, series resistance [95, 112]. . . . . 23
3.6 **a)** - Staircase-shaped pulsed signal of potential applied over time, characteristic of Differential Pulse Voltammetry (DPV), showing its parameters; **b)** - Current response $\delta$i corresponding to the difference between the two sampled current values, where the peak current is proportional to analyte concentration. Modified from [95]. . . . . 25
3.7 Dropcasting technique of Gold Nanoparticles (AuNPs) onto the LIG electrode. . . . . 26

3.8 Hybrid sensing platform containing the LIG nitrite sensor in the usual electrochemical cell and the Polymeric Optical Fiber (POF) pH sensor placed in the bottom of the cell. 27

4.1 SEM images with 1kx magnification, of LIG on optical fiber produced in 360°, at **a)** 2.5 W, **b)** 4 W and **c)** 4 W in cross-section, where D1 refers to the cladding diameter. 28
4.2 SEM images of LIG on optical fiber produced at 1 passage and 4 W, with **a)** 1.5 kx magnification and **b)** 5 kx magnification. . . . . 29
4.3 Energy Dispersive X-Ray Spectroscopy (EDX) spectrum in **b)** of the LIG area outlined by green square in **a)**. EDX spectrum shows the peaks's intensities, in counts, as a function of x-ray characteristic energy transitions, in keV, which are named on top of the spectrum as KA or LA. . . . . 30
4.4 EDX spectrum in **b)** of the LIG area outlined by green square in **a)**, with an evident Au peak, Au-MAB, outlined by an orange circle. In the bottom image of **a)** a spatial distribution of these deposited AuNPs in the SEM image is shown in orange. . . . . 30
4.5 Raman spectra of 2.5 W and 4 W LIG-on-fiber electrodes, with the LIG characteristic peaks identified. A Gaussian-Lorentzian fitting was applied for both spectra, as represented by the dashed lines. An extra dashed line appears in 2.5 W, referring to the a-C peak of amorphized carbon. . . . . 31
4.6 **a)** Cyclic Voltammetrys (CVs) performed with scan rate of 50 mV/s, of 2.5 W, 4 W and 4 W LIG with AuNPs. **b)** Scan rate study, from 5 to 500 mV/s, of 4 W LIG/AuNPs. The inset graph shows both the peak anodic and cathodic current of the three tpes of LIG electrodes, plotted against the (scan rate)$^{1/2}$, with linear fittings applied. . . . . 33
4.7 Nyquist plots containing EIS spectra of: **a)** LIG of 4 W and 4 W with AuNPs, with bias of 90mV vs. SCE and three fitting models applied to the data; **b)** LIG of 4 W with AuNPs, for three different bias: 0, 90 and 180 mV vs. SCE, and four fitting models applied. The inset graphs represent a zoomed view ot the EIS plots, for low values of $Z_{re}$. . . . . 34
4.8 Schematic representation of the LIG-electrolyte interface and equivalent circuits models employed: **a)** Modified Randles model, where the diffusion layer increases as the electron transfer occurs; **b)** Bisquert Open model, where circuit elements are repeated along the pore depth. . . . . 35
4.9 **a)** Exponential fitted baselines applied to blank DPV and 50 $\mu$M $NO_2^-$ data, with its anchor points located to the left and right of the nitrite potential region. The OER tail increases in an exponential fashion. Inset graph contains the subtraction of blank DPV with the baseline, yielding residual currents that reaches $\sim 2.5\times 10^{-8}$A. **b)** Comparison of laser and DPV parameters on the LIG electrodes, regarding electrochemical performance and detection of nitrite concentration. . . . . 37
4.10 Electrochemical responses of LIG sensor for several nitrite concentrations, regarding three different pHs of PBS solution, in **a)**, and two real water samples, before (inlet) and after (outlet) entering the aquaculture tank, in **c)**. Graphs of the peak currents plotted against the $NO_2^-$ concentrations introduced in PBS, for its three different types of pH, in **b)**, and for intlet and outlet samples, in **d)**. Error bars show the variability in results from three LIG sensors, and linear fittings were applied to view the linear range and sensitivity of the sensor. . . . . 38
4.11 Monitoring of the optical signal's peak evolution as nitrites are added in three instants, in steps 0f 50 $\mu$M.'H. Start' and 'H. Stop' stand for homogenize start and stop, respectively, and 'P. Start' and 'P. Stop' stand for the beginning and end of the potentiostat measurements, respectively. Image shared with permission from the owner. . . . . 40

# List of Tables

2.1 Brief list of electrochemical sensors for nitrite detection found in the literature. . . . . 6

3.1 CV and DPV parameters used for nitrite detection measurements, along with each nitrite concentration solution. . . . . 25

4.1 Comparison between the Nitrites ($NO_2^-$) concentrations obtained with calibration plots of 7.5 and 8 pH, and the real $NO_2^-$ value. . . . . 41

# List of Acronyms

**$[Fe(CN)_6]^{4-}$** Ferrocyanide. 16, 32, 33, 42

**AOB** Amonia-Oxidizing Bacteria. 3

**AuNPs** Gold Nanoparticles. ii, 6, 17, 20, 23–26, 29, 30, 32–35, 37, 38, 42, 43

**BTO** Bisquert Open. 34–36

**CE** Counter Electrode. 14, 21, 22

**CL** Chemiluminescence. 5

**$Cl^-$** Chloride. 4, 5, 14

**CNTs** Carbon Nanotubes. 6, 9, 17, 43

**$CO_2$** Carbon Dioxide. 1, 11, 12, 19

**CV** Cyclic Voltammetry. iii, iv, 2, 16, 22–25, 32–34, 42

**DPV** Differential Pulse Voltammetry. ii–iv, 2, 16, 24, 25, 36–40, 43

**$E^0$** Standard Potential. 14, 15, 22, 35

**$E_{1/2}$** Half-wave Potential. 22, 25, 35

**EDX** Energy Dispersive X-Ray Spectroscopy. iii, 20, 29, 30, 42

**EIS** Electrochemical Impedance Spectroscopy. 2, 15, 23, 24, 33–35, 42

**FBG** Fiber Bragg Grating. ii, 8, 9, 26, 27, 43

**GO** Graphene Oxide. 6, 8–10, 17

**Gr** Graphene. 6, 9, 14

**IR** Infrared. 11–13, 20

**LIG** Laser-Induced Graphene. ii, iii, 1, 2, 6, 11–13, 16, 17, 19–21, 23–40, 42, 43

**LOD** Limit of Detection. 6, 17, 39, 42, 43

**LoF** Lab-on-Fiber. 1, 43

**MMF** Multimode Fiber. 7, 8

**$NH_3$** Ammonia. 3

**NO** Nitrogen Oxide. 5

**$NO_2$** Nitrogen Dioxide. 4, 5

**$NO_2^-$** Nitrites. iv, 3, 4, 36, 38, 40, 41, 43

**$NO_3^-$** Nitrate. 3, 4

**NPs** Nanoparticles. ii, 6, 8, 17

**OER** Oxygen Evolution Reaction. 6, 36–38, 43

**PBS** Phosphate Buffer Saline. 21, 23–27, 32, 34, 36, 38–40, 42

**PI** Polyimide. ii, 1, 2, 8, 9, 11–13, 19, 20, 28, 29, 33, 37, 42, 43

**PMMA** Poly(methylmethacrylate). 8, 43

**POF** Polymeric Optical Fiber. iii, 8, 26, 27, 40, 43

**$R_s$** Series Resistance. 24, 34

**$R_{ct}$** Charge-Transfer Resistance. 24, 34, 35

**RAS** Recirculating aquaculture systems. 1, 3, 4, 26

**RE** Reference Electrode. 14–16, 21

**rGO** reduced Graphene Oxide. 6, 8–10

**RI** Refractive index. 7, 8

**SCE** Standard Calomel Electrode. 14, 21

**SEM** Scanning Electron Microscopy. ii, 2, 17, 20, 28–31, 37, 42

**SMF** Single-Mode Fiber. 7, 8, 19, 26, 27

**SOF** Silica Optical Fiber. 8

**SPR** Surface Plasmon Resonance. 8, 18, 43

**UV** Ultraviolet. 1, 5, 12, 13, 20, 26, 27

**WE** Working Electrode. 14–16, 18, 20–22, 24, 27

# CHAPTER 1

# Introduction

## 1.1 Motivation and Objectives

Sensor technology and predictive data analysis are of utmost importance in progress of society, being possible to continuously monitor different parameters in which the human being interacts daily, from food to well-being to security. To respond to this diversity of parameters to be measured, there is a growing need of intelligent and increasingly sensitive and selective sensors, also in the area of aquaculture, which will be addressed in this work.

Goals 2 and 14 of the United Nation's Sustainable Development Goals for 2030 aim to "eradicate hunger, achieve food security and improved nutrition and promote sustainable agriculture" and "conserve and sustainably use the oceans and marine resources for sustainable development" [1]. With the world population increasing and consequent increase in fish consumption, it is expected that this consumption, by 2050, will grow well above the production capacity of the oceans and seas, so aquaculture has emerged as an opportunity and a need to respond to this increase in consumer demand, as it currently already produces more fish for human consumption than fishing [2].

Aquaculture refers to the cultivation and production of aquatic organisms, under certain controlled conditions implemented throughout their life cycle, usually in aquatic tanks. Recirculating aquaculture systems (RAS) are an almost closed circuit, where water recirculates between the fish culture and water treatment stages, such as a mechanical filter (solid waste removal), biofilter (ammonia and nitrite conversion), degassing tower ($CO_2$ removal), oxygen supply and UV disinfection (of bacterias and viruses), among others [3, 4]. This system, illustrated in Figure 1.1 reuses the water used for production, limiting water requirements and isolating fish production from external environments. Despite these advantages, water tanks are usually small and have a high fish density which can be prone to spreading diseases if water quality and feed intake aren't carefully controlled [3, 5]. Due to the system's complexity, where fish biomass and water chemistry interact with each other, small variations of parameters such as pH, temperature, oxygen concentration and nitrites, among others, result in sub-optimal conditions on fish health, inducing stress and potentially death [3, 5].

Therefore, to ensure good food quality for human consumption, it is highly desirable for RAS to have a network of autonomous in-situ sensors, in order to provide real-time data of these multi-parametric measurements. Currently there are no sensitive, low-cost commercial products that perform these measurements directly in the water tanks.

The project in which this thesis is included, DIGIAQUA, aims to develop innovative sensors integrated in a miniaturized prototype to monitor and detect different critical parameters in water tanks. It would be a hybrid platform (optical and electrochemical transduction), in-situ, where it would safely detect parameters at various points along an optical fiber, as shown in Figure 1.1 [6]. This sensing format is called Lab-on-Fiber (LoF), which consists of transforming a simple optical fiber into a multi-functional sensor, by integrating materials and devices miniaturized at the micro and nano scale [7, 8].

The main objective of this thesis concerns the development of a proof-of-concept sensor, based on producing LIG directly on the PI coating that covers the optical fiber, for the electrochemical detection of different nitrite concentrations relevant in aquaculture water. From the various electrochemical sensors investigated in the literature, currently no reports were found on production of LIG on polyimide coating optical fibers, let alone for nitrite detection. Only in the present year did Hou

et. al [9] produce an optical fiber sensor based on LIG for humidity detection, but in this case the polyimide (concretely Kapton sheets) coating was added and transformed into LIG after the optical fiber production.

Thus, the innovation in this thesis is in proving the feasibility to create electrochemical sensors on the exterior surface of commercial optical fibers that already contain PI in its surface for LIG conversion, and detect nitrites in a quick, low-cost and reproductible way.

To do this, in this work, firstly several lasing parameters were used to scribe LIG on the optical fiber, followed by its morphologic and structural characterization with SEM and Raman techniques, in order to analyse which parameters optimize production of quality LIG. Then, electrical contacts were made on the optical fiber, originating the LIG working electrode. These were also characterized electrochemically with potassium ferrocyanide trihydrate, with CV and Electrochemical Impedance Spectroscopy (EIS) tecnhiques, intending to understand the effect of LIG morphology on its electrochemical performance. After that, several electrochemical detections were performed for different nitrite concentrations with DPV technique, aiming to investigate the sensor's detection limit, its reproducibility, the influence of pH changes on nitrite detection and its adequacy in detecting nitrites on real tank water samples.

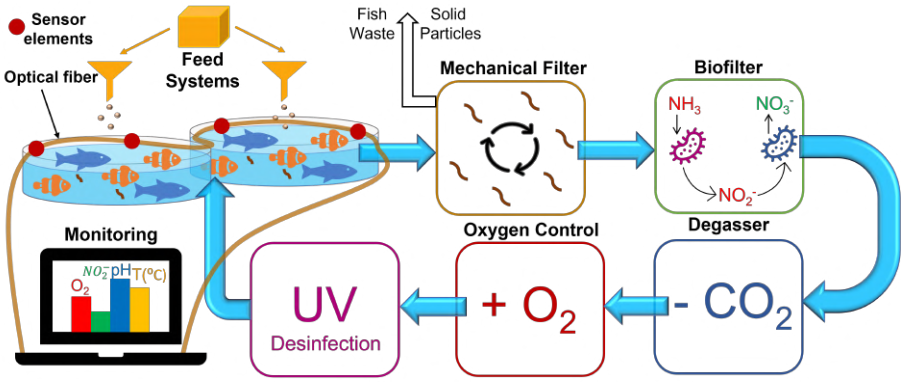


**Figure 1.1:** Recirculating aquaculture system, with sensor elements (red circles) on a single optical fiber placed on the tanks, for multi-parametric monitoring.

The production of these LIG-on-fiber electrochemical sensors open doors to the creation of multi-parametric hybrid sensors of electrochemical and optical transduction. This dual-mode measurement is advantageous, as it can provide counterproof, where information given by the electrochemical sensor and optical sensor of the same analyte can be exchanged to avoid false results (false negative/positive) and gain reliability. Therefore, another objective in this thesis is the creation of a multi-parametric hybrid sensing platform, where the LIG electrochemical sensor is combined with a pH optical fiber sensor and measurements are taken simultaneously, in order to investigate possible influence of pH in nitrite values, and vice-versa. Long-term objectives include placing this hybrid sensing system on the same optical fiber line, which could also enable the investigation of the optical signal of nitrites and cross its information with the LIG sensor.

# CHAPTER 2

# Theoretical Principles and State of the Art

## 2.1 Nitrite detection

### 2.1.1 Nitrites in aquaculture ecossystems

$NO_2^-$ are a commonly found ion in the food industry, acting as a preservative, as well as in environmental samples such as water and soil, due to misuse of inorganic fertilizers in modern agriculture [10]. This also results in excessive amounts of nitrites in vegetables and fruits, posing a threat to human health, as nitrites are deemed a dangerous species for its known toxicity [11]. Specifically, nitrites have the ability to bind with blood pigments, causing an irreversible transformation of haemoglobin to methemoglobin in the blood stream. This hinders the haemoglobin's ability to exchange oxygen, compromising oxygen transport to body tissues [10, 11]. Furthermore, nitrites were added by the World Health Organization to the list of carcinogens, since they can react with secondary amines and amides in the stomach to form N-nitrosamines, known cancer biomarkers [12].

Nitrites are potentially even more toxic to aquatic animals, such as fish and crustaceans [13]. In aquaculture facilities, high nitrite levels are often found, generally due to the increasing need for growth and production of fish. Excessive feeding along with higher fish density in aquaculture tanks results in increased amounts of fish waste, where Ammonia ($NH_3$) is the main product of this metabolism of fish [14]. This is part of the nitrogen cycle in aquatic environments, where the next step consists in the removal of ammonia from the tanks, since it's toxic to fish, by oxidizing it to nitrite through a nitrification process. In closed RASs, this aerobic process is done with a biofilter, where it houses Amonia-Oxidizing Bacteria (AOB), called *Nitrosomonas* [14,15]. However, since nitrites are also very toxic to fish, the nitrification process continues with AOB, called *Nitrobacter*, transforming nitrite into low toxic Nitrate ($NO_3^-$) through oxidation.

$$NH_3 + O_2 \rightarrow NO_2^- + 3H^+ + 2e^- \ (Nitrosomonas) \tag{2.1}$$

$$NO_2^- + H_2O \rightarrow NO_3^- + 2H^+ + 2e^- \ (Nitrobacter) \tag{2.2}$$

The nitrate will be used by plants to produce oxygen for fish and help balance pH [14]. This process of removing waste ammonia and nitrites is not instantaneous nor perfect due to several factors, including the biofilter inefficacy and water quality parameters [5]. Therefore, nitrite remains available in water as an intermediate species of this process and its concentration often increases, reaching toxic levels to fish of 2 mg/L ($\sim$ 43.47 $\mu$M) and even reaching 46 mg/L (1 mM), with mass fish mortality as the likely result in this case [16].

Aquatic animals are more susceptible to high nitrite concentrations than other animals, since nitrite enters the fish mainly by diffusion through the skin and gills, accumulating high concentrations in the blood stream [13]. This affects the blood oxygen-carrying capacity the same way as humans, oxidizing iron in haemoglobin to form methaemoglobin, threatening to fish life if concentrations are over 50% of blood constitution [16]. Visible symptoms of high methaemoglobin levels (starting at 20%) are brownish color of blood and gills and a gasping behaviour of fish at the surface of the water due to oxygen starvation [5]. Other physiological consequences of nitrite toxicity and induced stress include reduced fish growth and feed intake, osmoregulatory dysfunction of gills, lower reproductive performance, weakening of immune system with higher risk of infections, and ultimately death if

exposed long enough with relatively high concentrations [14,16]. This was corroborated by Svobodová et.al [5], where part of fish stock, after several days, died due to high nitrite concentrations in water, about 2 mg/L, and 82% of methaemoglobin in blood. This occurred due to high fish density in a small volume tank and inadequate biofilter efficacy, when oxidizing Nitrogen Dioxide ($NO_2$) to $NO_3^-$.

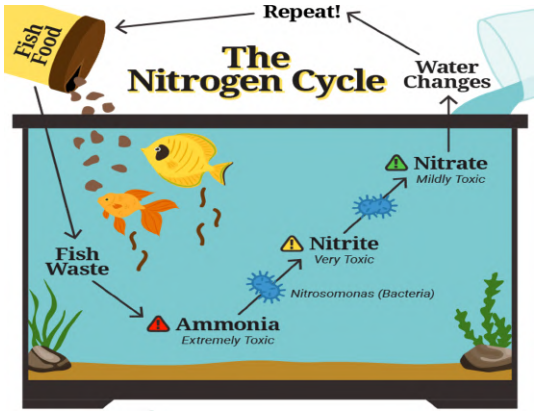


**Figure 2.1:** Nitrogen cycle, where the nitrification process of ammonia to nitrite and then nitrate is shown. Retrieved from [17].

Nitrite toxicity in fish is dependent upon external and internal factors, such as duration of nitrite exposure (24 to 48 hours for maximum accumulation of nitrite), fish species, fish size and age, as well as water quality parameters, such as pH, temperature, chloride, dissolved oxygen, cations, anions and ammonia, among others [16]. For example, an increase in Chloride ($Cl^-$) concentration protects from nitrite toxicity, thus it's important to monitor the $Cl^-/NO_2^-$ molar ratio in aquaculture. As for pH, within the natural pH range in water, the effect it has on nitrite toxicity is minute but a large change in pH can alter the ion diffusion process and consequently nitrite intake in fish [14]. Regarding temperature, Huey et. al [18] reported that fish kept at 30 °C in the presence of 0.9 mg/L of nitrite developed twice the methaemoglobin concentration as the same fish kept at 10 °C.

Since small variations of these parameters are prejudicial to fish (and consequently human) health, a network of autonomous in-situ sensing tools is desirable in RAS, in order to provide real-time data of not only nitrite concentrations, but also key water indicators such as pH, temperature, oxygen and nutrient concentrations [19].

### 2.1.2 Nitrite current detection methods

Nitrite toxic effects and its excessive amount in water and food products are a significant environmental and public health concern. Thus, there is a rising need of highly sensitive, selective and cost-effective sensors able to determine nitrite concentrations.

Numerous analytical methods have been developed over the past 20 years, normally using either optical or electrochemical transducers. These methods include spectrophotometric, chemiluminescent, spectrofluorimetric, biosensing and electrochemical detection [11].

The most widely established method for determination of nitrite has been colorimetric spectrophotometry because of its simplicity, cost-effectiveness and feasibility [11]. Miranda et.al [20] used the modified Griess assay reaction, the most frequent approach in spectrophotometry to determine nitrites. The Griess Assay's main principle is the diazotisation of an appropriate aromatic amine, such as N-(1-Naphthyl)ethylenediamine (NED), by acidified nitrite [11]. This converts the amine into its correspondent diazonium salt (organic compounds that share a common functional group), resulting in a highly coloured azo dye [21]. The absorbance of this solution is analyzed by measuring the intensity of light that passes through the sample solution, in the range of 500-600 nm. This measured absorbance, according to Beer's Law, is proportional to nitrite concentration and can thus be

quantified [11, 21]:

$$A = \varepsilon b C \tag{2.3}$$

Where A is the absorbance, $\varepsilon$ is the molar absorptivity, $b$ is the length of light path and $C$ is the concentration of the analyte. Despite being a pratical choice, the Griess Assay method is time-consuming, shows poor sensitivity and suffers interference from other ions such as $Cu^{2+}$, $Fe^{3+}$, $S^{2-}$ and $I^-$, which affect its accuracy. Nowadays, this issue is mostly resolved however they rely on modern equipment that is quite expensive [11].

Chemiluminescence (CL) is another method that's been applied in recent years in food samples, due to being simple, low cost and showing a wide detection range [11]. It refers to the emission of light as a result of chemical reactions. Regarding nitrite, when it is reduced to Nitrogen Oxide (NO) and then reacts with ozone, nitrogen dioxide is produced in a excited state ($NO_2$*). The excited $NO_2$* then decays to the stable state $NO_2$ and light is emitted above 600 nm [21]. This CL intensity is proportional to the nitrite concentration within a certain range. Since no light source is needed for this technique, background noise is reduced leading to improved detection limits. However, trace amounts of oxygen in the system react with NO to form $NO_2$, decreasing CL intensity. To minimize these interferences, $NO_2$ can be re-converted to NO, however high combustion temperatures (600 °C) are necessary, increasing the overall method complexity [11]

Spectrofluorimetry is similar to chemiluminescence, the main difference being that the electronic excited state and consequent emission of light are products of photon absorption from an incident beam of UV light, rather than chemical reactions [21]. Nitrite itself is not fluorescent, however, when certain fluorescent probes react with nitrite through nitrosation or diazotization, changes in fluorescent intensity occur, either enchancing or quenching it [11]. And these variations are linear with nitrite concentration over a certain range. This method is mainly applied to nitrite detection since it's highly sensitive, reaching very low detection limits of 10 nM [22]. Nonetheless, it suffers from interference of $Cl^-$ ions and removing these ions adds complexity to the process. Additionally, the probes explored so far present low water solubility and are prone to oxidants in the environment, restricting the wide application of fluorimetry [11].

Conventional colorimetric methods require a spectrophotometer, which is not suitable for in-situ measurements due to their large size and difficulty in operation. Thus, a portable, low-cost, fast responding system started being highly desirable for in-situ online nitrite detection [23]. Fiber optic sensors began to be integrated in the aforementioned optical methods, due to the ability of remote analysis, excellent resistance to electromagnetic interferences and water, and easy portability [23]. For instance, fiber optics integration with the spectrophotometry has been reported in [23] and [24], using the Griess method. In both sensors, fiber optics had the function of delivering the excitation light source to the sample cell and collecting light transmitted through the sample. This sample cell was, in [23], a microfluidic capillary waveguide; it is miniaturized and easily coupled with optical fibers. Here the light would interact with the absorbing colored azo dye and intensity of light would change with different nitrite concentrations.

Optical fiber optofluidic, a combination of optics and microfluidics, have a miniaturized integrated structure, meaning that light and fluid are confined to a micro-scale channel allowing for more efficient light-fluid interactions, thus increasing the sensor's sensitivity [25]. These microfluids can be integrated in the microfluidic channels around the optical fiber, as reported in [26], or into the interior of the fiber, as shown in [27]. In [26], a decladded portion optical fiber acts as the sensing region and was inserted into a transparent silica capillary tube, forming the microchannel and, instead of direct light on sample, evanescent waves produced on the fiber core surface interacted with the nitrite-sensitive dye on the microchannel. This sensor improved sensitivity and dynamic range compared with standard spectrophotometry methods, while being low-cost and portable. In [27], an in-fiber optofluidic fluorescence sensor for detection of nitrite was designed with a hollow optical fiber, where the injection of sample volume and chemical reagents is done by etching microholes on the surface of the fiber. This ensures fluorescence quenching due to nitrite's presence inside the fiber.

Despite advantages of miniaturization and ease of use of these optical fiber sensors compared to traditional methods, commercial applications are still unreachable as of today, due to complex microfluid filling technology [25].

Moving on from optical methods, electrochemical sensors are, apart from traditional methods, the most widely investigated analytical technique due to its miniaturization, low-cost, simplicity and high selectivity [28]. The main sensing mechanism, voltammetric/amperometric, relies on the eletrochemical oxidation of nitrite while a potential is applied to the working electrode. This reaction involves the production of nitrate and transfer of two electrons to the electrode, producing a current signal [10]. This electric signal is proportional to nitrite concentration, within a certain range, and the sensor is able to quantitatively measure nitrite. The rate of oxidation reaction and its potential depends on the electron transfer kinetics of electrode materials [12]. Nitrite is electroactive at different electrodes, such as platinum (Pt), gold (Au), copper (Cu), silver (Ag) , glassy carbon (GC), among others [10]. Bare electrode applications are limited since the electrode surface is prone to interferent species, decreasing sensitivity and selectivity. Thus, modified electrodes with functional nanomaterials, namely metal NPs , such as Au, Ag and Pt, or carbon nanomaterials, such as Carbon Nanotubes (CNTs), Graphene (Gr), Graphene Oxide (GO)) or enzymes, started being the main focus of research due to their electrocatalytical activity, with significantly increased detection range and lower Oxygen Evolution Reaction (OER) impact [11, 28].

Numerous nitrite sensors were reported in water samples and aquatic environments, combining metal NPs with carbon nanomaterials. For instance, Fu et.al [29] embedded Pd NPs onto a layer of rGO placed on a glassy carbon electrode. The Pd/rGO/GCE electrode showed no interference in detecting nitrite when exposed to interfering ions and exhibited a range of detection of 1-1000 $\mu$M and Limit of Detection (LOD) of 0.23 $\mu$M. Afkhami et al. [30] developed a modified carbon paste (CP) electrode by electrodepositing Ag NPs onto multi-walled CNTs. The AgNPs/MWCNT/CPE electrode showed a detection range of 0.05-250 $\mu$M and a very low LOD of 0.01 $\mu$M. Recently, a LIG electrode modified with COOH-functionalized MWCNTs and AuNPs was reported by Nasraoui et al. [10] to have a linear range from 10-140 $\mu$M and a LOD of 0.9 $\mu$M.

Most detection limits of these sensors are limited to $\mu$M or mM, which in average are inferior to traditional methods therefore needing to be improved when wanting to detect trace amounts of nitrites [11]. However, it is suitable for most applications, opening doors for these simple, inexpensive and easily miniaturized sensors to be commercially available for the in-situ monitoring of nitrites in water environments [31].

**Table 2.1:** Brief list of electrochemical sensors for nitrite detection found in the literature.

| **Electrode**[a] | **Detection**[b] **Method** | **LOD ($\mu$M)** | **Linear Range ($\mu$M)** | **Sample** | **Ref.** |
|---|---|---|---|---|---|
| Pd-rGO/Glassy Carbon | DPV | 0.23 | 1-$10^3$ | Water | [29] |
| rGO-MWCNTs/Glassy Carbon | DPV | 25 | 75 - $6\times10^3$ | River Water | [32] |
| AgNPs-MWCNT/Carbon Paste | SWV | 0.01 | 0.05-250 | Food, Water | [30] |
| AgNPs/Graphene Oxide | LSV | 2.1 | 10-180 | - | [33] |
| PEDOT/Graphene Oxide | Amperometric | 1.2 | 4 - $2.5\times10^3$ | - | [34] |
| Au-PtNPs/N-doped Graphene | Amperometric | 0.19 | 0.5 - $1.6\times10^3$ | Tap water, Ham | [35] |
| AuNPs/Carbon Nanodots | Amperometric | 0.06 | 0.1 - $2\times10^3$ | Lake water | [36] |
| MWCNT-AuNPs/Laser-Induced Graphene | SWV | 0.9 | 10-140 | Water | [10] |
| **AuNPs/LIG on Optical Fiber** | **DPV** | **20** | **20-200** | **PBS, Aquaculture** | **This work** |

**a** - Pd: Palladium; rGO: Reduced Graphene Oxide; MWCNTs: Multi-Walled Carbon Nanotubes; AgNPs: Silver Nanoparticles; PEDOT: Poly(3,4-ethylenedioxythiophene); Au-PtNPs: Gold-Platinum bimetallic Nanoparticles; N - Nitrogen.
**b** - DPV: Differential Pulse Voltammetry; SWV: Square Wave Voltammetry; LSV - Linear Sweep Voltammetry.

## 2.2 Optical fibers

An optical fiber is a cylindrical structure that transmits light within its transparent core, thus being an dielectric waveguide. This confinement is possible due to total internal reflection, a phenomenon that is allowed to occur because the Refractive index (RI) of the cladding surrounding the core, $n_{cladding}$, is slightly smaller than that of the core, $n_{core}$ [37, 38]. The core and cladding are also usually surrounded by a coating or buffer, that can have either a protective or functional purpose [39]. This typical structure of an optical fiber can be seen in Figure 2.2.

When a light beam propagating in a medium reaches a boundary interface, part of it is reflected and some is refracted to the other medium, according to the law of reflection and Snell's Law, respectively [40]. They are described by the following equations, $\theta_i = \theta_r$ and $n_1 \text{sen}\theta_i = n_2 \text{sen}\theta_t$, where $n_1$ is in this case the core's RI, $n_2$ is the cladding's RI, $\theta_i$ is the angle of incidence that the incident ray makes with the normal of the boundary interface, $\theta_r$ is the angle of the reflected ray, and $\theta_t$ is the angle that the transmitted ray makes with the normal [40].

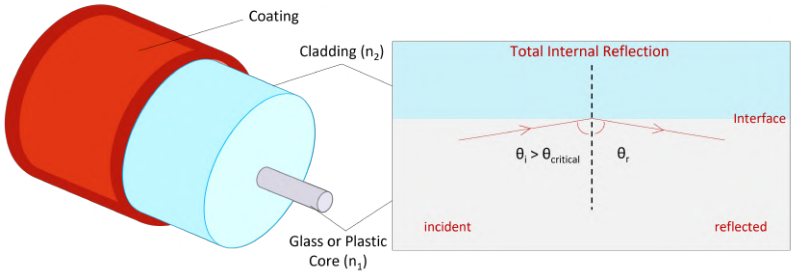


**Figure 2.2:** Optical fiber structure, in a perspective view, and Representation of transmission of light in optical fibers, due to total internal reflection.

By making the RI of the core slightly greater than that of the cladding, according to Snell's Law, if the incident angle is greater than the critical angle (where light travels alongside the interface), the light ray is totally reflected and propagates internally through the core, resulting in low losses of light to the surroundings. This is the principle of transmission of light in optical fibers [39, 41].

An important parameter of an optical fiber is the normalized frequency, also known as the V-number. It defines the cut-off condition for the number of modes allowed to propagate in Multimode Fibers (MMFs), given mathematically by the expression [37]:

$$V = \frac{2\pi a_{core}}{\lambda_c}\sqrt{n_1^2 - n_2^2} = \frac{2\pi a_{core}}{\lambda_c} NA \tag{2.4}$$

Where $a_{core}$ is the core radius and $\lambda_c$ is the wavelength of incident light rays in vacuum. For values of V $\leq$ 2.405 (cut-off frequency), only a single mode can propagate since modes of higher order are cut-off, and the fiber is designated Single-Mode Fiber (SMF), while for V $>$ 2.405 it is called MMF, since propagation is allowed to take in several modes [37].

In fiber optics, the word "mode" in simple terms refers to the path traversed by the propagation of light within the fibers. When eletromagnetic waves are guided along the fiber and reach interface boundaries, phase shifts occur and the waves reflecting inside the fiber interfere with each other. The modes are therefore the discrete number of guided paths that yield constructive interference, in the form of eletric field distributions [42]. As evidenced by equation 2.4, the number of modes that are able to propagate depends on the dimension of the core, the wavelength of the radiation and the RI of the core and cladding.

MMFs have a very large core diameter, from 50-1500 $\mu$m, allowing the propagation of higher modes, coming from different incident angles. In SMFs only the fundamental zero-order mode is transmitted; it propagates along the central axis of the fiber, eliminating errors associated with the

intermodal dispersion. As a result, pulses of information can be transmitted much closer in time without overlapping, giving a SMF a much higher bandwidth than a MMF. Therefore, SMFs are preferable and frequently used in modern long range communication systems [42]. Regarding optical fiber sensors, depending on the application, both SMF and MMF are widely applied. In biosensors, for example, it is usually used single-mode Silica Optical Fibers (SOFs), or multimode POFs. The cladding and core diameter of a SOF is generally 125 $\mu$m and 9 $\mu$m, respectively, while MMF POFs usually have a cladding diameter of 1000 $\mu$m and a core diameter of 980 $\mu$m [38].

As reported above, optical fibers can be fabricated with different materials, SOFs, which were the first fibers used in the field of sensing, and POFs, which have been used lately in the development of sensors due to advances in POF technology [38]. POFs are usually made of a Poly(methylmethacrylate) (PMMA) core with a fluorinated polymer cladding. Compared to SOFs, they exhibit higher propagation losses throughout the system, however they are mechanically more robust and flexible, with a lower material cost, allowing for considerable cost savings in several applications [43].

### 2.2.1 Coatings

Optical fibers usually have their core and cladding surrounded by a coating, whose main role is to protect the fibers from external factors that can damage the surface, but they can also help optimize optical performance requirements and serve a more functional job.

Functional coatings serve a purpose beyond protection of optical fibers, often optimizing the fiber performance. Due to their material's unique properties they are used for specific applications, predominantly in optical fiber sensors (OFS). In OFS, functional coatings, such as polimeric, can provide a matrix support to fixate the sensing materials, or they can also act themselves as the sensitive elements and enhance the sensor's sensitivity [44]. In temperature sensing, the effective length and refractive index of the OFS changes with temperature variations. Since the fiber is made of silicon dioxide and its thermal expansion and thermo-optic coefficients are small, the thermal sensitivity of the OFS is relatively low. To improve the temperature sensitivity, some materials with higher thermo-optic coefficient, such as the polymer polydimethylsiloxane (PDMS), are coated on the fiber so that when the temperature increases, the size of PDMS will become longer and the length of the FBG inside the fiber will increase, causing a wavelength drift [45, 46].

Polyimide can also have several functional purposes, being mostly used for humidity measurement, and also for cryogenic temperature measurements. PI exists stably in the temperature range of -200 to 300 °C, protecting the structure of fiber sensors by improving the frost resistance of the fiber [45, 47]. Since FBG sensors are itself not sensitive to humidity , one of the ways to increase sensitivity is to coat the FBG with special polymers, such as PI, as reported by Zhang et.al [48]. It has hydrophilic properties, being a good water and moisture absorber, so that when humidity in the measurement environment changes, the overall volume of PI changes and the layer is deformed [45, 48]. This causes a variation in the FBG period and the effective refractive index value, inducing a shift in the FBG Bragg wavelength.

Metallic coatings, such as Au and Ag films or NPs, can also be used as a functional coating in optical fiber biossensors for Surface Plasmon Resonance (SPR) phenomena [41]. SPR generally occurs when the phase matching condition between the incident electromagnetic wave and the surpace plasmon wave of the metal layer coated on the fiber is satisfied. The transmission spectra in the output experiences energy loss at a specific wavelength known as resonant wavelength, due to variations in the surrounding RI [41, 49]. Graphene and its derivatives GO and reduced Graphene Oxide (rGO) also started being introduced in optical fiber sensors, adding it on top of the metal surface to inhibit oxidation [41]. In 2017, Jiang et.al [50] delevoped a localized SPR biosensor, with a U-shape POF covered with an Ag film, AgNPs and graphene, reporting that graphene not only delayed the oxidation process of AgNPs but also enhanced the sensitivity, reaching 700.3 nm.RIU$^{-1}$.

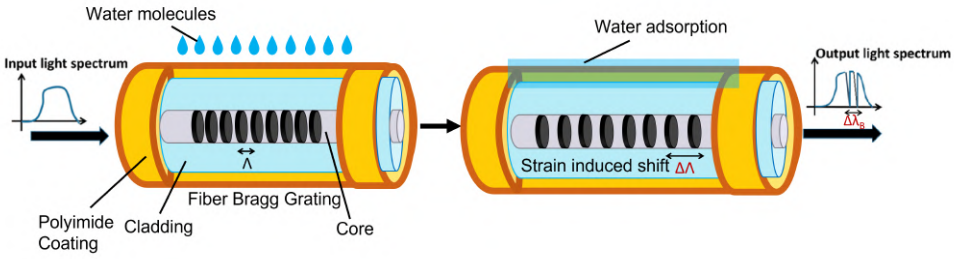


**Figure 2.3:** Schematic illustration of the PI-coated FBG humidity sensing mechanism, where $\Lambda$ is the FBG period and $\lambda_B$ is the Bragg wavelength.

## 2.3 Graphene

Graphene is a carbon allotrope that consists of a single atomic plane of graphite, with each carbon atom bound to three neighbours ($sp^2$ hybridized), in a two-dimensional honeycomb lattice structure [51,52]. The term 'graphene', though, is also generally designated to bilayer or even few-layer graphene films, since the electronic structure remains relatively similar, approaching the 3D limit of graphite at 10 layers [51, 52]. Other 2D carbon materials, such as GO and rGO, are known as 'graphene-based materials'. GO is graphene oxide, a chemically modified graphene that results from the oxidation and following exfoliation of graphite, having many oxygen-containing functional groups in its single-layer structure [51]. The GO can be reduced thermally, creating a diminished oxygen content form of graphene oxide, known as reduced graphene oxide [53].

Graphene, being a free-standing 2D atomic crystal, possesses unique properties such as a zero bandgap semiconductor, extreme mechanical strength and exceptionally high electronic and thermal conductivities [51, 53]. These characteristics have been measured in high-quality graphene obtained from laboratory experiments, many exceeding those obtained in any other material. For instance, the charge carriers intrinsic mobility at room-temperature in mechanically deposited graphene was first reported in [54] to be 10000 $\text{cm}^2\ \text{V}^{-1}\ \text{s}^{-1}$, while suspended graphene with minimal impurity scattering was reported in [55] to have an ultra-high value of $2 \times 10^5\ \text{cm}^2\ \text{V}^{-1}\ \text{s}^{-1}$, the largest value ever reported for a semiconductor or a semimetal.

It was also reported to have a Young Modulus of 1 TPa (Terapascal, a record value) and mechanical breaking strength of 42 N/m, 331 times higher than that of steel [56]. It has the highest thermal conductivity of all materials, on par with diamond and CNTs, of around 5000 $\text{W m}^{-1}\ \text{K}^{-1}$. [57, 58].

In addition, Gr also presents other properties that open doors to a broad range of applications. As an example, it possesses high optical transparency, up to 97.7 %, in the visible range of the spectrum [58].This combined with its decent conductivity makes graphene a possible future replacement of ITO (the standard transparent conductive eletrode with high conductivity) in solar panels or liquid crystal displays, since ITO's supplies are becoming more scarce and expensive [58, 59]. Its mechanical flexibility and chemical durability are also useful in new applications that require flexible electronic devices [58]. Graphene is inert to oxidation and shows a complete impermeability to gases creating a barrier, thus serving as a coating to protect metal surfaces from corrosion [51]. Gr also fulfills many of the requirements of sensing, from interface accessibility to molecular sensitivity, where the electrical and mechanical properties can be of service in the transduction of the sensing signal [59]. Graphene sensors are usually used as chemical sensors, since it has a high specific surface area ($\sim$ 2630 $\text{m}^2\ \text{g}^{-1}$ [60]). Gas molecules adsorbed onto the graphene layer either receive or transfer charges, inducing changes in the carrier concentration and in the electrical resistance [53]. However they can be generally applied to any external factor that is capable of inducing this change, such as a magnetic field or electric charges [59].

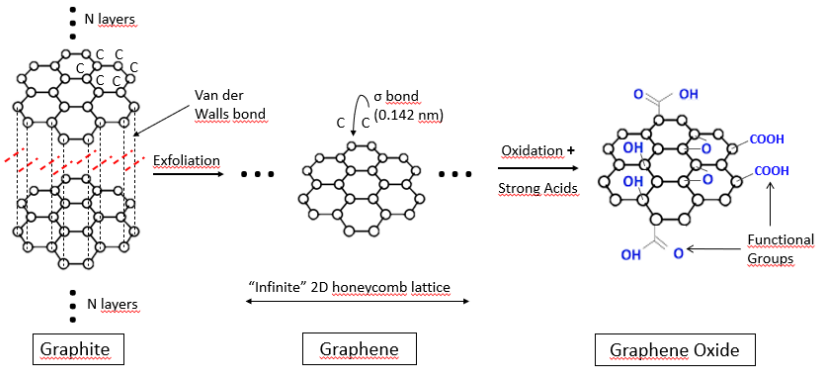


**Figure 2.4:** Graphite structure, with multiple stacked graphene layers. Graphene is a planar layer of carbon atoms bonded in a hexagonal lattice. Oxygen-containing functional groups appear due to oxidation and strong acids, forming graphene oxide.

Graphene was discovered in 2004 by Geim and Novoselov, opening new doors in materials science and physics [54]. Their method of isolating graphene consisted in mechanical exfoliation of a crystalline graphite source, consecutively peeling it to its limit with adhesive tape [51]. This thinned down graphite was then transferred onto a silica wafer with the appropriate color contrast and, through optical microscopy, 2D graphene became visible. Although this method is easy and low cost and produces high-quality one atom thick layer of graphene, it is not suitable for large scale production [59].

In a matter of months, alternatives to graphene synthesis were explored sucessfully, based on the growth of graphene on solid substrates: the epitaxial growth of graphene layers on metal carbides (SiC) by thermal decomposition , or directly on metal surfaces by chemical vapor deposition (CVD) of hydrocarbons [59]. In SiC wafers, the thermal treatment applied at about 1300 °C under high vacuum conditions leads to the sublimation of Si atoms, while the remaining carbon atoms are reorganized and graphitized. By carefully controlling the sublimation process, it's possible to obtain very thin and often uniform films of graphene on the entire wafer, although the control of morphology and adsorption energy is quite difficult, and prices of the substrates are high [51, 59].

Another prominent way to supported growth of graphene consists in decomposition by CVD of hydrocarbons into graphitic materials, on metallic surfaces, since these can efficiently catalyze this process. The metal surface, made of Pt or Cu, is exposed to a mixture of hydrocarbon gaseous reactants, that decompose at high temperatures (about 1000 °C). Carbon atoms are then deposited and diffused into the metal surface. However, by controlling the cooling of the substrate, segregation of carbon atoms happens and large-area graphene layers appear on the surface of the substrate [51,61].

It should be noted that for both the epitaxial growth and CVD, graphene produced must be transferred onto a different substrate, where it will be processed directly for its desired application. To separate the graphene from the copper substrate, hydrolysis is applied electrochemically, forming hydrogen gas bubbles between the materials and exfoliating the graphene from copper [51, 62]. These supported grown methods demand high energy consumption and require expensive templates that are only relevant in high performance applications [59].

There is also Hummer's method of chemical oxidation and exfoliation (peeling off GO layers from graphite), that weakens the van der Waals coesive force between adjacent graphene layers, by inserting oxidizing agents and strong acids in the inter-space [59, 63]. This causes the formation, on the surface of the layers, of different oxygen-containing functional groups, making them hydrophilic and reducing the interlayer forces between the GO sheets [51]. The exfoliation process is then done by inserting the graphite in an aqueous media, via sonication (application of ultrasonic waves in a liquid to agitate particles), until a stable colloidal suspension of GO is achieved [51]. GO is an electric insulator since the bonding network of graphene was disrupted. In order to increase conductivity to values close to those of graphene, GO can be reduced by thermal reduction, producing rGO. However, this reduction

to graphene is only partial, not exhibiting the same eletrical properties [59].

All the referred methods have specific drawbacks which prevent their full commercialization. In order for a production method to be the technology of choice worldwide in the synthesis of graphene/graphene-based materials, it needs to be of low complexity, scalable, economically viable and have a high production throughput, all of that while maintaining a decent quality single-layer graphene. This way, recent new techniques have been developed as alternatives and an attempt to meet these requirements. Focusing on one in particular, Tour et. al [64] in 2014 reported a new method for the synthetization of graphene. It was discovered that by irradiating a commercial PI film with a $CO_2$ Infrared (IR) laser, the PI would transform into three-dimensional porous graphene layers, dubbed Laser-Induced Graphene (LIG).

### 2.3.1 Laser-induced graphene (LIG)

Laser processing has proven to be an effective way to alter the surface of the scribed material, having the ability to quickly change designs and produce complex structures with a precision that can´t be matched with traditional thermal methods [51]. Since it shows compatibility with many materials, laser technology started being explored to obtain graphene-based materials [65]. This recent approach by Tour et. al [64] of producing and patterning porous graphene-based structures meets the demands for industrial use by being straightforward, requiring only a one step IR laser scribing on a PI sheet under atmospheric conditions, thus making it inherently scalable and cost effective.

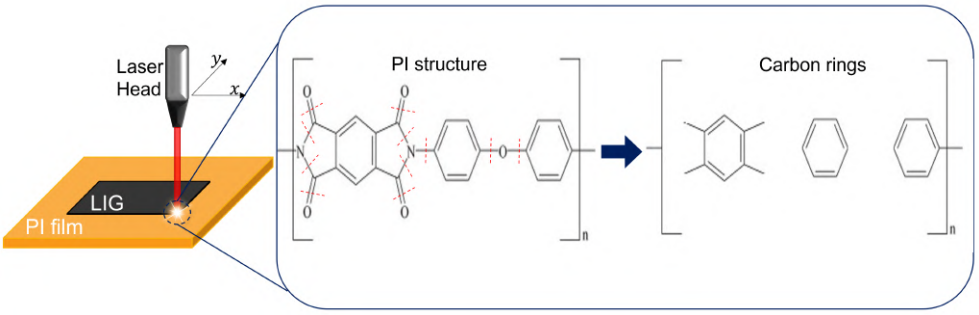


**Figure 2.5:** Schematic illustration of LIG production, with photothermal reaction taking place on PI film, disrupting several bonds and leaving behing carbon rings, forming graphene. Typical chemical structure of PI retrieved from [66].

When Carbon Dioxide ($CO_2$) laser scans the PI, the $sp^3$-carbon atoms in the polymeric substrate are likely photothermally converted to $sp^2$ hybridized carbon atoms, obtaining LIG with high electrical conductivity and good chemical stability [64]. The photothermal effect refers to the temperature increase of a material due to the absorption of light [67]. Specifically, the absorption of energy from laser irradiation induces vibrational perturbations on the lattice of PI, which can lead to high localized temperatures (above 2,500 °C) [64]. This high temperature causes the rearrangement of the PI's molecular structure, easily breaking the C—O, C=O and N—C bonds. Consequently, nitrogen and oxygen gases are rapidly released, forming an overlayer that protects from oxidation, and leaving behind residual carbon rings on the PI surface, characteristic of graphene [64].

At nanoscale, LIG shows polycrystalline layers with disordered grain boundaries, expanding the hexagon lattice, characteristic of graphene, to a hexagon and pentagon-heptagon hybrid lattice [64]. These defects are responsible for the curvature of its graphene layers, causing LIG films to exhibit the appearance of a foam with a 3D porous structure. These porous structures create high accessible surface areas for functionalization with nanomaterials, ensuring flexibility and enhancing electrochemical applications [64].

Tour's report in 2014 tested different polymers to the irradiation of $CO_2$ laser, finding that most polymeric substrates ablate when irradiated; only polyimide and polyetherimide would graphitize and

convert into LIG. Since then, LIG production has been reported mainly on PI but also tried on many materials, showing success on plastic composites and naturally occurring carbon precursors, such as wood [68], food [69], paper [70], among others. The fabrication method is similar, the difference being the laser is scribed multiple times onto the substrate until graphene was formed, sometimes under an inert atmosphere, if necessary, to prevent burning of the biodegradable material [69].

The $CO_2$ IR laser scribing on PI is computer-controlled allowing LIG to be written into various patterns and sizes. Additionally, several laser parameters can also be controlled, such as laser power, scanning speed and spacing between lines, as they have a major influence in the morphology and overall quality of LIG produced.

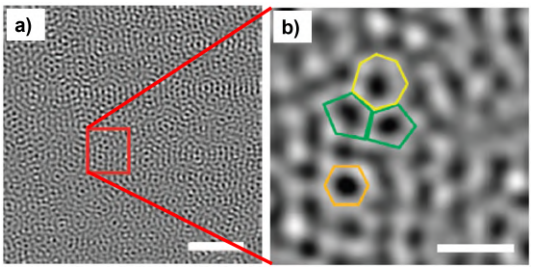


**Figure 2.6:** (**a**) TEM image taken at the edge of a LIG flake, with scale bar of 2 nm, displaying polycrystalline structure with many grain boundaries; (**b**) TEM image of the area indicated by the red square, showing a hexagon and pentagon-heptagon hybrid lattice, with scale bar of 0.5 Å. Image retrieved from [64].

For instance, the laser power effect on LIG was investigated in [64], using powers ranging from 2.4 to 5.4 W. 2.4 W was the minimum value since it has been well-documented that it is the threshold power for laser ablation of polymers. Beginning at this power, it was found that the atomic percentage of nitrogen and oxygen both decrease significantly to less than 3%, while that of carbon increases from 71% in PI to 97% in LIG. Also, when increasing the laser power, the resistance of the PI sheet decreased while its conductivity improved, indicating a better carbonization and crystallinity.

This is corroborated by Duy et al [71], although the laser fluence (optical energy delivered per unit area) is investigated directly instead of laser power. Laser fluence $\phi$ can be approximately calculated by: [72]

$$\phi = \frac{E}{S} \approx \frac{Pt}{dL} \approx \frac{P}{dv_{laser}} \tag{2.5}$$

Where $S$ is the area irradiated by the laser energy $E$, $P$ is the laser power, $t$ is the scanning time, $d$ is the beam diameter, $L$ is the length of line and $v_{laser}$ is the laser scanning speed. It was found that LIG formation starts at about 5.5 J/cm$^2$ and its porosity increases with increase in laser fluence, since photothermal decomposition is intensified [71]. However, increasing too much the laser fluence (and power) and exceeding a certain limit value ($\sim$ 4.8 W) leads to a degradation of quality of LIG, due to partial oxidation in air and presence of more defects [64].

With most studies of LIG production using $CO_2$ IR laser, researchers started turning their attention to different lasers (wavelengths), such as visible [73, 74] and UV laser, wondering if they are also able to fabricate LIG and if so, how it affects its structure and morphology. The first successful production of LIG by a Ultraviolet (UV) laser was demonstrated by Carvalho et. al [75]. An UV pulsed laser of 355 nm was used which, compared to a $CO_2$ laser, has a more focused beam spot. This means a higher spatial resolution, allowing for smaller LIG feature sizes, an advantage in terms of sensor miniaturization [76]. Furthermore, UV irradiation presents a shorter wavelength, meaning that photons irradiated have higher energy, in the same order of magnitude of the atomic bonds energy of PI. Therefore, they are likely able to break these chemical bonds directly (photochemical effect), and not only by a dominant thermal-vibrational process like in IR lasers [75]. However, because single photon energy in UV lasers is much higher and small features demand tightly focused beam spots,

laser parameters must carefully selected in order for the laser fluence to not be high enough to perform destructive abrasion of the PI substrate [77].

Comparative studies between these two types of lasers were made in [76,77], where under the same fluence, both LIGs present similar porous morphologies. However, IR LIG presents a higher density of graphene edges and pores and overall better quality than UV LIG. Applying this findings in a LIG electrochemical sensor of dopamine, Santos et al. [76] reported that, despite UV LIG showing decent sensitivity, IR shows superior values, due to the higher presence of defects and a higher surface porous area, making IR LIG the preferable choice.

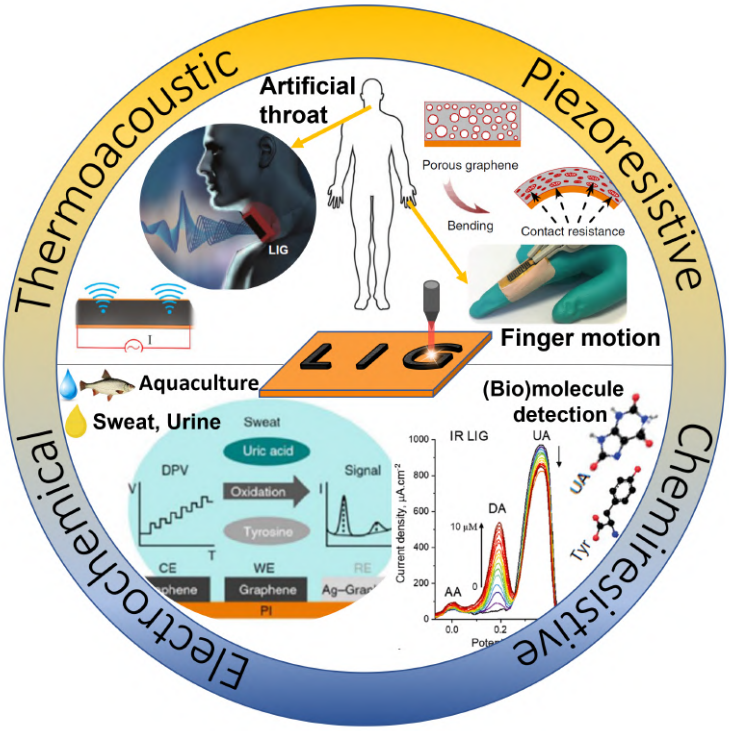


**Figure 2.7:** Schematic diagram of main sensing principles and applications of LIG.

The ability to easily engineer the LIG properties made this a multifunctional material ready to be explored in a many application areas, such as micro-supercapacitors for energy storage devices in wearable electronics, water treatment systems, fuel cell technology, and recently as sensors [67, 78]. There are highly sensitive sensors being developed for the detection of numerous stimuli, illustrated in Figure 2.7. Mechanical sensing is commonly explored in human body-induced strains as a piezoresistive sensor, either monitoring muscle movements [79], such as facial skin expansion [72] and finger motion [79], or detecting physiological signs such as heartbeat pulse [75] and throat sounds [73]. These types of LIG sensors are flexible and wearable, with the intention to provide a personalized healthcare by monitoring real-time daily human activities. Another broad field in LIG sensing is the detection of specific chemicals. Chemical sensors can measure air quality around industries with hazardous gas emissions [80], food quality [81], contaminants in aquaculture [82, 83], and help quantify some important biomolecules, such as acid uric [84], dopamine [85], ascorbic acid [86] and glucose [87] or even bacteria [88]. Usually this sensing occurs from the change in electrochemical response of LIG when adsorbing chemicals, where the resistance, capacitance or charge transfer resistance vary with eletron transfer between the electrolyte and LIG [78]. This is the principle behind electrochemical sensors.

## 2.4 Electrochemical sensors

Since it was discovered that the energy involved in some chemical reactions could be converted to electric energy, and vice-versa, applications of chemical analysis methods involving electrochemical phenomena started being developed. The history of electrochemical sensors started with the development of the glass electrode as pH sensitive membranes, by Cramer in 1906. Later in 1909, Haber applied this idea and performed its characterization as a potentiometric device [89]. The general working principle behind electrochemical sensors relies on electron or ion transfer processes occurring at the interface between the electrode (electronic conductor) and an electrolyte solution (ionic conductor) [90]. This way, it is able to transform the chemical interactions between the analyte and the sensor into a measurable electrical signal. A relation between the electrical signal and the concentration of the target analyte in solution can then be established [91]. By adding concentrations of the analyte to the electrolyte solution, a calibration curve can be plotted and the sensor is ready to detect quantitatively a certain analyte concentration, in the range of detection [92]. The signal transduction can occur in a range of modes of detection, such as potentiometric, amperometric, voltammetric, and impedimetric [89, 93].

Usually, the experimental setups to collect data involve an electrochemical cell, whose schematic representation is presented in Figure 3.3, and inside a two or three-electrodes setup in contact with the electrolyte. The Working Electrode (WE) is where the sensing occurs, its surface serving as the transduction element in the chemical reaction [90, 94].

Since WE is involved in the electrochemical sensing, the different types of electrode material, its dimensions and surface modification are crucial factors that influence the electrochemical response, due to different electron transfer kinetics and changes in surface adsorption of the analyte [95]. As such, common WEs consist of redox-inert material, such as gold, silver, platinum, glassy carbon or Gr, in order to not participate in the reaction and avoid corrosion. These materials have a versatile potential window and are suitable for most sensing applications [89, 95].

Another electrode present is the Reference Electrode (RE), it has well-defined and stable equilibrium potential. It is kept at a distance from the sensing site, thus behaving independently from the properties of the WE and reaction occurring there [94]. Its main function is to provide a reference point against which the potential of the other electrodes can be compared and measured [96]. The internationally accepted reference is the standard hydrogen electrode (SHE), formed by a platinum wire dipped in a strong acid solution, while hydrogen gas is bubbled in [90]. The electric current that passes through the wire will cause hydrogen reduction, and its reduction potential (potential threshold for redox reaction under standard conditions) , $E^0$, is defined by convention to be zero. The WE potential is thus always relative to the defined RE potential. For example, a common Standard Calomel Electrode (SCE) has a potential of 0.242 V *vs.* SHE [90, 95].

When the reduction or oxidation of the analyte occurs, current begins to flow from the WE to the solution, and a Counter Electrode (CE) is used to establish a connection to the electrolyte, closing the electrical circuit [96]. This electrode should also be conductive and chemically stable, typically consisting of a platinum wire [95].

Regarding the electrolyte solution, in most cases an aqueous solution of acids, bases or salts, it is a ionic conductor, meaning that charge is carried by the movement of ions [90]. Ions move in solution to compensate for charge change, as electrons transfer from the WE to the analyte [96]. Mass transfer of the analyte in solutions can occur by diffusion, migration (influence of electric field gradient) and convection. Convection is negligible since the movement of whole volumes of solution doesn't usually take place and migration is minimized by using electrolyte in high concentration. It is therefore dominated by diffusion (influenced by the analyte concentration gradient) [95, 96] . The electrolyte solution situates in between electrodes, and is a mixture of solvent and a supporting electrolyte, where the latter is dissolved in the solvent to produce ionic species, such as hydrogen ($H^+$), sodium ($Na^+$), $Cl^-$, among others [90, 96]. This will increase the conductivity and lower the resistance to charge transfer in the solution. Another important property that an electrolyte should possess is low

chemical reactivity towards redox reactions with the analyte, in the potential range of the experiment, in order to avoid undesirable interference in the electric signal [96].

As previously mentioned, the electric response is varied according to the modes of detection. A potentiometric sensor measures potential between the WE and RE derived from accumulation of charges on the WE interface [94]. The most common electrode used is a ion-selective electrode (ISE), consisting of a membrane that ensures selectivity towards the analyte ion of interest [91]. Measurements are done in open-circuit at zero current, in equilibrium conditions. This way, the ion-exchange reaction is governed by the Nernst equation, a chemical-thermodynamical relationship where the measured electrode potential, E, varies logarithmically with the concentration of the analyte in the solution at equilibrium [89, 95]:

$$E = E^0 + \frac{RT}{z_i F} \ln (a_i) \tag{2.6}$$

Where Standard Potential ($E^0$) is the standard potential of the ion, R is the universal gas constant, T is the absolute temperature, F is the Faraday constant, $z_i$ is the charge number of the analyte ion and $a_i$ is the ion activity. This parameter is the product of ion concentration with the activity coefficient, which for very dilute solutions can be regarded as one [97].

Regarding impedimetric sensors, they rely on impedimetric-based measurements, usually with a selective binding of the analyte to the sensor's surface. The most known technique to characterize these systems is Electrochemical Impedance Spectroscopy (EIS), whose working principle consists of applying a small sinusoidal voltage signal, e, over a dc bias voltage, to the electrochemical cell and measure the resulting current, i, with a phase shift of $\phi$ relative to the applied signal [90, 94].

$$e = E \sin (\omega t), \;\; w = 2\pi f \tag{2.7}$$

$$i = I \sin (\omega t + \phi) \tag{2.8}$$

The current is acquired while sweeping a wide range of perturbation frequencies, f, of the applied potential [94, 95]. The response can be read in terms of impedance, Z, which, according to Ohm's Law, corresponds to the ratio of potential to current in the frequency domain [90, 95].

$$Z(w) = \frac{e}{i} = \frac{E \sin (\omega t)}{I \sin (\omega t + \phi)} \tag{2.9}$$

Current-potential linearity can be assumed since the applied sine-wave perturbation is sufficiently small not to cause a transient signal [95]. Z is a complex impedance, with real ($Z_{Re}$) and imaginary ($Z_{Im}$) components, and can also be written in phasor notation [90]:

$$Z(w) = |Z| e^{-j\phi} \tag{2.10}$$

$$Z(w) = Z_{Re} - jZ_{Im} \tag{2.11}$$

Materials usually don't exhibit pure resistance behaviour, thus the real component of the impedance corresponds to the resistance, R, and the imaginary component corresponds to the capacitive reactance, $X_c$. This can be graphically plotted with a Nyquist plot (example displayed in section 3.4.2), in which $Z_{Re}$ is plotted against $Z_{Im}$, for different values of $w$. [90].

Lastly, amperometric/voltammetric sensors are the most used to derive information about one or more analytes. The working principle of both methods relies on continuously measuring current generated from oxidation or reduction of an electroactive species, as a function of an applied potential [91,94]. In this case, if an external voltage is applied to the WE, the energy of the electrons of the WE surface are modulated. [96] When they have a higher energy than the Lowest Unnocupied Molecular Orbital (LUMO) of the analyte (named A for exemplification purposes), the transfer of an electron to electronic vacant states in A becomes thermodynamically favorable and A is reduced, producing

a reduction current [96]. The resultant peak value of the current measured over a certain range is linearly dependent to the bulk concentration of the electroactive species in analysis [89, 94].

Both methods are controlled potential techniques, the difference between them being that in amperometry, the potential applied between the WE and RE is constant through time, while in voltammetric sensors, potential can be scanned across a certain range of values, or increased in a step-like fashion [89]. Potential sweep methods like linear scan voltammetry (LSV) or CV are advantageous since we can obtain the complete electrochemical behaviour of the system much faster by just scanning once the potential window, instead of through many series of steps to different potentials. However, pulsed voltammetry techniques (step potential) such as square wave voltammetry (SWV) or DPV have a high sensitivity, as well as improve the resolution of redox current signals of multiple electroactive species that might overlap. [98]. DPV, in particular, is very important when detecting analytes, since it is capable of minimizing the contributions of capacitive charging (non-faradaic) currents, augmenting the sensitivity for the faradaic processes, which are of interest [76].

There are two types of phenomenon, faradaic and non-faradaic processes, that compose the current measured in voltammetric measurements. Faradaic processes are related to the redox reactions, where charges are transferred between the WE and the electroactive species, yielding a faradaic current. This is governed by Faraday's Law, that states the rate of consumption of the analyte is proportional to the magnitude of current that flows in the electrode. This current is desirable since we can measure detection of analytes with it [90, 98]. However, other processes that hinder this detection signal occur, called capacitive or non-faradaic processes. Non-faradaic phenomena always happen in solid-liquid interfaces, where the adsorption and desorption of ions in the solution leads to a charged layer in the electrode interface, which attracts opposite charges and creates a double electric layer. It can be considered a kind of capacitor with charge associated to it, and this process yields capacitive currents that interfere with the signal detection, thus needing to be minimized [90, 95].

### 2.4.1 LIG and electrochemistry

LIG has emerged lately as a promising electrode material for electrochemical sensing. One of the reasons relies on it being a graphene-based material that is produced easily and cost effectively, in any desirable two-dimensional shape, which is great for disposable electrodes. In comparison, in screen-printed carbon electrode process, stencils must be prepared every time a design change is required, rendering a more complex production. [82]. Other motives are related to the material's properties and structure that influence electroanalytical performance. Many of graphene's qualities as an electrode material, such as excellent electrical conductivity, high surface area, wide potential window, reversability and high electron transfer rates, are passed onto LIG, with this 3D porous graphene material having better mechanical stability and higher catalytical activity [99, 100].

As previously mentioned, LIG films exhibit the appearance of a foam in the form of a 3D self-standing porous network, resulting from the rapid liberation of gaseous products when laser scribed [64]. These porous structures ensure highly accessible surface areas and facilitate electrolyte penetration into the electrode surfaces, improving electron transfer rates and conductivity [86]. In fact, in several studies the heterogeneous electron transfer (HET) rate ($k^0$) of LIG, for both inner-sphere and outer-sphere redox mediators, Ferrocyanide ($[Fe(CN)_6]^{4-}$) and Hexaammineruthenium ($[Ru(NH_3)_6]^{3+}$), was reported to be significantly higher than the rate for similar carbon-based electrode materials [76, 86].

It is well known in the literature that electron transfer kinetics are considerably enhanced at graphene edge plane sites, due to higher density of defects, when compared to the basal planes where it is less pronounced [101, 102]. Hence, for optimizing electrochemical performance, a high number of edge sites is desirable, which can happen when graphene transitions to a 3D architeture with more layers, while maintaining his "2D" properties [86]. LIG is an appropriate example, since it is very rich in edge plane sites and density of defects. The porosity of LIG leaves many edge plane structures exposed to electroactive species and functionalized nanomaterials, enhancing catalytical activity for

redox reactions. [76, 86].

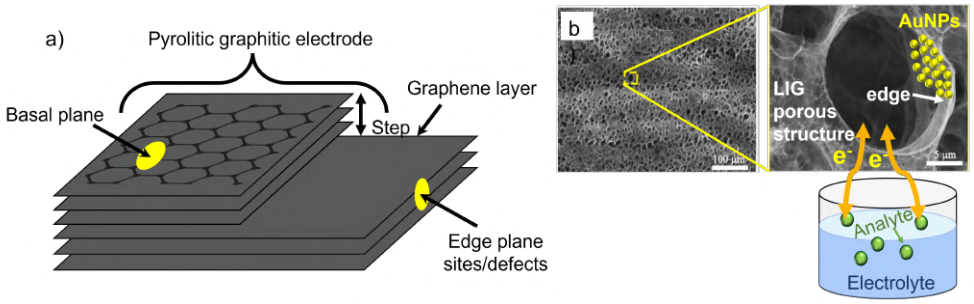


**Figure 2.8:** (**a**) Schematic diagram of pyrolytic graphite showing atomically ordered hexagonal planes, "basal planes", and edge plane like-sites/defects; (**b**) Typical SEM image of LIG, with the yellow rectangle representing a zoomed porous structure, where electrolyte can penetrate and promote HET, and NPs can be deposited. Original SEM images retrieved from [100].

Bare LIG electrode applications exist, however their selectivity is relatively poor, since the presence of electroactive species with similar redox potentials to the analyte may not be discriminated, making these electrodes prone to interferents [11, 103]. To enhance the electrochemical response, functionalization of electrodes started being implemented by chemically modifying its surface with materials that show great affinity with the analyte [103, 104].

Methods for modifying the electrode surface depend of course of the analyte in question and its final application. However, the most used procedures in LIG are functionalization with bioreceptors (antibodies, enzymes, etc), since they present a strong and selective affinity with specific biomolecules, doping of LIG surface with heteroatoms (possible when laser induction occurs in a controlled atmosphere, such as nitrogen) and deposition of electroactive nanomaterials (metal NPs, carbon-based nanomaterials, etc) [103]. Nanomaterials such as Au, Cu, or Pt NPs, CNTs, GO, among others, present a high electrocatalytical activity and enlarged surface-to-volume ratio, which leads to an increase in the current signal [103]. Other properties include significant electric conductivity, good adsorption capability and high chemical stability, which altogether enhance the sensor's sensitivity and lower its LOD [10]. Applying these nanomaterials' properties in LIG is even more advantageous due to its porosity and large surface area, which creates a pathway for the adsorption of these NPs. With the attachement of these metal NPs and its catalytic activity, there is a higher number of catalytic active sites, improving the HET in redox reactions [85, 104].

In nitrite sensing, modification of electrodes with nanomaterials, such as AuNPs, PtNPs or CNTs, has been frequently used to improve the electrocatalytic activity of the redox reaction and also minimize electrode fouling caused by products generated during nitrite oxidation [10]. However, the vast majority of nitrite sensors found in the literature were glassy carbon electrodes or graphene-based electrodes, whereas only one report of a LIG electrochemical sensor functionalized with nanomaterials was found. In this study by Nasraoui et al. [10], a LIG electrode modified with COOH-functionalized MWCNTs and AuNPs was reported to have a linear range of 10-140 uM and a LOD of 0.9 uM, a value comparable and sometimes lower to some other carbon-based electrodes (ranging from 0.1 to 30 uM). It is worth reminding some advantages of LIG regarding other graphene production methods, such as flexibility, simple one-step production with no need for additional preparation, and much lower costs than CVD or screen-printed electrodes, while presenting comparable values of sensitivity.

## 2.5 Hybrid Sensors

Electrochemical sensors have demonstrated their ability to analyse chemical reactions, such as oxidation or reduction. However the data retrieved from these measurements alone is insufficient to provide reliability to the data, as well as it fails to give complete and detailed information on the

investigated species. In recent years, experimental techniques, known as multi-domain or dual-mode, that involve sensing in more than one transduction domain have started to receive attention [105]. Electrochemical techniques have been integrated into hybrid sensors by combining them with optical transducing, which is advantageous, as they can provide counterproof, where information given by the electrochemical sensor and optical sensor of the same analyte can be exchanged to avoid false results (false negative/positive) and gain reliability. Moreover, they can provide additional new information that with only one domain couldn't be known, such as extending the detection range of a certain analyte by combining each sensor's detection range [106].

This type of hybrid transduction started to involve optical fibers due to their known characteristics. For instance, a hybrid sensing system combining simultaneous electrochemical (voltammetric) and optical (absorbance spectroscopy) measurements, with applications in beer discrimination, was reported in [106]. However, the sensing process was done outside the optical fiber, in a sample cell, where the optical fibers only guided the light, and a carbon screen-printed electrode was placed inside the sample cell with the electrolyte. An electrochemical SPR optical fiber sensor for heavy metal detection was developed by Ying et.al [107], where the deposited thin gold film in the optical fiber coating serves as the WE for anodic stripping voltammetry and for high-efficency in SPR sensing of refractive index changes by the heavy metal adsorption on the surface.

Another hybrid configuration was reported by Richter et.al [105], where it was used a Long-Period Fiber Grating functionalized by an ITO film on the surface of the fiber, to study the electrochemical and optical properites of ITO/electrolyte interface. The ITO acts as the WE and also, as a coating, it enhances the sensitivity of the LPG to changes in the external refractive index. This way, electrochemical and optical transmission measurements were monitored simultaneously, providing a reliable data set rich in complementary information from two different domains. The schematic diagram of the experimental apparatus is visible in Figure 2.9.

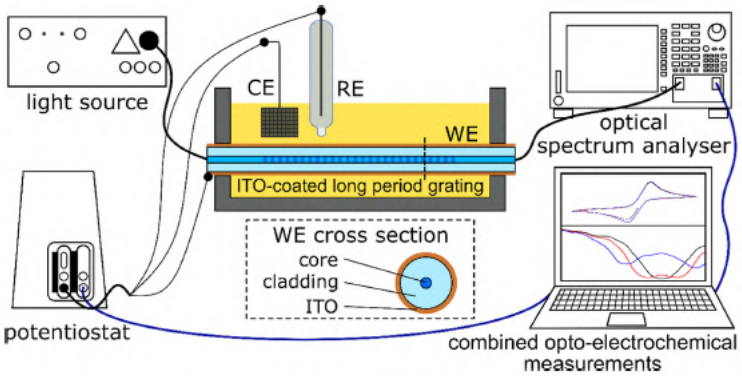


**Figure 2.9:** Hybrid sensor diagram retrieved from [105].

# CHAPTER 3

## Experimental Implementation and Characterization

### 3.1 LIG production on PI-coated Optical Fiber

In order to produce LIG on optical fibers, a continuous $CO_2$ laser with wavelength of 10.6 $\mu$m and maximum power output of 60 W (RedSails Technologies) was used. The laser beam exits through a laser head that can move linearly in a xy plane, so it can pattern any kind of 2D design in the substrate, in this case a silica optical fiber coated with polyimide, of the type SM1500(4.2/125)P.001, acquired from Fibercore. It is a SMF with 4.2 $\mu$m of core diameter, 125 $\mu$m of coating diameter and 30 $\mu$m coating thickness.The scribing movement is controlled by the software RDWorks, where several parameters could be selected, such as the spacing between consecutive lines of laser scribing (d), scanning speed ($v_{laser}$) and laser power (P).

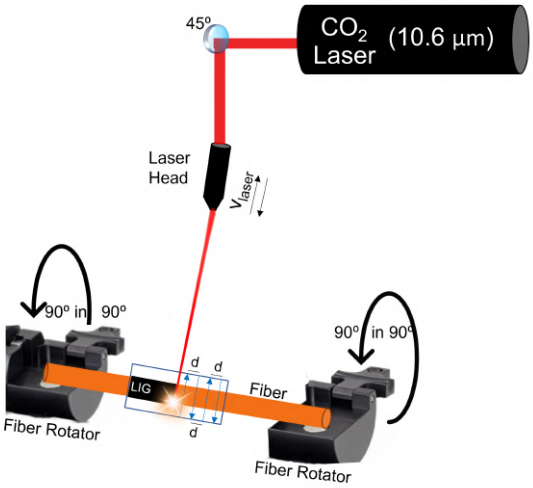


**Figure 3.1:** Scheme of LIG-on-fiber samples production.

In this work, d = 0.08 mm and $v_{laser}$ = 150 mm.s$^{-1}$ were used for all LIG electrodes produced. The laser scanning was done transversely to the optical fiber, after unsuccessfully trying to align the laser beam with the fiber axis, producing LIG with length of 2 cm. Since the PI irradiated in this case isn't a film but rather a coating surrounding the optical fiber, attempts were made to produce LIG all around the fiber. It was placed in a platform that straps and rotates the fiber in its longitudinal axis. This way, two types of electrodes were fabricated, one just scanning the fiber in 1 passage, and the other where the fiber was manually rotated from 90° to 90°, thereby laser scanning the fiber in 4 passages (for simplication purposes, from now on this scanning is called 360° scanning). This process is exemplified in Figure 3.1. Intending to investigate the laser power that optimizes the quality of LIG production, several power values were explored but the main ones investigated were 2.5 W and 4 W, as this last value was reported by a previous work to optimize the LIG coating on fiber. A powermeter (S350C model from Thorlabs) was used to measure the optical power from the laser. Lastly, everytime before starting scanning on a new fiber sample, the distance between the laser head and the fiber was made sure to be equal to the focal length, of 1.8 cm.

## 3.2 SEM and Raman Characterization

The Scanning Electron Microscopy (SEM) is a high-resolution instrument that can provide information on surface topography and morphology, crystalline structure and chemical composition of the material in analysis [108]. It uses an accelerated focused electron beam to scan the specimen's surface and generate 3D magnified images. SEM can also incorporate EDX, a technique that also uses an electron beam but its interaction with the sample's electrons leads to emission of characteristic X-rays [108]. EDX measures the energy transitions that are specific to each chemical element present in the sample, thus providing information about its chemical composition [109].

In order to study the morphology of LIG and which laser parameters produce the most uniform and best quality LIG electrodes, SEM images were acquired using a TESCAN Vega 3SB instrument, in secondary electron mode, at high voltages of 25 keV. EDX spectra were acquired to identify chemical elements and impurities present on LIG optical fibers, as well as to verify if AuNPs were successfully dropcasted and adsorbed by LIG electrodes. LIG optical fiber samples were taped to an aluminium holder using double sided carbon tape and, before measurements, a conductive carbon coating was applied on the sample's surface, in order to avoid charge collection and consequently excessive brightness in SEM images.

Raman spectroscopy is an established characterization technique for carbon allotropes, being important to identify LIG, as graphene has a characteristic signature spectrum [110]. Raman provides information on the vibrational structure (molecular vibrations, or phonon/lattice vibrations for crystals), electronic properties and molecular interactions of the material in analysis. An incident laser beam interacts with the molecules and atoms in the sample, and inelastic scattering of radiation (UV, visible and IR radiation) occurs, shifting up or down the energy of the laser photons. This shift gives information about the vibrational modes in the sample [111].

A Raman spectrum presents different peaks/bands over a large frequency (or wavenumber, $cm^{-1}$) range, that correspond to the energy transitions between vibrational states of molecular bonds [111].

In this work, Raman was used to verify if the PI coating had indeed transformed into LIG, and compare the structural quality of the LIG electrodes processed under different laser powers. Room-temperature Raman spectra were acquired via a Jobin Yvon HR800 instrument (Horiba, Japan), using retro dispersion configuration, with a He-Cd laser (Kimmon Japan) with a wavelength of 442 nm and 1 mW power. The laser beam was focused on the fiber samples with the help of an optical microscope associated with spectrometer (Olympus, 50x objective). A neutral-density filter was used to avoid modification of graphene with light intensity, as it reduces the laser intensity in all wavelengths. The LIG optical fibers were placed, once at a time, in a xy-plane holder. Between spectrum acquisitions, the 360° LIG-on-fiber was rotated manually 180° (turned upside down) so that two different parts of the LIG coating around the fiber could be checked for uniformity and overall good quality. A 600 grooves/mm grating was used to disperse the radiation to the Peltier cooled CCD sensor.

## 3.3 Electrical contacts

Following LIG production in optical fibers, electrical contacts were established in order to create WEs for implementation in the electrochemical cell. For that, a copper wire, a conductive silver ink (Agar Scientific) and Lacomit Varnish (Agar Scientific) were used, as this polymeric resin isolates the electrical contacts and defines the electrochemically active area of the sensor. As represented in Figure 3.2, this process started by fixating the fiber with LIG on a holding platform and placing the copper wire right next to one of the fiber ends, so that when applying the silver ink it glues them together. The ink was left to dry for about 30 minutes and then varnish was applied in the electrical contact formed, as well as in the other end of the LIG, defining a LIG WE with about 0.5 cm of length. It was also left to dry for 30 minutes, followed by a second coat until no silver ink is left exposed.

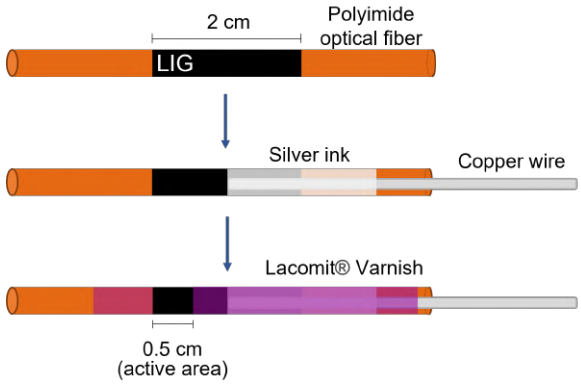


**Figure 3.2:** Scheme of production of the electrical contacts of the working electrode (LIG).

## 3.4 Electrochemical Characterization

To understand if the LIG electrodes are suitable for electrochemical sensing, each electrode was characterized by Ciclic Voltammetry and Electrochemical Impedance Spectroscopy techniques. These measurements were performed using a VersaStat3 potentiostat (Princeton Applied Research), whose function is to control the potential applied to the 3D home-made electrochemical cell illustrated in Figure 3.3, and measure the resulting current.

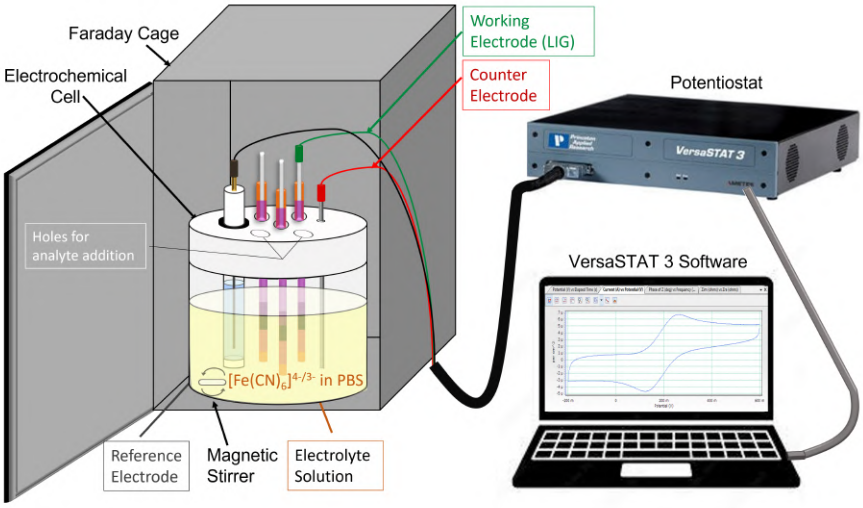


**Figure 3.3:** Schematic diagram of the experimental setup used for both electrochemical characterization of LIG electrodes and nitrite detection.

The cell contained a three-electrode setup, where LIG on fiber was the WE, the RE was the SCE and a platinum wire was the CE. These electrodes were fixated, by applying varnish, on the orifices of the cell lid, so that they could be suspended and dipped 3.5 cm in the electrolyte solution. Up to 3 LIG electrodes could be fixated on the cell and be measured. The electrolyte solution consisted in 5 mM of potassium ferrocyanide ($K_4[Fe(CN)_6]$, from Labkem) as the active redox partners, in a 50 ml of Phosphate Buffer Saline (PBS) solution with constant pH = 7.4. This PBS was prepared by using tablets from Fisher Bioreagents, 1 tablet per 200 ml provides a solution with 0.137 M NaCl, 0.027 M KCl, and 10 mM of phosphate buffer. The redox mass was diluted in the solution with the help of a magnetic stirrer, rotating at 500 rpm for a few minutes, and the solution was transferred into the

electrochemical cell. The cell is placed inside a faraday box (to block external electromagnetic fields), where the electrical connections of the electrodes to the potentiostat were done, as observed in Figure 3.3. Just before measurements are taken, all the electrodes were rinsed with deionized water, and the CE was additionally cleaned with ethanol.

### 3.4.1 Ciclic Voltammetry

CV is a widely used electrochemical technique for the characterization of electrodes and investigation of redox processes of electroactive species [94]. It's possible to obtain information such as the Half-wave Potential ($E_{1/2}$) and the reversibility of the chemical reaction [94, 96]. CV measures the current generated in the WE, as the applied potential is scanned linearly with time between two chosen values (starting potential, $E_1$, and switching potential, $E_2$). However, when voltage reaches $E_2$, the scanning direction is reversed and potential is swept back until reaching $E_1$ [95]. The obtained measurements are displayed as a current vs. voltage plot, known as voltammogram [94]. A typical voltammogram of a reversible redox reaction is portrayed in Figure 3.4, where an arrow near A indicates the beginning and the direction of the scanned potential [96].

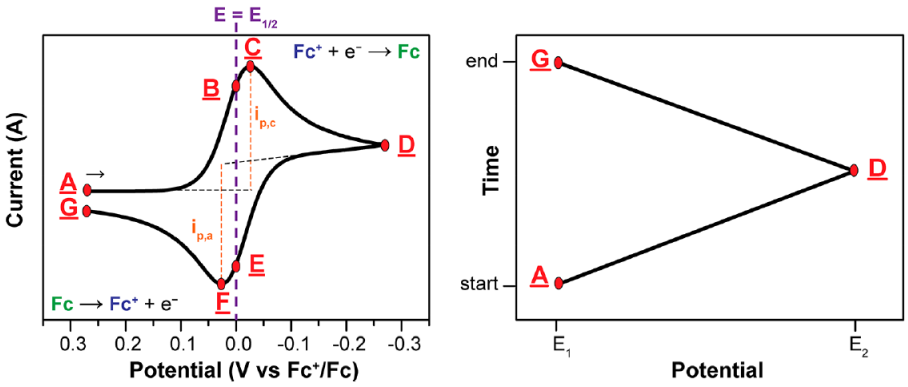


**Figure 3.4:** Typical voltammogram of reversible reduction of 1mM $Fc^+$ solution to Fc, with various points from A-G represented (left), and applied potential as a function of time, with initial (A), switching (D) and end (G) potentials represented (right). Retrieved from [96].

This particular example has the x-axis going from high to low potentials (US convention) while in this work the opposite was used (IUPAC convention) [96]. This "duck" shape is characteristic of quasi-reversible processes and is due to the evolution of the concentration profiles according to the potential sweep and diffusion processes [95], which can be modeled by the Nernst equation in the equilibrium, where R is the universal gas constant, T the temperature, F the Faraday's constant and n the number of electrons [96].

$$E = E^0 + \frac{RT}{nF} \ln \frac{(Ox)}{(Red)} = E^0 + 2.3026 \frac{RT}{F} \log_{10} \frac{[Fc^+]}{[Fc]} \tag{3.1}$$

It predicts how the potential applied E induces changes in the concentrations of the oxidized (Ox) and reduced (Red) analyte, and vice-versa [96]. In this example of reduction of $Fc^+$ to Ferrocene (Fc) with one electron transfer (n=1), the potential is swept negatively from A to D, and when reaching $E^0 \approx E_{1/2}$ (average potential between F and C), reduction becomes thermodynamically favorable, so that $Fc^+$ is more easily reduced to Fc and a cathodic (reduction) current continues to increase [96, 98]. It reaches a peak cathodic value at C, due to additional $Fc^+$ arriving from the bulk electrolyte solution, and then decreases since the volume of solution containing Fc created at the electrode's surface (known as diffusion layer) continues to grow as the scan increases. This slows down the mass transport of $Fc^+$ from the solution to the electrode, as these ions need to travel greater distances to reach the electrode's surface and undergo reduction. This decrease in current response is thus typical of a semi-infinite diffusion regime in a planar electrode, a process which will be later discussed.

The potential is then reversed and scanned in opposite direction, until reaching $E_1$. The same process occurs but instead of reduction, oxidation of Fc back to $Fc^+$ happens and an anodic current is produced [96, 98].

In this work, CV technique was implemented to understand the adequacy of the LIG electrodes produced towards electrochemical sensing, specifically regarding reversibility of the redox reactions and other processes behind these measurements. First, a blank CV was performed, that is, a solution containing only PBS and no electroactive species, in order to observe the potential values that define the ideal potential window of chemical stability. After that, more blank CVs ("stabilization CVs") measurements were made, this time in the defined potential window. This is done to minimize faradaic currents originated from the redox activity of functional groups present in LIG's surface, which is stabilized after a few CV cicles. Lastly, nine CV measurements were recorded with the electrolyte solution of $K_4[Fe(CN)_6]$, each with their own scan rate ($v_{rate}$),in order to monitor its influence in current response and overall shape of the voltammogram. This way it is possible to check the degree of reversibility of the redox process. CV's were performed on 2.5 and 4 W lasing power LIGs, and 4 W LIG with AuNPs. All measurements were acquired with the software VersaStudio.

### 3.4.2 Electrochemical Impedance Spetroscopy

EIS is a useful technique since it analyses the bulk and interface properties of electrochemical systems. As previously explained in section 2.4, it consists of applying a small sinusoidal voltage signal to the electrochemical cell and measure the resulting current. The current is acquired while sweeping a wide range of perturbation frequencies, f, of the applied potential [90, 94]. The response can be read in terms of impedance, Z, a complex impedance, with real ($Z_{Re}$) and imaginary ($Z_{Im}$) components, which can be graphically represented by a Nyquist Plot. The capacitive reactance ($Z_{Im}$) is plotted against the resistance ($Z_{Re}$), for different values of angular frequency, w. At the x-axis, impedance at the right side of the plot is conducted with low frequency, while, at higher frequencies, their generated impedances are shown on the left [95]. A typical example can be found in Figure 3.5.

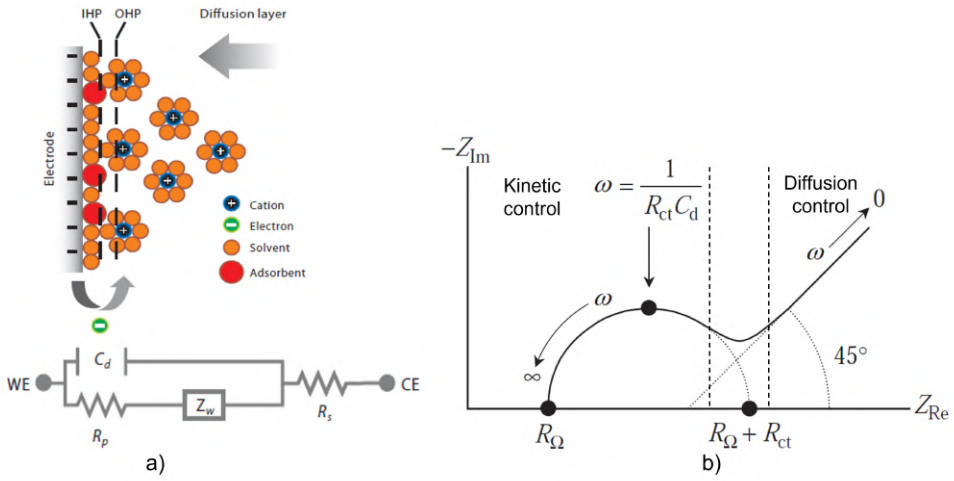


**Figure 3.5: a)** Negatively charged electrode, where countercations are aligned along its surface. The electrochemical processes here are modeled by the Randles equivalent circuit, at bottom left. **b)** Typical Nyquist plot a planar electrode. Abbreviations: $C_d$, double-layer capacitor; ; IHP, inner Helmholtz plane; OHP, outer Helmholtz plane; $R_p/R_{ct}$, polarization (charge-transfer) resistance; $R_s/R_\Omega$, series resistance [95, 112].

A key part in EIS consists in designing an equivalent electrical circuit where its electrical components, such as resistances, capacitors and constant phase elements, intend to model the different physical and chemical characteristics of the eletrolyte/interface system, such as charge transfer, mass

transport and diffusion processes [113]. Therefore, based on the Nyquist plot, a theoretical model for equivalent circuit is constructed, where the Randles equivalent circuit, shown on Figure 3.5, is the most applied. The circle shape is associated with the redox charge transfer processes and the linear region with mass transport in bulk electrolyte solution [95]. Series Resistance ($R_s$) represents the ohmic contributions of the electrical contacts and of electrolyte solution (ionic conductor) that limits the current signal. Regarding the electrode interface, parallel elements are introduced since the total current flowing through the $R_s$ interface is the sum of contributions from the faradaic process, and the double layer charging process (non-faradaic) [90]. The faradaic impedance is generally composed of a pure resistance, the Charge-Transfer Resistance ($R_{ct}$) and a general impedance, the Warsburg impedance ($Z_w$), that represents a resistance to the diffusion of electroactive species to the WE interface (mass transport) [90]. $R_{ct}$ quantifies the kinetics of the redox process, where a large $R_{ct}$ value means that the chemical system is kinetically sluggish. In non-faradaic processes, some of the ions are adsorbed or desorped in the interface, in order to adjust the ionic atmosphere until the charge balance between the electrode and interface is reached, creating an electric double layer.

This is ideally equivalent to a electric charge of a capacitor with capacitance $C_d$ [90, 95]. Experimentally though, a non-ideal capacitive behaviour is observed, due to surface roughness effects, and $C_d$ is replaced by a constant phase element (CPE or Q), a mathematical construction that adjust its values according to $Z_{CPE} = \frac{1}{Q_0(jw)^n}$, for which $Q_0$ is a pre-exponent factor analogous to a capacitance and n is a constant moduling the element's phase, that ranges from 0 to 1 [95]. Going back to the Nyquist plot, several information regarding the equivalent circuit can be extracted from this impedance diagram. $R_s$ corresponds to the high-frequency point that intercepts the x-axis. $R_{ct}$ value is equal to the diameter of the circle and $C_d$ can be extracted from the frequency at the maximum of the circle, $w=1/(R_{ct}C_d)$. Ideally, a $R_s$ as close as possible to zero and a low $R_{ct}$ value is desirable [95].

EIS was used in this work to observe the interface properties related to the electron processes between nitrite and the WE interface. EIS characterization was performed on 4 W LIGs, with and without AuNPs, since it's also pertinent to study the catalytic impact of AuNPs in the kinetics of the redox reaction.

## 3.5 Nitrite Detection

Several electrochemical meaurements were performed for different nitrite concentrations, with DPV technique. The same setup illustrated in Figure 3.3 was used for nitrite detection, however the electrolyte solution was different. Alongside with 400 ml of main solution of PBS of 7.5 pH, a solution consisting of 1mM stock concentration of nitrite in 200 ml of PBS was used to make six dillutions of 50 ml. The nitrite concentrations and corresponding volumes used in each dillution are presented in Table 3.1, where for example, for 20 $\mu$M of nitrite, 1 ml of nitrite-containing PBS and 49 ml of pure PBS compose the total volume of electrolyte solution.

For each fiber, first a stabilization CV in PBS was performed. Then, two types of DPV with different specific parameters, DPV#1 and DPV#2, were performed in blank, and for each nitrite concentration of Table 3.1, in ascending order, to know which one provided better results in detecting the nitrite signal.

**Table 3.1:** CV and DPV parameters used for nitrite detection measurements, along with each nitrite concentration solution.

| | Stabilization CV | DPV#1 | DPV#2 |
|---|---|---|---|
| **Initial; Final Potential (V)** | 0 | 0.1; 0.9 | 0.1; 0.9 |
| **Window Potential** | -1 - 0.9 | - | - |
| **Cicles** | 10 | - | - |
| **Scanning Speed** (V/s) | 0.05 | - | - |
| **Pulse: height (mV); width (s)** | - | 45; 0.03 | 30; 0.15 |
| **Step: height (mV); width (s)** | - | 2; 0.2 | 3.5; 0.35 |
| **Measurements** | PBS | PBS and Tank water | |
| **Nitrite concentration (uM)** | - | 10 20 40 50 100 200 | |
| **Nitrite solution Volume (ml)** | - | 0.5 1 2 2.5 5 10 | |

In Differential Pulsed Voltammetry, the potential is scanned in one direction with a base potential and short pulses applied over time, employing a linear staircase-shaped signal, as demonstrated in Figure 3.6. The current is sampled immediately before the potential pulse and at the very end of this interlevel potential, before returning to a different base potential. The net current is the difference between these two values, which is plotted as a function of the base potential [95, 98].

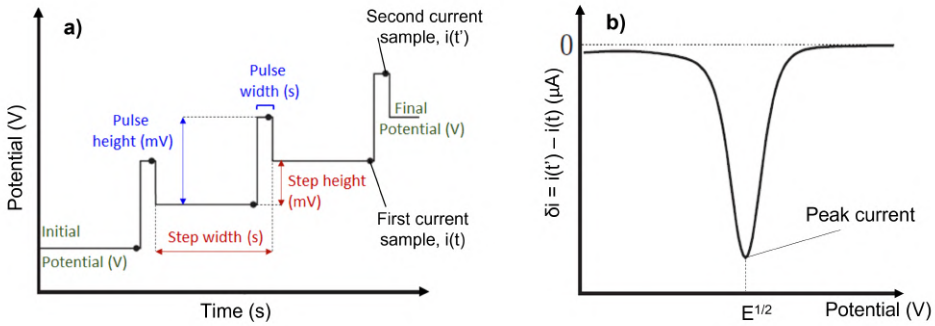


**Figure 3.6: a)** - Staircase-shaped pulsed signal of potential applied over time, characteristic of DPV, showing its parameters; **b)** - Current response $\delta$i corresponding to the difference between the two sampled current values, where the peak current is proportional to analyte concentration. Modified from [95].

This is a major advantage compared to other simpler voltammetric techniques, since it minimizes capacitive currents and and promotes the extraction of faradaic currents. As previously explained, the capacitive current originates from the double electric layer which acts as a capacitor that is accumulating charges. This charging process has a very small time constant and therefore, the capacitive current only appears at the very beginning of applying the pulse, increasing significantly the proportion of redox current at the end of the pulse, as faradaic processes have a higher time constant [95,98]. Thus, it shows a better sensitivity towards redox reactions in the electrode, where the peak redox current (situated around $E_{1/2}$, of the electroactive species) is proportional to the analyte concentration [98].

Always before initiating DPV in a new concentration solution, the fibers were rinsed with deionized water and the solution was mixed with a magnetic stirrer at 500 rpm during 2 minutes. Measurements were taken for LIGs of 2.5 and 4 W, LIGs of 360° and 1 passage, all with AuNPs. Additionally, after choosing the optimal LIG and DPV parameters, nitrite detection measurements were performed for three different pHs of PBS solution in order to verify its influence on the electrochemical measurements and to produce calibration plots. PBS solutions were produced with 6.6, 7.5 (standard PBS) and 8

pH values, with 600 ml of volume. PBS of 6.6 and 8 pH were prepared by keeping constant the phosphate buffer concentration in 10 mM and the ionic strength as well (0.137 M NaCl and 0.027 M KCl), but varying the $NaH_2PO_4$:$NaHPO_4$ ratio [114]. For PBS of 6.6 pH, a ratio of 6:4 was used, while for a PBS of 8 pH, a ratio of 9.4:0.6 was used. pH measurements were performed with a commercial pH meter (from Hannah Instruments). After calibration, the sensor was ready to be tested in real water samples, replacing PBS with aquaculture fish water as the electrolyte solution. One of the samples is from seawater that enters the RAS system (inlet sample), and the other is from the aquaculture tanks (outlet sample), whose chemical analysis was shared, but due to confidentiality reasons its information can't be reported in this work. Nonetheless, the adequacy of the LIG sensor in real samples was evaluated, as well as its capability in detecting nitrite values deemed toxic for fish in the required linear range.

Note that AuNPs deposition on the electrochemical active area of LIG was done by dropcasting technique, as seen in Figure 3.7, which consisted on dropping 100 $\mu$L of AuNPs solution with a micropipette and let it evaporate over time in a chemical fume hood; this process was repeated twice. An alternative method of immersing the LIG fibers (dip-coating) in the AuNPs solution for a period of time was first tried but proved to be unsuccessful, as will be seen in section 4.1.1.

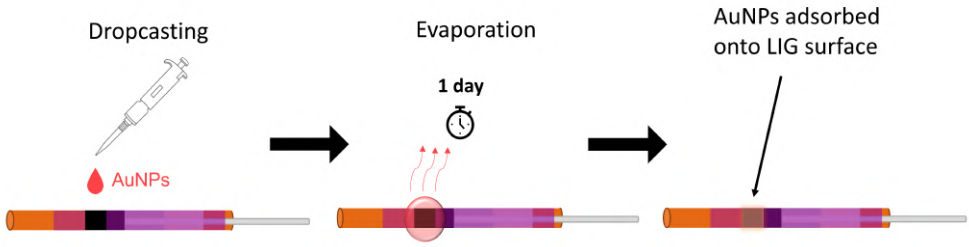


**Figure 3.7:** Dropcasting technique of AuNPs onto the LIG electrode.

## 3.6 Hybrid Platform

After producing the LIG electrochemical sensor for nitrites detection, another main goal of this work was to integrate it in a hybrid sensing platform with an optical pH sensor.

Although nitrites are a key parameter that impact well-being of fish, other parameters such as pH, are important as well since small variations result in sub-optimal conditions for fish and could influence nitrite toxicity. Specifically, pH has been reported in [10] to have influence in the electro-oxidation of nitrite for slightly acidic solutions, where electro-oxidation increases in this case, whereas for pH $> 6$ it becomes more difficult and stable. This way, it is important to check the influence of pH on the response of this work's LIG nitrites sensor, in order to calibrate it correctly, as well as to check possible influence of nitrite oxidation on the pH values measured with the optical pH sensor.

The optical pH sensor was developed by a laboratory colleague. In his work two different optical pH sensors were produced: a tapered SMF with a FBG and a D-shaped POF. The tapers, provided by Liaocheng University, were produced using a combiner manufacturing system, which through a three-electrode configuration, a plasma field surrounding the fiber is created with even heat distribution. This field is applied to a short section of the fiber while both fiber ends are pulled, to produce the tapered fiber. Afterwards, a FBG is inscribed in the tapers using a UV laser with the phase mask method. The D-shaped POF was produced by placing the POF in a customized V-groove with a depth of approximately 700 $\mu$m, leaving 300 $\mu$m of the fiber exposed to be polished away by a polishing machine. By changing the geometries of the fibers, the light traveling inside the core starts to leak to the surrounding medium as an evanescent wave. However, there is still the need to coat the fiber with a pH sensitive material. The material chosen was polyaniline, produced directly on the fibers surface using synthetic oxidative polymerization. The most common form of polyaniline is

its partially oxidated state, emeraldine. It changes between its swollen and protonated configuration when in contact with an acidic medium, revealing a green color (emeraldine salt), or between its deswollen and deprotonated configuration when in contact with a basic medium, revealing a blue color (emeraldine base).

When pH characterizing these sensors, it is possible to see a trend regarding power variations. This is because when pH rises, polyaniline transitions from protonated to deprotonated, which raises the layer's refractive index and results in a decrease in transmission.

The initial configuration consisted in integrating the LIG WE and the tapered optical pH sensor in the same fiber, by splicing them together using a fusion machine (Fujikura, model FSM-40s), with this fiber being inserted in the electrochemical cell. The pH sensor was located near the bottom of the graduated cell, in order to ease the calibration step where hydrochloric acid (HCl) is needed. The fiber would connect to the optical interrogator (Micron Optics, model SM125-500, acquisition frequency of 1 Hz and spectral range of 1520-1570 nm), an instrument that can measure multiple optical FBG sensor signals.

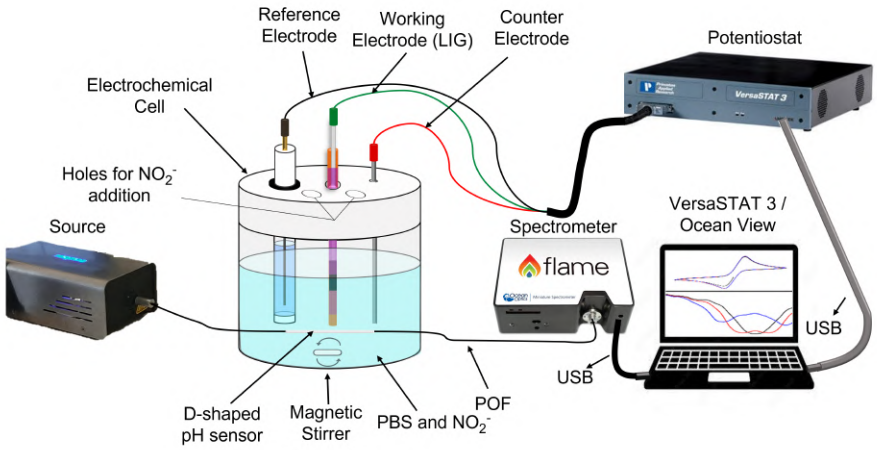


**Figure 3.8:** Hybrid sensing platform containing the LIG nitrite sensor in the usual electrochemical cell and the POF pH sensor placed in the bottom of the cell.

Unfortunately, the interrogation system suffered a malfunction and an alternative setup had to be designed, using the POF D-shaped optical pH sensor. This was not a issue in terms of performance, since both pH sensors have similar sensing principles and behaviours, however integrating and splicing the LIG and pH sensor in the same fiber line was no longer possible because of the over-sized dimensions of POF compared to the SMF polyimide fiber where LIG is. Therefore, the setup used for electrochemical measurements was maintained, and two small holes, on opposite sides, were made at the bottom of the electrochemical cell, in order to place the D-shape centered at the bottom,as shown in Figure 3.8. Glue was used at the holes to hold the D-shape and avoid electrolyte leakage. The LIG WE was placed close to the D-shape to check possible influences on one another, and a hybrid platform was thus created. Unlike in previous protocols such as of section 3.5, here only 30 ml of PBS were filled in the cell and measurements were performed only for PBS, and for the same PBS solution with $\sim$ 50 $\mu$M of nitrites added. This difference in procedure is due to the pH sensor needing to be in the same position without moving or receiving external touches for measurements in HCl (used for baseline), blank and nitrites concentration, otherwise output intensity would have different values. The light source used for pH sensor was a 7 W tungsten lamp (model LS-W7, brand Sarspec) with an emission range between 380 nm to 2500 nm, and a spectrometer (model FLAME-T-UV-vis by Ocean Optics, USA), with a detection range of 180 nm to 890 nm, where transmission spectra were acquired using the Ocean View software.

# CHAPTER 4

# Results and Discussion

## 4.1 Morphologic Characterization

### 4.1.1 SEM

In order to assess the morphology of LIG samples and the laser parameters that provide a high quality production of LIG onto the polyimide fiber, SEM images of these electrodes were taken. Initally, two scanning laser speeds, of 150 mm.s$^{-1}$ and 200 mm.s$^{-1}$, were tested in LIG production, however only the 150 mm.s$^{-1}$ speed provided consistently better results based on initial SEM images, and this value was chosen for every electrode production henceforth. Likewise, the direction of laser scanning initially was tried transversely to the optical fiber or aligned with its longitudinal axis, which was assumed to be the optimal way to provide consistency to the LIG layer. However, the alignment of the focused laser beam with the 125 $\mu$m optical fiber proved to be hard and unsucessful, confirmed by some SEM images where LIG wasn't uniform along the fiber. From then on, the laser beam was always scanned transversely, and other parameters were studied.

In Figure 4.1, for instance, the SEM images refer to LIG produced with 360° laser scanning on polyimide fibers, at two different laser powers, 2.5 W and 4 W. Analysing the SEM image of 4.1 **a)** of LIG at 2.5 W, it is possible to observe two different morphologies. Pinpointed in yellow, some areas appear to show a slightly porous structure with graphene multi-layers, characteristic of LIG. However, this transformation of PI into LIG is not uniform, as some areas pinpointed in red that appear in between them don't present the microstructure of LIG, indicating that the polyimide there likely hasn't been fully processed. Thus, 2.5 W lasing power seems to be close to the threshold lasing power to produce LIG, which is in accordance to the theory described in section 2.3.1, explaining its heterogeneous surface. In contrast, in Figure 4.1 **b)** of LIG at 4 W, overall the fiber seems to have a more homogeneous LIG layer. It shows some variations in its microstructure, however all polyimide seems to have been transformed into LIG. This is corroborated by Figure 4.1 **c)**, where a cross-section SEM image of the same 4 W LIG shows that all polyimide coating until the cladding interface has been transformed into LIG all around the fiber, as it presents a wavy porous structure. The LIG layer being in contact with the cladding interface is also an important step in order to study possible photonic interactions of light transmitted in the fiber with the exterior LIG coating.

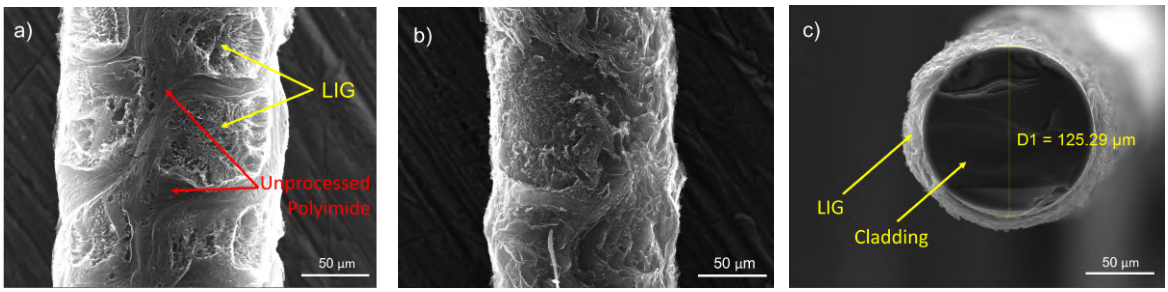


**Figure 4.1:** SEM images with 1kx magnification, of LIG on optical fiber produced in 360°, at **a)** 2.5 W, **b)** 4 W and **c)** 4 W in cross-section, where D1 refers to the cladding diameter.

In Figure 4.2, SEM images of LIG produced on optical fiber with 4 W and 1 passage are shown.

Similar to 4 W 360° LIG, most of the area irradiated by the laser appears to have been converted to a 3D LIG structure. Since the fiber wasn't rotated and was only laser scanned once, there are regions where PI wasn't irradiated, as visible in the left side of 4.2 **a)**. In the intermediate area, a different microstructure from LIG is present, which can possibly be attributed to non-homogeneous laser fluence and heating, given the cylindrical shape of the fiber. A laminated and highly porous microstructure can be further observed on 4.2 **b)**, where the small circular-shaped pores usually found in LIG are missing, however here also exists large volume pores where an electrolyte solution can penetrate and transfer electrons with the electrode's surface. This way, from 2.5 to 4 W the porosity of LIG increased significantly, which is in accordance to the theory written in section 2.3.1, where porosity is reported to increase with the laser fluence.

Furthermore, these laminated porous shapes also offer a decent amount of edge sites, which are known to be important regarding electrochemical activity [76].

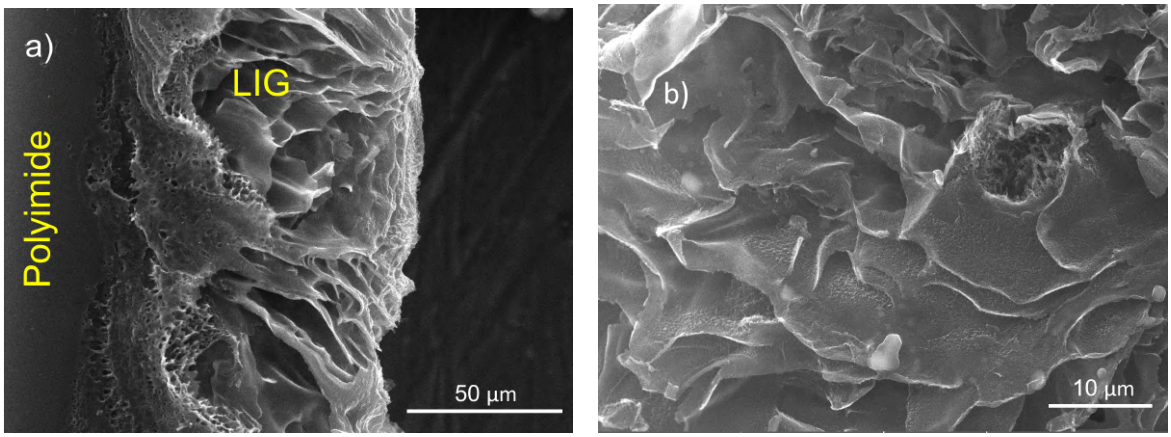


**Figure 4.2:** SEM images of LIG on optical fiber produced at 1 passage and 4 W, with **a)** 1.5 kx magnification and **b)** 5 kx magnification.

SEM imaging was also used, along with EDX spectra, to detect if AuNPs were successfully deposited and adsorbed by the LIG's surface, either with dip-coating or dropcasting technique. In Figure 4.3 b), an EDX spectrum of the area outlined in green in 4.3 a) is presented. It refers to a LIG electrode with AuNPs deposited by dip-coating technique. The EDX spectra presents characteristic peaks specific to each chemical elements, which is the case here to C, O, Na, Al, Si, Cl and K elements. Carbon can be attributed either to LIG or the PI itself, or even the carbon coating used in sample preparation for SEM analysis. Oxygen appears in the oxygen-containing functional groups connected to LIG's surface, while sodium, chlorine and potassium are part of the chemical constitution of PBS, as this sample was examined after electrochemical measurements. This shows that the electrolyte solution is able to penetrate LIG's porous structure and be adsorbed. Aluminium traces appear since the sample holder in SEM is aluminium, and silicon appears due to silica of the fiber optic cladding.

However, Au's presence was not found, as its strong identifiable peak at around 2.2 keV isn't evident. Multiple other LIG-on-fiber samples dip-coated with AuNPs were examined with SEM and EDX and their spectra also don't present a characteristic Au peak, and that AuNPs weren't adsorbed by the LIG's surface, affecting electrochemical sensitivity. One possible reason consists in the hydrophobicity of LIG surfaces, due to limited presence of OH surface groups, which severly affects wettability, thus preventing AuNPs deposition.

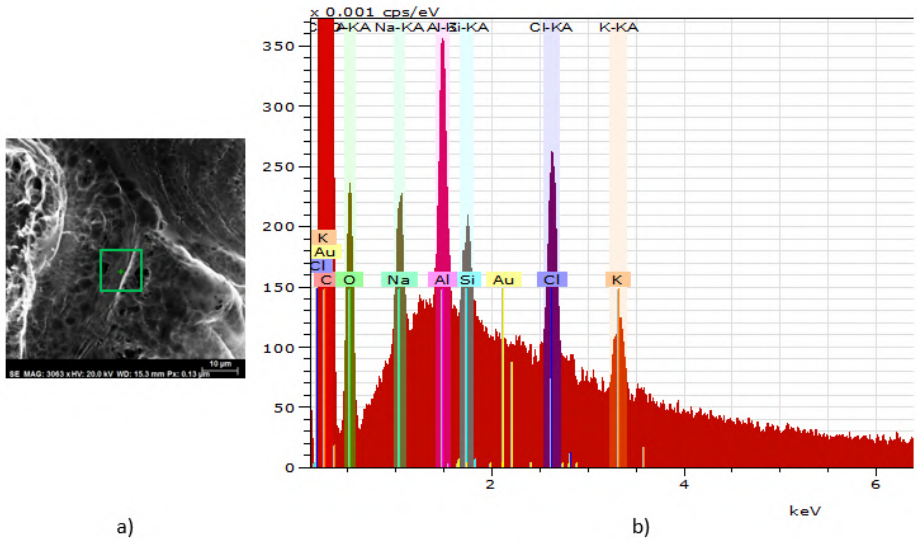


**Figure 4.3:** EDX spectrum in **b)** of the LIG area outlined by green square in **a)**. EDX spectrum shows the peaks's intensities, in counts, as a function of x-ray characteristic energy transitions, in keV, which are named on top of the spectrum as KA or LA.

An alternative deposition method for the AuNPs to adhere to the LIG's porous surface was consequently tried - dropcasting. Various LIG electrodes were examined in SEM and EDX characterization, and AuNPs were found in all of them. For instance, in Figure 4.4 b) an EDX spectrum of the outlined area in the SEM image of a) shows a clear identifiable Au peak, at around 2.1 keV, in comparison to the previous spectrum. The Au atomic percentage was measured in several points along the outlined area and the mean value was 0.35 at.%, showing that dropcasting technique was more effective than dip-coating technique. In the bottom image of a), a spatial distribution of the deposited AuNPs in the same SEM image is shown in orange, visually confirming their presence.

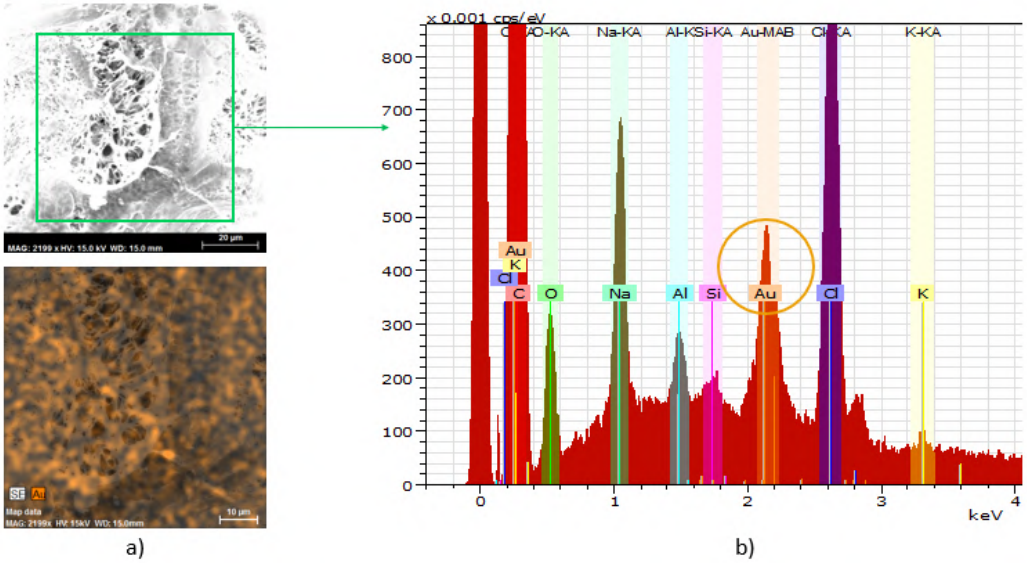


**Figure 4.4:** EDX spectrum in **b)** of the LIG area outlined by green square in **a)**, with an evident Au peak, Au-MAB, outlined by an orange circle. In the bottom image of **a)** a spatial distribution of these deposited AuNPs in the SEM image is shown in orange.

### 4.1.2 Raman

Raman was used to compare the structural quality of the LIG electrodes processed under 2.5 and 4 W lasing powers, and representative results are shown in Figure 4.5. The Raman spectrum of LIG is dominated by the D, G and 2D bands, along some other smaller bands, D' and 2D', as well as combined overtones of peaks, D+D' and D+D" [75, 76]. The peak G at $\sim$ 1580 cm$^{-1}$ corresponds to phonon scattering of the stretching mode of the sp$^2$ carbon bonds ($E_{2g}$vibrational mode), indicating graphitization [76, 115]. The 2D peak at $\sim$ 2740 cm$^{-1}$ refers to the scattering of two Brillouin zone-boundary phonons, with symmetric mommenta, of the breathing modes of perfect aromatic rings [76]. For single-layer graphene (SLG), the 2D peak is very sharp, symmetric and has increased intensity, compared to bilayer or few-layer graphene, where the peak will broaden and shift in position as well [59, 110]. The ratio between the 2D and G bands, $I_{2D}/I_G$, allows to qualitatively infer on the number of graphene layers present in LIG [76]. $I_{2D}/I_G \approx 2$ is a usual feature for SLG, for instance [104], whereas in LIG that ratio is about 0.3 to 0.4 and the 2D band is significantly broadened, as observed in the results, indicating the presence of multilayer graphene. In non perfect graphene lattices, such as LIG, another peak appears. The D band at $\sim$ 1370 cm$^{-1}$ arises from one-phonon scattering involving the breathing mode of aromatic rings, requiring defective or bent sp$^2$ carbon bonds for its activation [76, 116]. The D peak's presence therefore indicates a significant concentration of defects in the graphene structure, and will increase with the number of graphene layers [117]. Along with the D- and G-band full width at half-maximum (fwhm), the $I_D/I_G$ ratio can be used to study structural aspects of the multilayer graphene. The $I_D/I_G$ ratio scales with disorder for sp$^2$ phases obeying the Tuinstra-Konig relation, valid for sp$^2$ carbon phases presenting well defined and intense G bands at $\sim$ 1580-1590 cm$^{-1}$, which states that this ratio is proportional to the inverse of the mean size of ordered domains, thus constituting a measure of crystallinity degree [115, 118]. Clearly, both the D and G bands fwhm and the $I_D/I_G$ ratio are larger for LIG produced at 2.5 W (57 cm$^{-1}$ and 55 cm$^{-1}$ for the D and G band fwhm, respectively, and an $I_D/I_G$ ratio of 0.89) compared to LIG produced at 4 W (52 cm$^{-1}$ and 36 cm$^{-1}$ for the D and G band fwhm, respectively, and an $I_D/I_G$ ratio of 0.27) clearly indicating that the latter presents lower defect density and higher crystallinity degree. Moreover, the band a-C at $\sim$ 1450-1500 cm$^{-1}$, related to the presence of amorphized carbon phases, is much more intense for LIG produced at 2.5 W. This analysis corroborates the SEM analysis suggesting that 2.5 W laser power is indeed near the threshold for LIG formation, since at laser powers below the threshold amorphized carbon phases are produced instead of LIG.

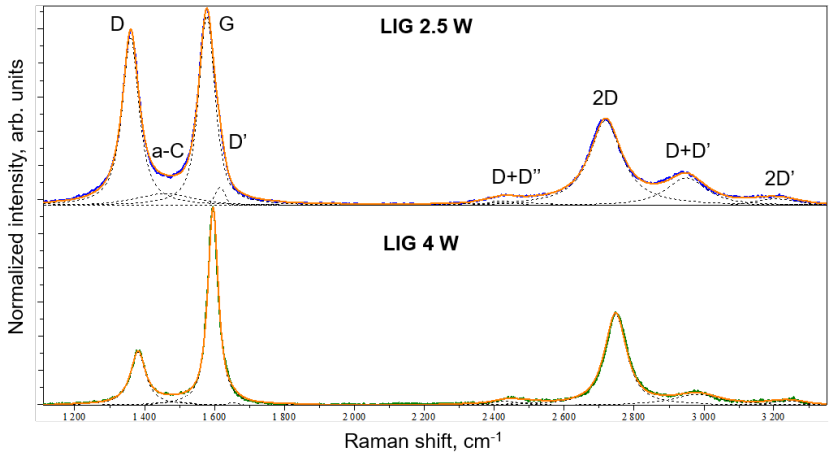


**Figure 4.5:** Raman spectra of 2.5 W and 4 W LIG-on-fiber electrodes, with the LIG characteristic peaks identified. A Gaussian-Lorentzian fitting was applied for both spectra, as represented by the dashed lines. An extra dashed line appears in 2.5 W, referring to the a-C peak of amorphized carbon.

## 4.2 Electrochemical Characterization

### 4.2.1 CV

Regarding the electrochemical characterization of LIG electrodes, nine CVs were performed to study nine different scan rates, by scanning the potential from -0.2 to 0.6 V, using 5mM of $K_4[Fe(CN)_6]$ dissolved in 50 ml of PBS as the electrolyte solution. The redox mediator $[Fe(CN)_6]^{4-}$ is commonly used in electrochemical characterization of electrodes due to its inherent reversibility and simplicity in the chemical reaction. It reacts at the electrode the following way [119]:

$$[Fe(Cn)_6]^{4-} \rightleftharpoons [Fe(Cn)_6]^{3-} + e^- \tag{4.1}$$

As demonstrated in Figure 4.6 a), which shows CVs performed with a scan rate of 50 mV/s of three LIG-on-fiber electrodes (2.5 W lasing power, 4 W and 4 W functionalized with AuNPs), the oxidation reaction yields a positive current response, located in the top part of the CV, where the LIG electrode receives electrons and acts as the anode. In contrast, the reduction reaction yields a negative current response, located in the bottom part of the CV, where LIG acts as the cathode. Note that the 4 W LIG unfortunately suffered damage during measurements, probably by touching the walls or bottom of the electrochemical cell, leaving $\sim$ 0.2 cm of length instead of the original 0.5 cm. This leads to a decrease in current response, lower than that of 2.5 W. Whereas 4 W LIG with AuNPs has the highest current values, due to the presence of highly conductive AuNPs, with enhanced electrochemical activity.

Scan rate is an important parameter because it controls the speed which the applied potential is scanned. Faster scan rates provide less time for reactions to take place in the electrode's surface and decrease the diffusion layer thickness, which in turn increases the mass transport of ions and the current signal [96, 98]. This is confirmed in Figure 4.6 b) where, in nine CVs performed for LIG electrode of 4 W with AuNPs, the current response increases with increasing scan rates.

Specifically, for reversible electron transfer processes limited by a semi-infinite diffusion regime (diffusion which is only bounded by a large planar electrode on one side), the peak current $i_p$ (A) is linearly proportional with the square root of the scan rate $\nu$ ($V.s^{-1}$), according to the Randles-Sevcik equation [96]:

$$i_p = 0.446nFAC^0 \left(\frac{nF\nu D_o}{RT}\right)^{1/2} \tag{4.2}$$

Where A ($cm^2$) is the electroactive area of the electrode, $D_o$ ($cm^2\ s^{-1}$) is the diffusion coefficient of the oxidized analyte and $C^0$ (mol $cm^{-3}$) is the bulk concentration of the analyte. This plot is exemplified in the inset graph of Figure 4.6 b) for all three types of LIG electrodes, where anodic and cathodic peak currents show a linear dependence with scan rate, with all fittings having coefficient determinations $R^2$ above 0.999, except cathodic current linear fitting of 4 W with AuNPs, which has $R^2 = 0.987$. Note that the two lowest scan rate values (5 and 10 mV/s) weren't included in the fittings, as they appear to deviate from linearity. Despite being in accordance with the Randles-Sevcik equation for reversible processes, 4 W LIG electrodes present different peak current slopes ($m_{anodic}$=0.48 and $m_{cathodic}$=-0.21 for 4 W AuNPs), pointing to some degree of irreversibility of the reaction [95, 96], which is unexpected. Whereas 2.5 W LIG has very similar slopes, characteristic of a reversible reaction with almost identical behaviours for oxidation and reduction.

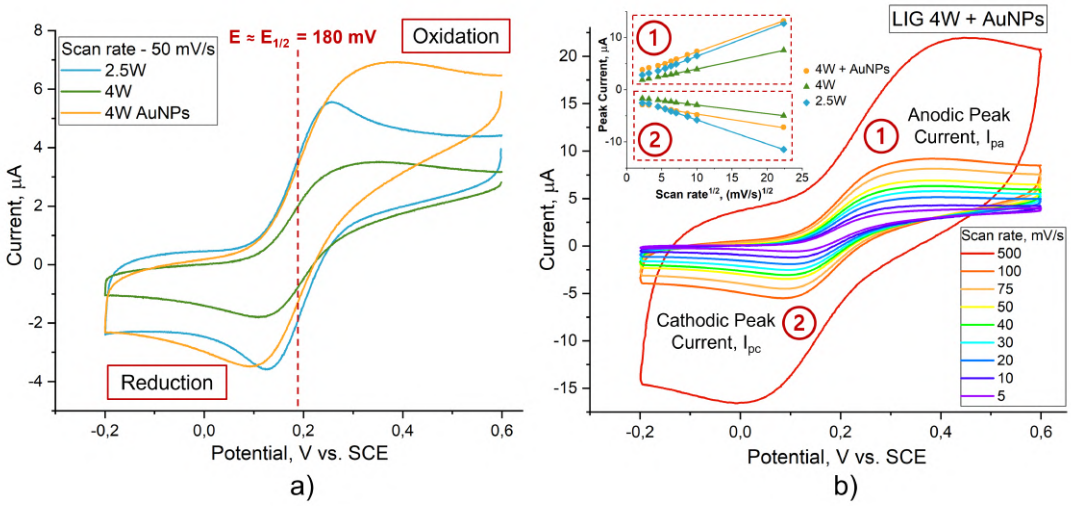


**Figure 4.6: a)** CVs performed with scan rate of 50 mV/s, of 2.5 W, 4 W and 4 W LIG with AuNPs. **b)** Scan rate study, from 5 to 500 mV/s, of 4 W LIG/AuNPs. The inset graph shows both the peak anodic and cathodic current of the three tpes of LIG electrodes, plotted against the (scan rate)$^{1/2}$, with linear fittings applied.

In fact, this can be observed in Figure 4.6a), where 2.5 W LIG and 4 W LIG exhibit different peak shapes. 2.5 W LIG presents visible and similar anodic and cathodic peaks, with a clear decrease in current response after the peaks. This is characteristic of a reversible process limited by the semi-infinite diffusion regime. However, for both 4 W LIGs, the current peaks appear wider and with a less steep decrease in current after the peaks. These wide peak shapes lead to an increase in peak-to-peak separation $\Delta E_p = E_{p_{anodic}} - E_{p_{cathodic}}$, from 2.5 W→4 W→4 W + AuNPs, which is contrary to reported in the literature, where AuNPs increase reaction kinetics for the $[Fe(CN)_6]^{4-}$ redox pair [10].

Clearly, a competing mechanism to the standard semi-infinite diffusion regime seems to take part in 4 W LIGs that is causing these wide peak shapes. This difference in electrochemical processes is likely due to the effect of lasing power on creating different morphologies of LIG, as demonstrated in section 4.1.1, since every other parameters and conditions were the same for 2.5 W and 4 W LIG electrodes. In 2.5 W only some small pores start to appear, presenting regions where PI isn't even fully transformed into LIG, whereas in 4 W all PI seems to be converted and LIG exhibits a wider porous and laminated structure. This can influence the diffusion of electroactive species, since the electrode's surface starts to shift from planar to a complex porous structure, meaning that the semi-infinite diffusion regime no longer is entirely valid. Instead, a porous diffusion is thought to be the dominant process, where the electrolyte solution penetrates the pores and electron transfer occurs beyond the electrode surface. The small volume of the pores limits the access to the active interface, increasing the resistance to diffusion of ions.

The complexity and different types of pores (micropores, mesopores, etc) possibly lead to slightly different potentials that induce the redox reactions, which can explain the widening of the peak current shape in 4 W LIGs, compared to the narrower shape of 2.5 W.

It can also explain the deviation in linearity of the lower scan rates regarding peak currents. In porous structures, access to active interfaces is limited and diffusion of ions to the inner pore walls becomes slower [114]. If the potential is scanned too quickly, electron transfer reactions in the pores won't happen. However, in some lower rates the ions will have enough time to diffuse and react in the pores, and at a higher pore depth. When this situation occurs, peak current seems to stop depending linearly with the root square of scan rate, which could indicate a porous diffusion regime instead of the standard semi-infinite diffusion. To further corroborate the existence of this porosity diffusion-ruled regime in LIG, EIS was also used.

### 4.2.2 EIS

EIS was performed to describe the bulk and interface mechanisms of the porous LIG. Here a sinusoidal 5mV perturbation at the open circuit potential (dc bias voltage of 90 mV vs. SCE), within the 1 kHz to 0.1 Hz range, was employed, using 5 mM of $K_4[Fe(CN)_6]$ dissolved in 50 ml of PBS as the electrolyte solution.

These EIS spectra of 4 W LIG with and without AuNPs are represented by a Nyquist plot in Figure 4.7 **a)**. Both plots describe a curve that corresponds to the beginning of the semi-circle shape characteristic of electron transfer processes. The semi-circles aren't complete since the range of frequencies used is not wide enough, which makes it harder to quantify $R_{ct}$ with precision. However, visually we can observe that with AuNPs the semi-circle diameter and thus $R_{ct}$ decreases significantly, with an extrapolated value of $1\times10^5$ Ω . This way, despite initial CV results, AuNPs do appear to have a catalytic effect in the redox reaction.

$R_s$ also decreases with AuNPs, as seen in the inset graph that shows a zoomed view of the plot high-frequency region. Here the EIS spectrum interception with the X-axis will be closer to zero, with an extrapolated value of $1.6\times10^3$ Ω . Therefore, AuNPs enhance electron conduction, as expected due to their good conductivity.

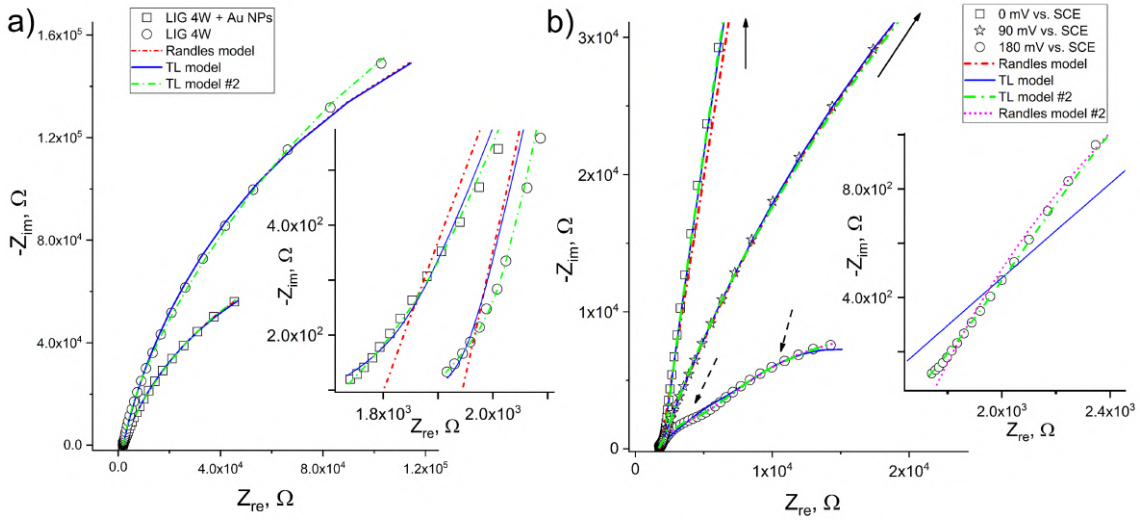


**Figure 4.7:** Nyquist plots containing EIS spectra of: **a)** LIG of 4 W and 4 W with AuNPs, with bias of 90mV vs. SCE and three fitting models applied to the data; **b)** LIG of 4 W with AuNPs, for three different bias: 0, 90 and 180 mV vs. SCE, and four fitting models applied. The inset graphs represent a zoomed view ot the EIS plots, for low values of $Z_{re}$.

In order to explain these frequency spectra, two main equivalent circuits were implemented to model LIG's response, illustrated in Figure 4.8. The most common method and first tried is the Randles circuit already discussed in section 3.4.2, which is only suitable for a continuous planar electrode surface, and in this case the Warburg impedance wasn't considered. The second one is the transmission line model, which is designed for uniformly distributed and cylindrical porous electrodes with a very high surface-volume ratio [114, 120]. It describes the stepwise flux of ions within a pore by repeating parallel and serially connected impedance elements along the pore depth [120].

A specific subset of the transmission line is the Bisquert Open (BTO) model, where electron transfer occurs only at the inner pore walls (active interface), disregarding the electrode's main surface and considering the base electrode inert. $R_{EL}$ represents the pore resistance to electrolyte diffusion and $\zeta$ refers to the reactions occurring at the inner pore walls. $\zeta$ is a parallel combination of resistor (describes charge transfer at the interface) and constant phase element, CPE or Q, which in an ideal case is treated as a capacitor, but practically it models capacitive behaviour due to surface

heterogeneity and porosity. These elements constitute the $R_{EL}\|\zeta$ block, whose repetition along the pore depth L is represented by the dashed lines [114, 120].

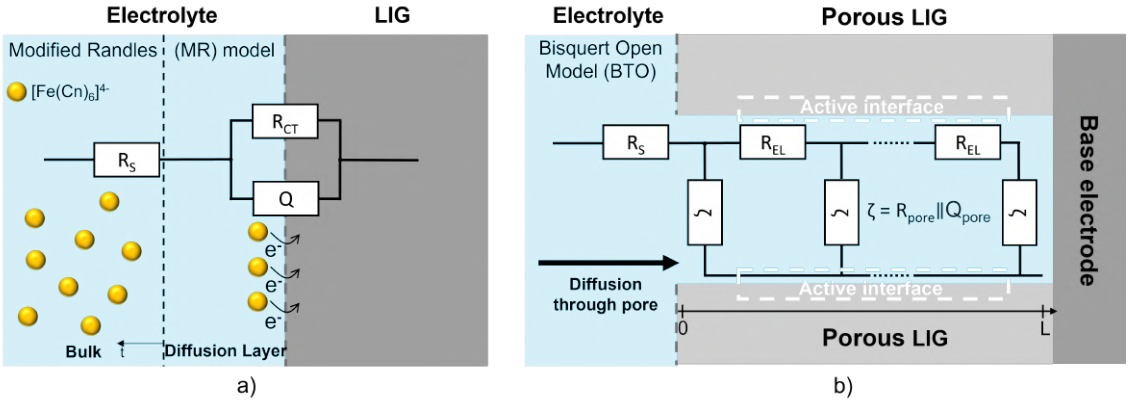


**Figure 4.8:** Schematic representation of the LIG-electrolyte interface and equivalent circuits models employed: **a)** Modified Randles model, where the diffusion layer increases as the electron transfer occurs; **b)** Bisquert Open model, where circuit elements are repeated along the pore depth.

Fittings were applied with these models to the spectra, using the Gamry Echem Analyst software. At very high frequencies (left side of the plot, zoomed in the inset graph), Randles model shows a poor fitting to the data, as it's unable to describe the electrochemical response of a complex porous electrode. In porous materials, the pore resistance to eletrolyte diffusion appears in EIS at high frequencies (slight curve region in inset graph) while charge transfer reactions occur at lower frequencies, opposite of what happens in a Nyquist plot of Randles model (Figure 3.5 in section 3.4.2).

Transmission line models can account for this porosity effect, as they show an adequate fitting to the data even in high frequencies, where BTO is named TL model, and a series combination of BTO with the Randles model is named TL model 2. This alternative model obtains an even better fitting than BTO, and was considered because of the results obtained in graph in Figure 2.8 b). Here, EIS spectra of 4 W LIG with AuNPs are shown for three different bias potentials ($V_{oc}$): 0, 90 and 180 mV vs. SCE. As this applied potential is increased, the beginning of the semi-circle becomes less steep, shortening its diameter and the charge transfer resistance ($3\times10^6$ Ω for 0 mV, $1\times10^5$ Ω for 90 mV and $3\times10^4$ Ω for 180 mV). This decrease occurs since 180 mV is the half-wave potential ($E_{1/2}$) of the 4 W LIG with AuNPs plot, as seen in Figure 4.6. This is the potential where transfer electron reactions are more favorable to occur. As the Nernst equation (3.1) explains, when applying a potential E equal to $E^0$ ($\sim E_{1/2}$), the $[Fe(CN)_6]^{4-}$ oxidizes until the produced $[Fe(CN)_6]^{3-}$ concentration becomes equal and equilibrium is reached. This maximizes redox reactions, whereas for a bias potential far away from $E^0$, only a small portion will reduce to $[Fe(CN)_6]^{3-}$, lowering redox currents and increasing $R_{ct}$, which confirms the higher slope for the 0 mV EIS plot.

An interesting phenomenon unveiled at 180 mV, where two semi-circles appear (signalized with two dashed arrows), one with a lower $R_{ct}$ than the other. For other bias plots this isn't visible because the higher $R_{ct}$ circle is dominating the spectrum and hindering the other process. These two semi-circles point to two distinct charge transfer processes, with different time constants associated to it. This is the reason for having considered the TL model 2 for fitting the data, since it employs a BTO in series with a resistance in paralel with a CPE (simply put, a serial connection of a BTO and a Randles equivalent circuit), where this last block represents another charge transfer process. Analysing the inset graph, it is clear that this TL model 2 is able to fit adequately both in high and lower frequencies, whereas only BTO deviates from the data. Another model consisting of two Modified Randles models serially connected (Randles model #2 in Figure 4.7b)) was tried in the fitting process but also deviates slightly from the data at high frequencies, failing to consider porosity.

Two possible explanations arise for these two charge transfer processes. There could be two

different types of pores in LIG, with different sizes for instance, where the smaller ones limit the electrolyte diffusion within the pores at high frequencies, described by a BTO model and bigger ones have a sufficient volume to easily allow the movement of ions, described by a standard Randles model. BTO itself isn't enough to model the complex structure and porosity hierarchization (which has been reported in the literature for general electrodes [121]), since in BTO only a uniform distribution of cylindrical pores is considered. Another hypothesis for the extra charge transfer process is that one semi-circle would be related to pore kinetics while the other would be related to kinetics of LIG's edge sites, known to play an important role in electron transfer, as previously mentioned in section 2.4.1.

## 4.3 Nitrite Detection

After electrochemical characterization, different nitrite concentrations detection measurements were followed, with DPV technique. A current peak appears around 0.75 V vs. SCE, as observed in Figures 4.9 and 4.10, corresponding to the electro-oxidation of nitrite, which follows the irreversible reaction in equation 4.3 and a second-order catalytic mechanism in equation 4.4 [10, 122]:

$$NO_2^- \rightarrow NO_2(g) + e^- \tag{4.3}$$

$$2NO_2 + H_2O \rightarrow NO_3^- + NO_2^- + 2H^+ \tag{4.4}$$

For nitrite detection, as mentioned before, a blank DPV in PBS is performed for the LIG electrode, before adding concentrations of nitrite. This serves as a reference signal or baseline to subtract to the DPV spectra of each nitrite concentration, in order for only the oxidation peak of nitrite to stand out. However, from measurement to measurement the signal presented notorious drifts compared to the blank signal, as observed in Figure 4.9 a) from blank data to 50 $\mu$M concentration of $NO_2^-$ data, specially in the OER region. This reaction generates molecular oxygen from aqueous solutions, increasing current from 0.6 V vs. SCE onward, as pointed out in Figure 4.9 a). The nitrite peak situates around 0.75 V vs. SCE, in which drifts of the OER tail make it difficult to extract the nitrite peak with precision through this method.

Therefore, an alternative method was employed using a mathematical baseline, via an exponential fitting to the data in every measurement, illustrated in red in Figure 4.9 a). Since the OER is only one faradaic phenomenon with a time constant associated, physically speaking a exponential fitting with only one time constant seems adequate to try and eliminate its contribution. Its general function is: $y = y_0 + A_1 e^{(x-x_0)/t_1}$, where $y_0$, $x_0$ and $A_1$ are constants that shift (vertically or horizontally) the function and expand/contract it, and $t_1$ is the time constant associated.

The fitted baseline was adjusted with some anchor points chosen outside the region where nitrite peak current starts to have influence. In blank DPV, where no nitrite was yet added, the fitting ideally should be equal to the data plot. However, the fitting isn't perfect in the intermediate area and there exists residual data from the baseline subtraction, which can be due to functional groups still present in LIG's surface that can cause redox activity.

These subtraction residuals are shown on the inset graph, with a maximum current close to $2.5\times10^{-8}$ A. This is of importance since nitrite peaks with comparable currents to the residual signal won't be significant. For instance, the 2.5 W signal of 50 uM of nitrite in the bottom part of Figure 4.9 b) is very close to the noise signal introduced by the exponential baseline, so that they are indistinguishable.

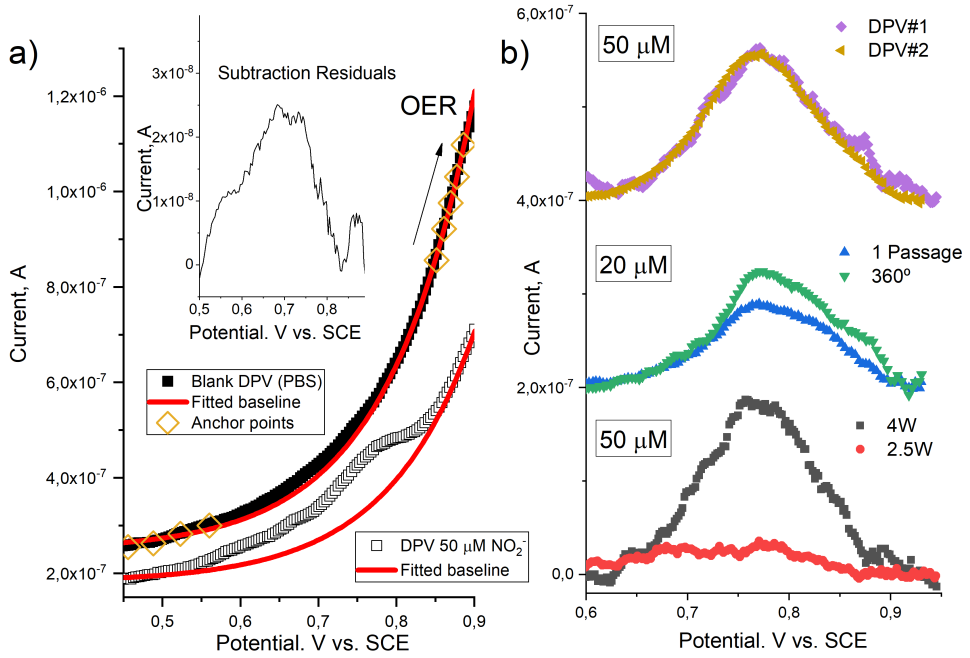


**Figure 4.9: a)** Exponential fitted baselines applied to blank DPV and 50 $\mu$M $NO_2^-$ data, with its anchor points located to the left and right of the nitrite potential region. The OER tail increases in an exponential fashion. Inset graph contains the subtraction of blank DPV with the baseline, yielding residual currents that reaches $\sim 2.5\times\ 10^{-8}$A. **b)** Comparison of laser and DPV parameters on the LIG electrodes, regarding electrochemical performance and detection of nitrite concentration.

Regarding 4 W LIG, its electrochemical performance in detecting nitrites is far superior to the 2.5 W LIG electrode, which may be attributed to its structure and morphology. As confirmed in the SEM images, 2.5 W lasing power seems to be almost at the threshold of LIG formation, where un-transformed PI regions are present, leading to heterogeneity in its morphology. Due to both these factors, 4 W was the parameter chosen to produce LIG electrodes for nitrite detection.

Another parameter tested in initial LIG samples was the number of times the laser irradiated the fiber, 1 passage and 4 passages (360° around the fiber). Both LIG electrodes presented similar measured limits of nitrite detection, of 20 $\mu$M. Note that the nitrite peak plots in the graph were shifted in intensity for visualization effects. Since the 360° LIG has a higher electroactive area than just LIG of one passage, it is expected that 360° LIG produces a higher current signal, as seen in the intermediate plot. However, this also increases capacitive and noise contributions making the detection signal comparable in both cases. Additionally, in 360° LIG production from laser irradiation, the fiber needs to be rotated manually from 90° to 90°, in a precise way (without bending the fiber for instance, which happened frequently). Due to this extra step of complexity and no improvements in nitrite detection by the 360° LIG, one passage was established for all produced LIG electrodes.

Lastly, DPV parameters were also compared in terms of detecting the nitrite signal. As observed in the top plot, they present very similar current values, for 50 $\mu$M of nitrite. However, DPV#1 can be seen to have more noise contributions than DPV#2. Moreover, there is a bigger impact of the OER tail in DPV#1 measurements, where before applying the baseline, the nitrite peak wasn't even visible due to overlap in the same potential. The same didn't occur in DPV#2, where the residual currents are much lower and a higher Signal-to-Noise Ratio (SNR) is obtained. This is specially important in the detection limit, 20 $\mu$M, where the nitrite signal is quite small and could be overlapped with noise when SNR is low, which is why DPV#2 were the chosen parameters.

All these LIG electrodes were functionalized with AuNPs. Nanoparticles are very important due to their high surface area and electrocatalytic effect, which decreases the potential necessary to occur

electron transfer between nitrite and LIG, and this way tries to escape the OER contribution. Specifically, AuNPs were chosen instead of other metal/carbon nanomaterials because it has been reported in the literature [10, 122] its excellent conductivity and catalytic effect on nitrite detection, enhancing selectivity to nitrite ions and giving rise to higher current signals at smaller potentials.

Ultimately the best conditions for LIG synthesis regarding nitrite detection were 4 W lasing power, irradiating the fiber only one time, with scanning speed of 150 mm/s. All sensors presented 0.5 cm of length and nitrite detection was measured with DPV#2 parameters. The results for nitrite detection in standard PBS (pH 7.5), with one of these LIG samples, are presented in Figure 4.10 a) in the intermediate plot.

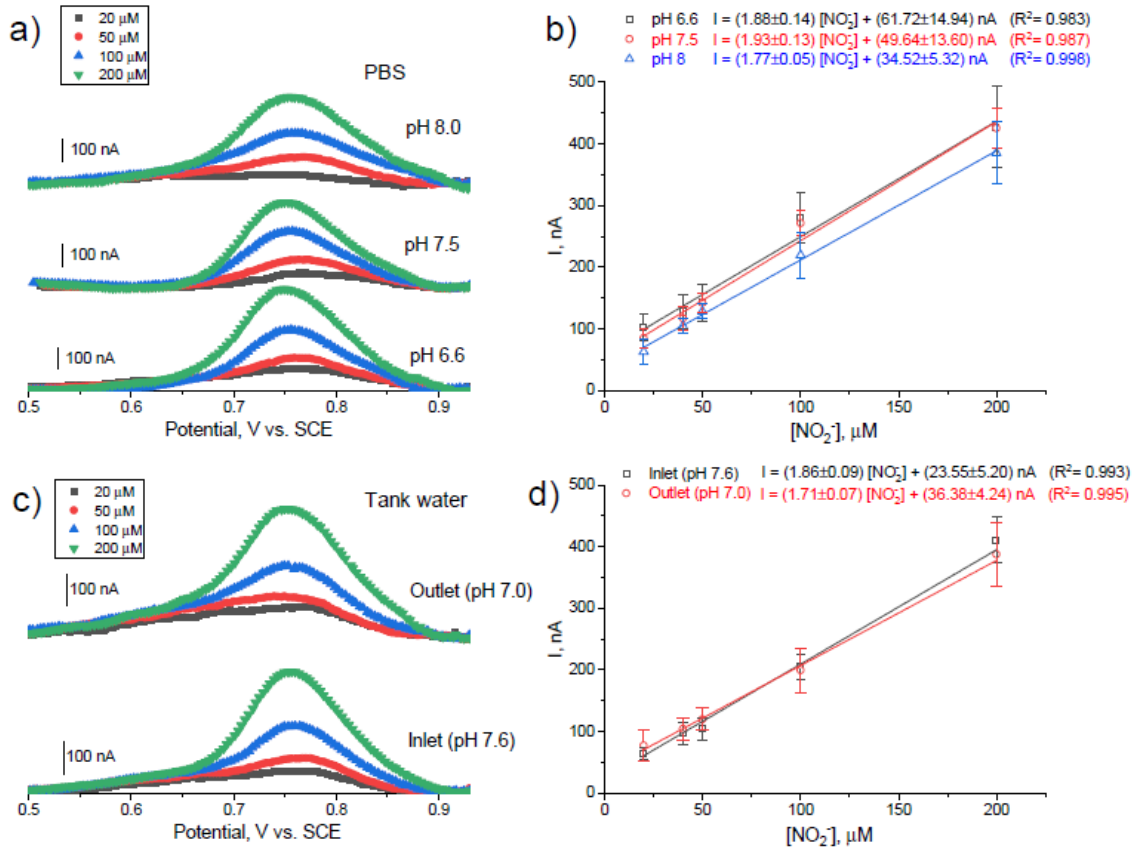


**Figure 4.10:** Electrochemical responses of LIG sensor for several nitrite concentrations, regarding three different pHs of PBS solution, in **a)**, and two real water samples, before (inlet) and after (outlet) entering the aquaculture tank, in **c)**. Graphs of the peak currents plotted against the $NO_2^-$ concentrations introduced in PBS, for its three different types of pH, in **b)**, and for intlet and outlet samples, in **d)**. Error bars show the variability in results from three LIG sensors, and linear fittings were applied to view the linear range and sensitivity of the sensor.

Here the nitrite oxidation peak is represented for each concentration of 20, 50,100 and 200 $\mu$M, and shows the current curve increasing with the nitrite concentration, while the nitrite potential remained approximately the same. Lower concentrations from 10 to 1 $\mu$M were tested, however the small currents were comparable to subtraction residual values, adding uncertainty to whether the measured signal corresponded to nitrite oxidation or noise. Higher concentrations up until 500 $\mu$M were studied as well but the peak current's intensity appeared to reach a steady state, either due to the sensor's saturation, having reached the maximum of its detection range, or to fouling effects. Fouling phenomenon consists in adsorption of chemical species to the LIG's surface, in this case possibly the irreversible adsorption of $NO_2^-$ and/or its oxidation byproducts. They occupy and diminish the

electroactive area for redox reactions, and consequently could limit the redox currents when they should be increasing with concentration.

This way, the linear detection range of this LIG sensor is from 20-200 $\mu$M, as demonstrated in Figure 4.10b) in red, where the peak current intensity increases linearly with the concentration, with a decent linear regression of $R^2 = 0.987$ and a sensitivity equal to its slope, of (1.93 $\pm$ 0.13) nA/$\mu$M. Regarding the LOD, it describes the smallest concentration of an analyte that can be reliably measured by an analytical procedure. It can be estimated via the lowest measured concentration, which in this case is 20 $\mu$M, with a current around 100 nA (higher than the noise value of 30 nA).

Compared to other carbon-based electrodes' reported in the literature, such as the ones in Table 2.1, the value found of 20 $\mu$M is generally higher by one or two orders of magnitude, but can also be comparable in some cases. When comparing to the only paper reporting a LIG electrode for nitrite detection in [10], their measured LOD is 10 $\mu$M, which is similar to this work's LOD. Regarding the linear range, this work's is slightly wider than theirs. These discrepancies in LOD values may derive from the geometry of LIG produced, since so far no reports of LIG produced on fiber have been found, and these present a smaller and perhaps cylindrical-shaped LIG rather than planar LIG electrodes produced on Kapton sheets.

The reproducibility of this LIG sensor was also analysed. The error bars in the plot represent the variability of current values of this LIG sensor with two other LIG electrodes measured in the same round (same electrolyte solution and conditions), as the electrochemical cell allowed three LIG electrodes to be placed at the same time. The error bars are generally small, with exception of 200 $\mu$M, where it shows a greater uncertainty. However, for its most part, the LIG nitrite sensors produced with these parameters and conditions show similar responses, with the same linear range and same LOD, indicating a good reproducibility of this type of sensor.

Afterwards, the pH effect on electrochemical response was evaluated on PBS, using the results from pH 7.5 and and adding two extra values of pH (6.6 and 8). As can be seen, the nitrite odixation potential remains constant with pH, and the current response is similar, however it slightly decreases with increasing pH. This in accordance to similar studies reported in the literature [10, 122]. In other words, slight pH variations (shift in concentration of $H^+$) don't seem to have a great influence in the nitrite ion concentration in the solution. This is of importance in aquaculture to maintain constant the nitrite intake in fish and consequently not increase its toxicity.

In order to validate the pratical use of the proposed sensor, the LIG on fiber electrode was used for nitrite detection in aquaculture water samples, before entering the water tank (inlet) and after entering it (outlet). Nitrites can be expected to be found in the oulet water sample, due to the nitrogen cycle in aquaculture tanks. So firstly, to verify this, a blank DPV was performed and no evidence of a nitrite peak was found, meaning that either the nitrification process occurred efficiently and no nitrites were present, or that they were in concentrations lower than the sensor's LOD. Next, the same procedure in PBS of adding nitrite concentrations was performed in these water samples, inlet and outlet, and the results can be found in Figures 4.10 c) and d). The peak current also increases linearly with the concentrations, for both cases, with a $R^2$ of 0.993 for inlet water, and $R^2$ of 0.995 for outlet. The response obtained is very similar between inlet and outer samples, which have different chemical composition, showing the adaptability of the LIG sensor to various solutions. The linear range and LOD are the same as the one obtained for PBS, and show sensitivities (1.86 $\pm$ 0.09 nA/$\mu$M for inlet, 1.71 $\pm$ 0.07 nA/$\mu$M for outlet) comparable to those in PBS, specifically the inlet water with pH 7.6 and the PBS with pH 7.5, whose sensibilities are within their margin of error. In this samples LIG sensor also shows reproducibility in results, with increasing error bars for greater concentrations (200 $\mu$M).

Fouling and interference of organic matter, which could be more evident in outlet sample, in the nitrite peak intensity weren't found. Additionally, in both responses, no evidence of interfering electroactive species was found for the whole potential window, as the nitrite peak was the only observable, which can possibly point towards an adequate selectivity to nitrite ions from the LIG sensor.

## 4.4 Hybrid Sensor

After successfully fabricating the LIG nitrites sensor, an hybrid platform was created by integrating the optical sensor with a POF pH sensor in order to exchange information retrieved from each other's measurements.

After the calibration step of the pH sensor using HCl (0.1 M), HCl was removed and 30 ml of PBS was added. As the polyaniline is transitioning from a protonated to a deprotonated state, since PBS has a defined pH of 7.4, the sensor was immersed in PBS for about 5 minutes to ensure signal stabilization. Subsequently, 1.5 ml of nitrite-containing PBS (1 mM stock nitrite concentration in 200 ml) was added to the original 30 ml of PBS, corresponding to $\sim$ 50 $\mu$M (47.6 $\mu$M actually, because total volume went from 30 to 31.5 ml). For both PBS and 50 $\mu$M measurements shown in Figure 4.11, a magnetic stirrer was used to homogenize the solution. These time periods are represented with 'H. Start' and 'H. Stop' in the figure.

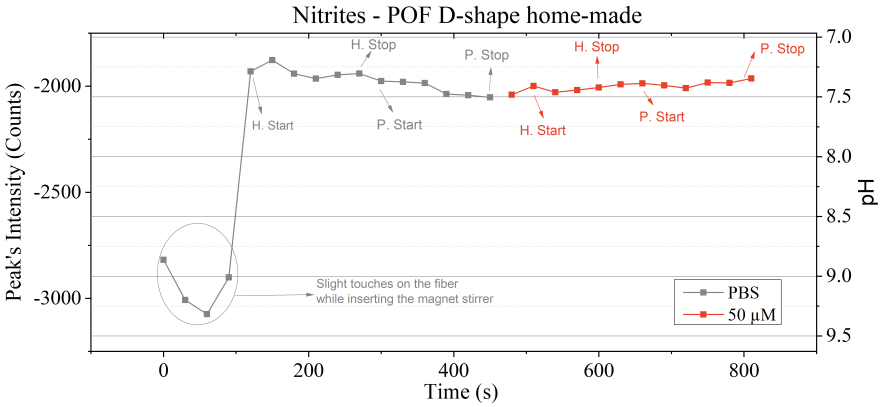


**Figure 4.11:** Monitoring of the optical signal's peak evolution as nitrites are added in three instants, in steps 0f 50 $\mu$M.'H. Start' and 'H. Stop' stand for homogenize start and stop, respectively, and 'P. Start' and 'P. Stop' stand for the beginning and end of the potentiostat measurements, respectively. Image shared with permission from the owner.

After the solution is properly homogenized, the stirring stops and DPV measurements of the potentiostat began, also represented by 'P. Start' and 'P.Stop' in the plot. During this time, the spectrometer is simultaneously saving spectra with intervals of 30 seconds. A reference spectrum using HCl was subtracted from all the spectra, and the evolution throughout time of the peak signal's intensity (equivalent to the pH axis on the right of the graph) is shown in Figure 4.11.

As Figure 4.11 shows, the transmission signal and thus pH remains constant with addition of nitrites in the PBS solution. Although nitrites are considered a weak base and its introduction to the solution could possibly decrease the pH, no major changes occurred, which is expected due to the PBS behaviour. PBS is a buffer solution, meaning that it is resistant to acids/bases additions, maintaining its pH constant. Here, it slightly varies its pH between 7.3 and 7.5 values, when potentiostat measurements are undergoing. The real concentration of $NO_2^-$ introduced in the solution was 47.60 $\mu$M, which corresponded to a signal's peak current of 133.07 nA. This value was introduced in the calibration curves produced in the previous section 4.3 in Figure 4.10, for both 7.5 pH and 8 pH. As seen in Table 4.1, for calibration curve of pH 7.5, it gives a $NO_2^-$ concentration of 43.20 $\mu$M, which constitutes a recovery of 90% to the real value. Indeed, the measured current is within the standard deviation of the calibration curve measurements for 50 $\mu$M at PBS 7.5 pH (142 $\pm$ 17 nA). The $NO_2^-$ concentration value obtained for calibration curve of pH 8 was 55.65 $\mu$M, with a recovery of almost 117%, a considerable difference to the real value. This showcases the importance of having multiparametric measurements. Not only pH is an important parameter in water quality monitoring, but it also allows to choose the proper calibration curve of the electrochemical sensor for more accurate results.

**Table 4.1:** Comparison between the $NO_2^-$ concentrations obtained with calibration plots of 7.5 and 8 pH, and the real $NO_2^-$ value.

| **Real [$NO_2^-$] ($\mu$M)** | **$NO_2^-$ current peak (nA)** | **[$NO_2^-$] for pH 7.5 calibration line ($\mu$M)** | **Recovery (%)** | **[$NO_2^-$] for pH 8 calibration line ($\mu$M)** | **Recovery (%)** |
|---|---|---|---|---|---|
| 47.60 | 133.07 | 43.20 | 90.76 | 55.65 | 116.91 |

# CHAPTER 5

## Conclusions and Future Work

Considering the fragile equilibrium on which aquaculture systems stand, there is a rising need in developing a network of in-situ autonomous sensors that can quickly monitor the water quality, by providing multi-parametric data regarding pH, temperature, nitrites concentration, among others. It is also vital to combine the different transduction mechanisms of these sensors into a miniaturized platform than can be safely placed in the water tanks, which can be done with optical fibers. This way, in this work innovative LIG electrochemical sensors were sucessfully produced directly on the exterior surface of optical fibers coated with polyimide, in order to study its performance in detecting nitrites (on real aquaculture water samples) and ultimately integrate the sensor in a hybrid sensing system with an optical pH sensor, in the same fiber line.

Through SEM analysis, it is observed that LIG produced at 2.5 W presents a heterogeneous morphology, with non-porous regions where PI was not transformed into LIG. Therefore, 2.5 W laser power appears to be near the threshold for LIG formation, whereas the LIG produced at 4 W denotes a homogeneous morphology constituted by interconnected multilayer graphene flakes in a highly porous arrangement. This is in agreement with the literature that shows that porosity increases with laser fluence. Raman measurements for 2.5 W LIG show increased intensity of the amorphous-carbon (a-C) band compared to 4 W LIG as well as broader D and G bands and higher $I_D/I_G$ ratio, meaning that it has a higher defect density and lower crystallinity degree. This also suggests that in fact 2.5 W laser power, in conjuction with other laser parameters, results in a laser fluence that is near to the threshold for LIG formation. Finally, EDX measurements allowed to conclude that dropcasting tecnhique successfully deposits AuNPs in LIG's surface while dip-coating technique does not.

Electrochemical characterization was performed in PBS using the $[Fe(CN)_6]^{4-}$ redox pair for 2.5 W, 4 W and 4 W+AuNPs LIGs. Peak currents scaled with the potential scan rate in accordance to the Randles-Sevcik equation, a sign of a reversible process in a planar semi-infinite diffusion regime. A decrease in redox kinetics in the direction 2.5 W→4 W→4 W+AuNPs is observed, opposite to the reported in the literature where AuNPs are seen to increase redox kinetics. However, a careful analysis of CV peak shapes reveals much broader peak shapes for 4 W LIGs, which suggests an important contribution of charge diffusion within the pores of LIG. This hinders a correct assessment in terms of redox kinetics via CV measurements. Porosity effects were corroborated by EIS results, showing that Randles equivalent circuits, commonly employed for analysis of planar, non-porous electrodes, fail to describe the EIS reponse of 4 W LIGs, whereas transmission line models that consider porosity effects successfully describe the EIS spectra. EIS measurements also show two distinct charge transfer mechanisms, possibly due to a bimodal distribution of pore sizes (e.g. meso and micropores) or to redox reactions occuring both within the pores and at the LIG's edge sites, which are known to possess high electrochemical activity. Regardless, these measurements undoubtedly point to the existence of electrochemically active porosity that is desirable regarding analyte detection, since it maximizes surface/electrolyte interface and thus detection events.

Regarding nitrite detection, the electrochemical responses of LIG sensors produced with different parameters were compared, and the best results were obtained for 4 W LIG produced with one laser passage modified with AuNPs. The detection range for this LIG sensor is linear from 20-200 $\mu$M, with a sensitivity of (1.93 ± 0.13) nA/$\mu$M and the measured LOD is 20 $\mu$M, which is relatively higher compared to some carbon-based electrodes, but comparable to another LIG electrode (LOD = 10 $\mu$M). The sensor was calibrated for pH in PBS and it was found that the peak currents relative to electro-oxidation of nitrite remain similar within the pH range tested (6.6 to 8), with sensitivities between

1.88 nA/$\mu$M and 1.77 nA/$\mu$M, slightly decreasing with pH, which is in agreement with the literature. The LIG sensor also has similar electrochemical responses when detecting nitrite in aquaculture water samples, before and after entering RAS, showing sensitivities of (1.86 $\pm$ 0.09) nA/$\mu$M and (1.71 $\pm$ 0.07) nA/$\mu$M respectively, a linear range of 20-200 $\mu$M and a measured LOD is 20 $\mu$M, which is lower than the 43 $\mu$M concentration of nitrites considered toxic to fish by the company that supplied the samples. Thus, the sensor is adequate to detect nitrites in real water samples in the relevant concentration range. Moreover, nitrites could not be detected in aquaculture waters and hence their concentration were below the sensor LOD. Finally, no supplementary DPV signal from other water components/contaminants was detected, which is beneficial regarding selectivity towards nitrites.

Regarding the integration of the LIG sensor into a hybrid sensing system, since the interrogator used to monitor the tapered pH sensors was malfunctioning, a POF D-shape home-made sensor had to be integrated in the electrochemical cell used for nitrite measurements, creating a hybrid platform. The D-shaped pH sensor measure pH values simultaneously with the electrochemical measurements of nitrite added to the PBS solution. Results showed that the pH remained overall constant, only slightly varying between 7.3 and 7.5 pH, an expected result as PBS is a buffer solution resistant to acids/bases introduction, such as $NO_2^-$. This pH data was used to choose the proper pH-dependent calibration curve of the electrochemical sensor and a satisfactory nitrite concentration recovery of 90% was obtained. This is an especially important feature when analysing non-buffered solutions, such as aquaculture waters.

Future work involves the optimization and automation of electrical contacts' production and insulation, in order to decrease its complexity, as aligning manually the copper wire with the fiber and gluing it with silver ink proved to be difficult and time-consuming. On the other hand, one limitation found in this work was the superposition of the oxygen evolution reaction (OER) tail on the signal from nitrites. In this sense, other catalytic nanomaterials could be deposited on the LIG's surface, such as PtNPS or CNTs, in an attempt to further decrease the oxidation potential of the nitrites peak, this way minimizing the impact of the OER tail on nitrite detection.

Further work is also related to development of an optical way of detecting nitrites, taking advantage of the multiple transduction possibilities offered by this LoF concept. This way, in-situ counterproofing using different signals is enabled, enhancing the accuracy of the measurements and minimizing false-positive or false-negative results. It could also allow for complementary detection ranges, enlarging the dynamic range of the measurements. For instance, by inscribing a grating structure directly on the PI fiber (such as a tilted FBG), and since LIG is coated with AuNPs, SPR phenomenon could take part and changes in the refractive index could occur in the presence of nitrites in LIG's surface.

Another point focus should be the hybrid integration of the LIG electrochemical sensor with the optical pH sensor in the same fiber line, in the scope of LoF, with an optical interrogator. However, it would be recommended to try and find alternative sensors for tapers and splicing process, since these are fragile and the splicing process of the tapered fiber with the PI fiber containing the LIG sensor proved to be difficult. For example, an alternative could be producing LIG directly on PMMA, the material of the POF core, however no reports of this in the literature were found so far. Therefore, it seems that a way must be found to deposit polyimide on the POF containing the pH sensor, perhaps by placing liquid PI on the fiber and then producing LIG there, but thickness and homogeneity of the PI coating would need to be carefully controlled.

Besides nitrites and pH, other parameters and analytes are of interest to be introduced in the hybrid platform, such as water turbidity sensors and bacteria, bromide or cortisol sensors, all of major importance in aquaculture water monitoring for healthy fish development.

# Bibliography


[1] United Nations. Do you know all 17 SDGs? https://sdgs.un.org/goals. Accessed in June, 2022.

[2] FAO. The State of World Fisheries and Aquaculture: Towards Blue Transformation. https://www.fao.org/state-of-fisheries-aquaculture. Accessed in June, 2022.

[3] Jaap Van Rijn. Waste treatment in recirculating aquaculture systems. *Aquacultural Engineering*, 53:49–56, 2013.

[4] CIM Martins, Ep H Eding, Marc CJ Verdegem, Leon TN Heinsbroek, Oliver Schneider, Jean-Paul Blancheton, E Roque d'Orbcastel, and JAJ Verreth. New developments in recirculating aquaculture systems in europe: A perspective on environmental sustainability. *Aquacultural engineering*, 43(3):83–93, 2010.

[5] Z Svobodova, J Machova, G Poleszczuk, J Hůda, J Hamáčková, H Kroupova, et al. Nitrite poisoning of fish in aquaculture facilities with water-recirculating systems. *Acta Veterinaria Brno*, 74(1):129–137, 2005.

[6] DIGIAQUA. Digitizing Aquaculture. https://www.digiaqua.eu/. Accessed in June, 2022.

[7] Patrizio Vaiano, Benito Carotenuto, Marco Pisco, Armando Ricciardi, Giuseppe Quero, Marco Consales, Alessio Crescitelli, Emanuela Esposito, and Andrea Cusano. Lab on fiber technology for biological sensing applications. *Laser & Photonics Reviews*, 10(6):922–961, 2016.

[8] A Ricciardi, M Consales, G Quero, A Crescitelli, E Esposito, and A Cusano. Lab-on-fiber devices as an all around platform for sensing. *Optical Fiber Technology*, 19(6):772–784, 2013.

[9] Maoxiang Hou, Neng Wang, Yun Chen, Zhengping Ou, Xin Chen, Fangcheng Shen, and Haiming Jiang. Laser-induced graphene coated hollow-core fiber for humidity sensing. *Sensors and Actuators B: Chemical*, 359:131530, 2022.

[10] Salem Nasraoui, Ammar Al-Hamry, Priscila Rios Teixeira, Sami Ameur, Leonardo G Paterno, Mounir Ben Ali, and Olfa Kanoun. Electrochemical sensor for nitrite detection in water samples using flexible laser-induced graphene electrodes functionalized by cnt decorated by au nanoparticles. *Journal of Electroanalytical Chemistry*, 880:114893, 2021.

[11] Qiu-Hua Wang, Li-Ju Yu, Yang Liu, Lan Lin, Ri-gang Lu, Jian-ping Zhu, Lan He, and Zhong-Lin Lu. Methods for the detection and determination of nitrite and nitrate: A review. *Talanta*, 165:709–720, 2017.

[12] Xunjia Li, Jianfeng Ping, and Yibin Ying. Recent developments in carbon nanomaterial-enabled electrochemical sensors for nitrite detection. *TrAC Trends in Analytical Chemistry*, 113:1–12, 2019.

[13] Zhao Yilong, Zhao Dean, and Li Daoliang. Electrochemical and other methods for detection and determination of dissolved nitrite: A review. *Int. J. Electrochem. Sci*, 10(2):1144–1168, 2015.

[14] Alexander Ciji and Mohammad Shahbaz Akhtar. Nitrite implications and its management strategies in aquaculture: A review. *Reviews in Aquaculture*, 12(2):878–908, 2020.

[15] Maartje AHJ van Kessel, Harry R Harhangi, Katinka van de Pas-Schoonen, Jack van de Vossenberg, Gert Flik, Mike SM Jetten, Peter HM Klaren, and Huub JM Op den Camp. Biodiversity of n-cycle bacteria in nitrogen removing moving bed biofilters for freshwater recirculating aquaculture systems. *Aquaculture*, 306(1-4):177–184, 2010.

[16] Hana Kroupova, J Machova, Z Svobodova, et al. Nitrite influence on fish: a review. *Veterinarni medicina-praha-*, 50(11):461, 2005.

[17] Inc. Living Arts Aquatic. Here's Why the Nitrogen Cycle is Important for the Health and Well-Being of Your Fish. https://livingartaquatics.com/why-is-the-nitrogen-cycle-important-for-your-aquarium/. Accessed in September, 2022.

[18] DW Huey, TL Beitinger, and MC Wooten. Nitrite-induced methemoglobin formation and recovery in channel catfish (ictalurus punctatus) at three acclimation temperatures. *Bull. Environ. Contam. Toxicol.;(United States)*, 32(6), 1984.

[19] Zewen Zhang, Wenwu Mao, Zijie Wang, Xiaolin Tan, Fan Wu, Dengkui Wang, and Xiong Fang. Development of remote monitoring system for aquaculture water quality based on internet of things. In *IOP Conference Series: Materials Science and Engineering*, volume 768, page 052033. IOP Publishing, 2020.

[20] Katrina M Miranda, Michael G Espey, and David A Wink. A rapid, simple spectrophotometric method for simultaneous detection of nitrate and nitrite. *Nitric oxide*, 5(1):62–71, 2001.

[21] Priyanka Singh, Manish Kumar Singh, Younus Raza Beg, and Gokul Ram Nishad. A review on spectroscopic methods for determination of nitrite and nitrate in environmental samples. *Talanta*, 191:364–381, 2019.

[22] Shoji Motomizu, Hiroshi Mikasa, and Kyoji Tôei. Fluorimetric determination of nitrate in natural waters with 3-amino-1, 5-naphthalenedisulphonic acid in a flow-injection system. *Analytica chimica acta*, 193:343–347, 1987.

[23] Yan Xiong, Cheng-Jie Wang, Tao Tao, Ming Duan, Shen-Wen Fang, and Min Zheng. A miniaturized fiber-optic colorimetric sensor for nitrite determination by coupling with a microfluidic capillary waveguide. *Analytical and bioanalytical chemistry*, 408(13):3413–3423, 2016.

[24] Zlatuše Legnerová, Petr Solich, Hana Sklenářová, Dalibor Šatínskỳ, and Rolf Karlíček. Automated simultaneous monitoring of nitrate and nitrite in surface water by sequential injection analysis. *Water Research*, 36(11):2777–2783, 2002.

[25] Like Li, Ya-nan Zhang, Yifan Zhou, Wanlu Zheng, Yutong Sun, Guoming Ma, and Yong Zhao. Optical fiber optofluidic bio-chemical sensors: a review. *Laser & Photonics Reviews*, 15(7):2000526, 2021.

[26] Yan Xiong, Dao-qian Zhu, Chun-feng Duan, Jian-wei Wang, and Ya-feng Guan. Small-volume fiber-optic evanescent-wave absorption sensor for nitrite determination. *Analytical and bioanalytical chemistry*, 396(2):943–948, 2010.

[27] Xinghua Yang, Tingting Yuan, Guoqiang Yue, Entao Li, and Libo Yuan. Optofluidic integrated in-fiber fluorescence online optical fiber sensor. *Sensors and Actuators B: Chemical*, 215:345–349, 2015.

[28] Guangli Li, Yonghui Xia, Yaling Tian, Yiyong Wu, Jun Liu, Quanguo He, and Dongchu Chen. Recent developments on graphene-based electrochemical sensors toward nitrite. *Journal of the Electrochemical Society*, 166(12):B881, 2019.

[29] Li Fu, Shuhong Yu, Lachlan Thompson, and Aimin Yu. Development of a novel nitrite electrochemical sensor by stepwise in situ formation of palladium and reduced graphene oxide nanocomposites. *RSC Advances*, 5(50):40111–40116, 2015.

[30] Abbas Afkhami, Farzaneh Soltani-Felehgari, Tayyebeh Madrakian, and Hamed Ghaedi. Surface decoration of multi-walled carbon nanotubes modified carbon paste electrode with gold nanoparticles for electro-oxidation and sensitive determination of nitrite. *Biosensors and Bioelectronics*, 51:379–385, 2014.

[31] MA Parvez Mahmud, Fatemeh Ejeian, Shohreh Azadi, Matthew Myers, Bobby Pejcic, Rouzbeh Abbassi, Amir Razmjou, and Mohsen Asadnia. Recent progress in sensing nitrate, nitrite, phosphate, and ammonium in aquatic environment. *Chemosphere*, 259:127492, 2020.

[32] Fangxin Hu, Shihong Chen, Chengyan Wang, Ruo Yuan, Dehua Yuan, and Cun Wang. Study on the application of reduced graphene oxide and multiwall carbon nanotubes hybrid materials for simultaneous determination of catechol, hydroquinone, p-cresol and nitrite. *Analytica chimica acta*, 724:40–46, 2012.

[33] Nurul Izrini Ikhsan and Perumal et.al Rameshkumar. Facile synthesis of graphene oxide–silver nanocomposite and its modified electrode for enhanced electrochemical detection of nitrite ions. *Talanta*, 144:908–914, 2015.

[34] Sen Liu, Jingqi Tian, Lei Wang, Yonglan Luo, and Xuping Sun. Production of stable aqueous dispersion of poly (3, 4-ethylenedioxythiophene) nanorods using graphene oxide as a stabilizing agent and their application for nitrite detection. *Analyst*, 136(23):4898–4902, 2011.

[35] Zhuang Li, Zhenzhen An, Yongyang Guo, Kangning Zhang, Xiaoling Chen, Dongxia Zhang, Zhonghua Xue, Xibin Zhou, and Xiaoquan Lu. Au-pt bimetallic nanoparticles supported on functionalized nitrogen-doped graphene for sensitive detection of nitrite. *Talanta*, 161:713–720, 2016.

[36] Zhenjing Zhuang, Haiqin Lin, Xiong Zhang, Fei Qiu, and Huiyong Yang. A glassy carbon electrode modified with carbon dots and gold nanoparticles for enhanced electrocatalytic oxidation and detection of nitrite. *Microchimica Acta*, 183(10):2807–2814, 2016.

[37] Carlos Marques. *Fiber-Optic Components for Optical Communications and Sensing*. PhD thesis, Universidade de Aveiro, 2013.

[38] Maria Soares. Optical Fiber Imunnosensors Based on SPR for Cortisol Detection. Master's thesis, Universidade de Aveiro, 2021.

[39] Hisham Kadhum Hisham. Optical fiber sensing technology: basics, classifications and applications. *Am. J. Remote Sens*, 6(1):1–5, 2018.

[40] Raymond A Serway and John W Jewett. *Physics for scientists and engineers*. Cengage learning, 2018.

[41] Maria Simone Soares, Miguel Vidal, Nuno F Santos, Florinda M Costa, Carlos Marques, Sónia O Pereira, and Cátia Leitão. Immunosensing based on optical fiber technology: recent advances. *Biosensors*, 11(9):305, 2021.

[42] Tarsem Lal Singal. *Optical fiber communications: principles and applications*. Cambridge University Press, 2016.

[43] Victor Giurgiutiu. *Structural health monitoring of aerospace composites*. Academic Press, 2015.

[44] Pedro J Rivero, Javier Goicoechea, and Francisco J Arregui. Optical fiber sensors based on polymeric sensitive coatings. *Polymers*, 10(3):280, 2018.

[45] Changxu Li, Wenlong Yang, Min Wang, Xiaoyang Yu, Jianying Fan, Yanling Xiong, Yuqiang Yang, and Linjun Li. A review of coating materials used to improve the performance of optical fiber sensors. *Sensors*, 20(15):4215, 2020.

[46] Kyung-Il Joo, Yeonjeong Han, Yong Wook Lee, Chang-sub Park, Seong Ho Kong, Shin-Won Kang, and Hak-Rin Kim. Optical sensing of solvents using selective tensile effects of a pdms-coated fiber bragg grating. In *SENSORS, 2010 IEEE*, pages 1645–1648. IEEE, 2010.

[47] Junjie Jiang, Lianhong Zhong, Xinhui Duan, Meng Song, Li Li, Zeming Wu, Zhuyong Li, Zhen Huang, Zhiyong Hong, Zhijian Jin, et al. Bend limitation of a polyimide-coated optical fiber at cryogenic temperature of 77 k. *IEEE Transactions on Applied Superconductivity*, 29(2):1–5, 2018.

[48] Jianxin Zhang, Xueyun Shen, Miao Qian, Zhong Xiang, and Xudong Hu. An optical fiber sensor based on polyimide coated fiber bragg grating for measurement of relative humidity. *Optical Fiber Technology*, 61:102406, 2021.

[49] Shuhui Liu, Shaoqing Cao, Zhe Zhang, Ying Wang, Changrui Liao, and Yiping Wang. Temperature sensor based on side-polished fiber spr device coated with polymer. *Sensors*, 19(19):4063, 2019.

[50] Shouzhen Jiang, Zhe Li, Chao Zhang, Saisai Gao, Zhen Li, Hengwei Qiu, Chonghui Li, Cheng Yang, Mei Liu, and Yanjun Liu. A novel u-bent plastic optical fibre local surface plasmon resonance sensor based on a graphene and silver nanoparticle hybrid structure. *Journal of Physics D: Applied Physics*, 50(16):165105, 2017.

[51] Bohdan Kulyk, Maria A Freitas, Nuno F Santos, Farzin Mohseni, Alexandre F Carvalho, Kiryl Yasakau, António JS Fernandes, Adriana Bernardes, Bruno Figueiredo, Rui Silva, et al. A critical review on the production and application of graphene and graphene-based materials in anti-corrosion coatings. *Critical Reviews in Solid State and Materials Sciences*, 47(3):309–355, 2022.

[52] Andre K Geim and Konstantin S Novoselov. The rise of graphene. In *Nanoscience and technology: a collection of reviews from nature journals*, pages 11–19. World Scientific, 2010.

[53] Yanwu Zhu, Shanthi Murali, Weiwei Cai, Xuesong Li, Ji Won Suk, Jeffrey R Potts, and Rodney S Ruoff. Graphene and graphene oxide: synthesis, properties, and applications. *Advanced materials*, 22(35):3906–3924, 2010.

[54] Kostya S Novoselov, Andre K Geim, Sergei V Morozov, De-eng Jiang, Yanshui Zhang, Sergey V Dubonos, Irina V Grigorieva, and Alexandr A Firsov. Electric field effect in atomically thin carbon films. *science*, 306(5696):666–669, 2004.

[55] Kirill I Bolotin, K J Sikes, Zhifang Jiang, M Klima, G Fudenberg, James Hone, Phaly Kim, and Horst L Stormer. Ultrahigh electron mobility in suspended graphene. *Solid state communications*, 146(9-10):351–355, 2008.

[56] Changgu Lee, Xiaoding Wei, Jeffrey W Kysar, and James Hone. Measurement of the elastic properties and intrinsic strength of monolayer graphene. *science*, 321(5887):385–388, 2008.

[57] Alexander A Balandin, Suchismita Ghosh, Wenzhong Bao, Irene Calizo, Desalegne Teweldebrhan, Feng Miao, and Chun Ning Lau. Superior thermal conductivity of single-layer graphene. *Nano letters*, 8(3):902–907, 2008.

[58] Konstantin S Novoselov, L Colombo, PR Gellert, MG Schwab, K Kim, et al. A roadmap for graphene. *nature*, 490(7419):192–200, 2012.

[59] Caterina Soldano, Ather Mahmood, and Erik Dujardin. Production, properties and potential of graphene. *Carbon*, 48(8):2127–2150, 2010.

[60] Michael J McAllister, Je-Luen Li, Douglas H Adamson, Hannes C Schniepp, Ahmed A Abdala, Jun Liu, Margarita Herrera-Alonso, David L Milius, Roberto Car, Robert K Prud'homme, et al. Single sheet functionalized graphene by oxidation and thermal expansion of graphite. *Chemistry of materials*, 19(18):4396–4404, 2007.

[61] Roberto Munoz and Cristina Gómez-Aleixandre. Review of cvd synthesis of graphene. *Chemical Vapor Deposition*, 19(10-11-12):297–322, 2013.

[62] Yu Wang, Yi Zheng, Xiangfan Xu, Emilie Dubuisson, Qiaoliang Bao, Jiong Lu, and Kian Ping Loh. Electrochemical delamination of cvd-grown graphene film: toward the recyclable use of copper catalyst. *ACS nano*, 5(12):9927–9933, 2011.

[63] William S Hummers Jr and Richard E Offeman. Preparation of graphitic oxide. *Journal of the american chemical society*, 80(6):1339–1339, 1958.

[64] Jian Lin, Zhiwei Peng, Yuanyue Liu, Francisco Ruiz-Zepeda, Ruquan Ye, Errol LG Samuel, Miguel Jose Yacaman, Boris I Yakobson, and James M Tour. Laser-induced porous graphene films from commercial polymers. *Nature communications*, 5(1):1–8, 2014.

[65] Fangcheng Wang, Kedian Wang, Buxiang Zheng, Xia Dong, Xuesong Mei, Jing Lv, Wenqiang Duan, and Wenjun Wang. Laser-induced graphene: preparation, functionalization and applications. *Materials technology*, 33(5):340–356, 2018.

[66] Laurence W McKeen. *The effect of sterilization on plastics and elastomers*. William Andrew, 2018.

[67] Ruquan Ye, Dustin K James, and James M Tour. Laser-induced graphene: from discovery to translation. *Advanced Materials*, 31(1):1803621, 2019.

[68] Ruquan Ye, Yieu Chyan, Jibo Zhang, Yilun Li, Xiao Han, Carter Kittrell, and James M Tour. Laser-induced graphene formation on wood. *Advanced Materials*, 29(37):1702211, 2017.

[69] Yieu Chyan, Ruquan Ye, Yilun Li, Swatantra Pratap Singh, Christopher J Arnusch, and James M Tour. Laser-induced graphene by multiple lasing: toward electronics on cloth, paper, and food. *ACS nano*, 12(3):2176–2183, 2018.

[70] Bohdan Kulyk, Beatriz FR Silva, Alexandre F Carvalho, Sara Silvestre, Antonio JS Fernandes, Rodrigo Martins, Elvira Fortunato, and Florinda M Costa. Laser-induced graphene from paper for mechanical sensing. *ACS Applied Materials & Interfaces*, 13(8):10210–10221, 2021.

[71] Luong Xuan Duy, Zhiwei Peng, Yilun Li, Jibo Zhang, Yongsung Ji, and James M Tour. Laser-induced graphene fibers. *Carbon*, 126:472–479, 2018.

[72] Lixiong Huang, Han Wang, Peixuan Wu, Weimin Huang, Wei Gao, Feiyu Fang, Nian Cai, Rouxi Chen, and Ziming Zhu. Wearable flexible strain sensor based on three-dimensional wavy laser-induced graphene and silicone rubber. *Sensors*, 20(15):4266, 2020.

[73] Lu-Qi Tao, He Tian, Ying Liu, Zhen-Yi Ju, Yu Pang, Yuan-Quan Chen, Dan-Yang Wang, Xiang-Guang Tian, Jun-Chao Yan, Ning-Qin Deng, et al. An intelligent artificial throat with sound-sensing ability based on laser induced graphene. *Nature communications*, 8(1):1–8, 2017.

[74] Michael G Stanford, Cheng Zhang, Jason D Fowlkes, Anna Hoffman, Ilia N Ivanov, Philip D Rack, and James M Tour. High-resolution laser-induced graphene. flexible electronics beyond the visible limit. *ACS applied materials & interfaces*, 12(9):10902–10907, 2020.

[75] Alexandre F Carvalho, António JS Fernandes, Cátia Leitão, Jonas Deuermeier, Ana C Marques, Rodrigo Martins, Elvira Fortunato, and Florinda M Costa. Laser-induced graphene strain sensors produced by ultraviolet irradiation of polyimide. *Advanced Functional Materials*, 28(52):1805271, 2018.

[76] Nuno F Santos, Sónia O Pereira, Ana Moreira, Ana V Girão, Alexandre F Carvalho, António JS Fernandes, and Florinda M Costa. Ir and uv laser-induced graphene: Application as dopamine electrochemical sensors. *Advanced Materials Technologies*, 6(6):2100007, 2021.

[77] Liyong Wang, Zhiwen Wang, Ali Naderi Bakhtiyari, and Hongyu Zheng. A comparative study of laser-induced graphene by co2 infrared laser and 355 nm ultraviolet (uv) laser. *Micromachines*, 11(12):1094, 2020.

[78] Libei Huang, Jianjun Su, Yun Song, and Ruquan Ye. Laser-induced graphene: En route to smart sensing. *Nano-micro letters*, 12(1):1–17, 2020.

[79] Tao Han, Anindya Nag, Roy BVB Simorangkir, Nasrin Afsarimanesh, Hangrui Liu, Subhas Chandra Mukhopadhyay, Yongzhao Xu, Maxim Zhadobov, and Ronan Sauleau. Multifunctional flexible sensor based on laser-induced graphene. *Sensors*, 19(16):3477, 2019.

[80] Manan Dosi, Irene Lau, Yichen Zhuang, David SA Simakov, Michael W Fowler, and Michael A Pope. Ultrasensitive electrochemical methane sensors based on solid polymer electrolyte-infused laser-induced graphene. *ACS applied materials & interfaces*, 11(6):6166–6173, 2019.

[81] Diana C Vanegas, Laksmi Patiño, Connie Mendez, Daniela Alves de Oliveira, Alba M Torres, Carmen L Gomes, and Eric S McLamore. Laser scribed graphene biosensor for detection of biogenic amines in food samples using locally sourced materials. *Biosensors*, 8(2):42, 2018.

[82] Ana C Marques, Ana R Cardoso, Rodrigo Martins, M Goreti F Sales, and Elvira Fortunato. Laser-induced graphene-based platforms for dual biorecognition of molecules. *ACS Applied Nano Materials*, 3(3):2795–2803, 2020.

[83] Cheng Cheng, Shutong Wang, Jayne Wu, Yongchao Yu, Ruozhou Li, Shigetoshi Eda, Jiangang Chen, Guoying Feng, Benjamin Lawrie, and Anming Hu. Bisphenol a sensors on polyimide fabricated by laser direct writing for onsite river water monitoring at attomolar concentration. *ACS applied materials & interfaces*, 8(28):17784–17792, 2016.

[84] Yiran Yang, Yu Song, Xiangjie Bo, Jihong Min, On Shun Pak, Lailai Zhu, Minqiang Wang, Jiaobing Tu, Adam Kogan, Haixia Zhang, et al. A laser-engraved wearable sensor for sensitive detection of uric acid and tyrosine in sweat. *Nature biotechnology*, 38(2):217–224, 2020.

[85] Xue Hui, Xing Xuan, Jiyoung Kim, and Jae Yeong Park. A highly flexible and selective dopamine sensor based on pt-au nanoparticle-modified laser-induced graphene. *Electrochimica Acta*, 328:135066, 2019.

[86] Pranati Nayak, Narendra Kurra, Chuan Xia, and Husam N Alshareef. Highly efficient laser scribed graphene electrodes for on-chip electrochemical sensing applications. *Advanced Electronic Materials*, 2(10):1600185, 2016.

[87] Yue Zhang, Na Li, Yangjun Xiang, Debo Wang, Peng Zhang, Yanyan Wang, Shan Lu, Rongqing Xu, and Jiang Zhao. A flexible non-enzymatic glucose sensor based on copper nanoparticles anchored on laser-induced graphene. *Carbon*, 156:506–513, 2020.

[88] Raquel RA Soares, Robert G Hjort, Cicero C Pola, Kshama Parate, Efraim L Reis, Nilda FF Soares, Eric S McLamore, Jonathan C Claussen, and Carmen L Gomes. Laser-induced graphene

electrochemical immunosensors for rapid and label-free monitoring of salmonella enterica in chicken broth. *ACS sensors*, 5(7):1900–1911, 2020.

[89] Aoife C Power and Aoife Morrin. Electroanalytical sensor technology. *Electrochemistry*, pages 141–178, 2013.

[90] Allen J Bard, Larry R Faulkner, and Henry S White. *Electrochemical methods: fundamentals and applications*. John Wiley & Sons, 2022.

[91] Daniel R Thévenot, Klara Toth, Richard A Durst, and George S Wilson. Electrochemical biosensors: recommended definitions and classification. *Biosensors and bioelectronics*, 16(1-2):121–131, 2001.

[92] Alejandro C Olivieri, Nicolaas M Faber, Joan Ferré, Ricard Boqué, John H Kalivas, and Howard Mark. Uncertainty estimation and figures of merit for multivariate calibration (iupac technical report). *Pure and Applied Chemistry*, 78(3):633–661, 2006.

[93] Nelson R Stradiotto, Hideko Yamanaka, and Maria Valnice B Zanoni. Electrochemical sensors: A powerful tool in analytical chemistry, 2003.

[94] Dorothee Grieshaber, Robert MacKenzie, Janos Vörös, and Erik Reimhult. Electrochemical biosensors-sensor principles and architectures. *Sensors*, 8(3):1400–1458, 2008.

[95] Cynthia G Zoski. *Handbook of electrochemistry*. Elsevier, 2006.

[96] Noémie Elgrishi, Kelley J Rountree, Brian D McCarthy, Eric S Rountree, Thomas T Eisenhart, and Jillian L Dempsey. A practical beginner's guide to cyclic voltammetry. *Journal of chemical education*, 95(2):197–206, 2018.

[97] Matti Kaisti. Detection principles of biological and chemical fet sensors. *Biosensors and Bioelectronics*, 98:437–448, 2017.

[98] Christopher Sandford, Martin A Edwards, Kevin J Klunder, David P Hickey, Min Li, Koushik Barman, Matthew S Sigman, Henry S White, and Shelley D Minteer. A synthetic chemist's guide to electroanalytical tools for studying reaction mechanisms. *Chemical science*, 10(26):6404–6422, 2019.

[99] Yuyan Shao, Jun Wang, Hong Wu, Jun Liu, Ilhan A Aksay, and Yuehe Lin. Graphene based electrochemical sensors and biosensors: a review. *Electroanalysis: An International Journal Devoted to Fundamental and Practical Aspects of Electroanalysis*, 22(10):1027–1036, 2010.

[100] Sónia O Pereira, Nuno F Santos, Alexandre F Carvalho, António JS Fernandes, and Florinda M Costa. Electrochemical response of glucose oxidase adsorbed on laser-induced graphene. *Nanomaterials*, 11(8):1893, 2021.

[101] Wan Li, Cen Tan, Michael A Lowe, Hector D Abruna, and Daniel C Ralph. Electrochemistry of individual monolayer graphene sheets. *ACS nano*, 5(3):2264–2270, 2011.

[102] Shouvik Banerjee, Jiwook Shim, Jose Rivera, Xiaozhong Jin, David Estrada, Vita Solovyeva, Xueqiu You, James Pak, Eric Pop, Narayana Aluru, et al. Electrochemistry at the edge of a single graphene layer in a nanopore. *ACS nano*, 7(1):834–843, 2013.

[103] Federico Maria Vivaldi, Alexander Dallinger, Andrea Bonini, Noemi Poma, Lorenzo Sembranti, Denise Biagini, Pietro Salvo, Francesco Greco, and Fabio Di Francesco. Three-dimensional (3d) laser-induced graphene: structure, properties, and application to chemical sensing. *ACS Applied Materials & Interfaces*, 13(26):30245–30260, 2021.

[104] Junbo Zhu, Xian Huang, and Weixing Song. Physical and chemical sensors on the basis of laser-induced graphene: Mechanisms, applications, and perspectives. *ACS nano*, 15(12):18708–18741, 2021.

[105] Marta Janczuk-Richter, Monika Piestrzyńska, Dariusz Burnat, Petr Sezemsky, Vitezslav Stranak, Wojtek J Bock, Robert Bogdanowicz, Joanna Niedziółka-Jönsson, and Mateusz Śmietana. Optical investigations of electrochemical processes using a long-period fiber grating functionalized by indium tin oxide. *Sensors and Actuators B: Chemical*, 279:223–229, 2019.

[106] Clara Pérez-Ràfols, Núria Serrano, and José Manuel Díaz-Cruz. A hybrid sensing system combining simultaneous optical and electrochemical measurements: Application to beer discrimination. *Talanta*, 241:123273, 2022.

[107] Ying Si, Jiajie Lao, Xuejun Zhang, Yuke Liu, Shunshuo Cai, Álvaro González-Vila, Kaiwei Li, Yunyun Huang, Yong Yuan, Christophe Caucheteur, et al. Electrochemical plasmonic fiber-optic sensors for ultra-sensitive heavy metal detection. *Journal of Lightwave Technology*, 37(14):3495–3502, 2019.

[108] KD Vernon-Parry. Scanning electron microscopy: an introduction. *III-Vs Review*, 13(4):40–44, 2000.

[109] Weilie Zhou, Robert Apkarian, Zhong Lin Wang, and David Joy. Fundamentals of scanning electron microscopy (sem). In *Scanning microscopy for nanotechnology*, pages 1–40. Springer, 2006.

[110] Andrea C Ferrari, Jannik C Meyer, Vittorio Scardaci, Cinzia Casiraghi, Michele Lazzeri, Francesco Mauri, Stefano Piscanec, Dingde Jiang, Konstantin Sergeevich Novoselov, Siegmar Roth, et al. Raman spectrum of graphene and graphene layers. *Physical review letters*, 97(18):187401, 2006.

[111] Ewen Smith and Geoffrey Dent. *Modern Raman spectroscopy: a practical approach*, chapter 1, pages 3–19. John Wiley & Sons, 2019.

[112] Byoung-Yong Chang and Su-Moon Park. Electrochemical impedance spectroscopy. *Annual Review of Analytical Chemistry*, 3(1):207, 2010.

[113] Hend S Magar, Rabeay YA Hassan, and Ashok Mulchandani. Electrochemical impedance spectroscopy (eis): Principles, construction, and biosensing applications. *Sensors*, 21(19):6578, 2021.

[114] Bohdan Kulyk, Sónia O Pereira, António JS Fernandes, Elvira Fortunato, Florinda M Costa, and Nuno F Santos. Laser-induced graphene from paper for non-enzymatic uric acid electrochemical sensing in urine. *Carbon*, 197:253–263, 2022.

[115] Andrea C Ferrari. Raman spectroscopy of graphene and graphite: Disorder, electron–phonon coupling, doping and nonadiabatic effects. *Solid state communications*, 143(1-2):47–57, 2007.

[116] Andrea C Ferrari and Denis M Basko. Raman spectroscopy as a versatile tool for studying the properties of graphene. *Nature nanotechnology*, 8(4):235–246, 2013.

[117] CNR Rao, Kanishka Biswas, KS Subrahmanyam, and A Govindaraj. Graphene, the new nanocarbon. *Journal of Materials Chemistry*, 19(17):2457–2469, 2009.

[118] F Tuinstra and Jack L Koenig. Raman spectrum of graphite. *The Journal of chemical physics*, 53(3):1126–1130, 1970.

[119] Stephan Vogt, Qiang Su, Cristina Gutierrez-Sanchez, and Gilbert Noll. Critical view on electrochemical impedance spectroscopy using the ferri/ferrocyanide redox couple at gold electrodes. *Analytical chemistry*, 88(8):4383–4390, 2016.

[120] Gamry Instruments. Use of Transmission Lines for Electrochemical Impedance Spectroscopy. https://www.gamry.com/application-notes/EIS/use-of-transmission-lines-for-eis/. Accessed in October, 2022.

[121] Gaurav Kumar Mishra and Rama Kant. Modular theory for dc-biased electrochemical impedance response of supercapacitor. *Journal of Power Sources*, 473:228467, 2020.

[122] Ying Wang, Eduardo Laborda, and Richard G Compton. Electrochemical oxidation of nitrite: Kinetic, mechanistic and analytical study by square wave voltammetry. *Journal of Electroanalytical Chemistry*, 670:56–61, 2012.